Microscale Phase Transformation in Shape Memory Alloy Actuators

by

Yue Gong

A dissertation submitted in partial fulfillment
of the requirements for the degree of
Doctor of Philosophy
(Mechanical Engineering)
in The University of Michigan
2017

Doctoral Committee:

Associate Professor Samantha Hayes Daly, Co-Chair
Professor Katsuo Kurabayashi, Co-Chair
Professor Diann Erbschloe Brei
Dr. Nilesh Mankame
Professor John Andrew Shaw

Yue Gong
gongyue@umich.edu
ORCID iD: 0000-0002-8418-6660

To grandmothers:

Mrs. Zhuzhen Wang and
Mrs. Xiuqiao Wu

Acknowledgements

I'd like to thank my adviser Professor Samantha H. Daly. Thank you for giving me the invaluable opportunity to work on this project. Thank you for the time, energy, and patience you invested in me; what I have learned from you and this experience will be instrumental moving forward, both professionally and in life. I'd also like to thank my graduate chair, co-chair, and committee member Professor Katsuo Kurabayashi, for your tireless support and care. Thank you to my committee members Professor John Shaw, Professor Diann Brei, and Dr. Nilesh Mankame for your support and guidance in the GM/UM CRL. I have been very fortunate to be funded by the program and to be part of this supportive, dynamic, collaborative and innovative team. Thanks to all my dearest colleagues: Kaitlyn Mallett, Dr. Keqin Cao, Dr. Ben Reedlunn, Dr, Kyubum Kim, Dr. Adam Kammers, Dr. Jared Tracy, Dr. Michael Kimiecik, Dr. Jason Geathers, Dr. Zhe Chen, Daniel Biggs, Clover Thebolt, Tizoc Cruz-Gonzalez, Chenyang Li, Alan Githens, Marissa Linne, Will LePage, Maya Nath, Corey Bowin, Laura Giñer, Michelle Harr, and Koray Benli. Thanks to the undergraduate students Monica Piñon and Michael Compagner who I had the privilege to work with.

Thanks to my friends around Ann Arbor and from H_2O campus ministry for your love and prayers: Furaha Kariburyo Yay, Melissa Hernandez Duran, Kaitlyn Thunderstorms, Dr. Shinuo Weng, Yuqing Kong, Biqiao Zhang, Lu Tian, Zach Barnes, Cindy and Jonathan Fellows, Jason Kohler, Julie and Chris Payne, and Tammy and Nino Guarisco. Thanks to my mentors, Glenn Galler, Gary Mull, and Winnie Song. Thanks to my parents Dr. Lingling Wang and Dr. Min Gong. You are such cool parents with so much unconventional wisdom. I am grateful for your unconditional support and for caring more about whether I get enough sleep than anything else. I look forward to the mornings because that is the time we can see each other over video calls. I am incredibly blessed to have all of my friends and family.

Table of Contents

List of Tables

List of Figures

Abstract

Shape memory alloys (SMAs) are a class of metallic alloys with the ability to recover large mechanical deformations with little residual strain, and the ability to revert to a previously defined shape or size when deformed and then heated past a set transformation temperature. The prior ability is termed superelasticity (SE) or pseudoelasticity, and the latter is termed the shape memory effect (SME). The most widely used shape memory alloy is Nickel-Titanium, also known as Nitinol, which is a nearly equiatomic mixture of nickel and titanium that undergoes a phase transformation between a B2 cubic austenite and a B19' martensite in order to give rise to these unique properties.

Although Nitinol is utilized in a variety of actuation applications, there is much that is unknown about the microscale characteristics of the transformation that underlies the shape memory effect, particularly under cyclic actuation. At the macroscopic length scale, global measures like stress-strain relationships are used to improve prediction capabilities. These studies provide valuable information, but are averaged measures that cannot capture the transformation heterogeneity inherent to these materials, nor the dependence of this heterogeneity on the underlying microstructure. As such, an opportunity to control material performance through targeted processing of the microstructure is lost.

In this thesis, the transformation characteristics of fine-grained and coarse-grained shape memory NiTi microwires (grain diameters of 20-40nm and 10 μm, respectively) are investigated using a custom experimental methodology combining deformation tracking with scanning electron microscopy in order to map the microscale strains associated with phase transformation

during shape memory actuation. Regardless of the grain diameter, a strongly heterogeneous strain distribution arose with martensite detwinning upon application of load, and remained consistent with actuation cycling. Sub-grain regions that accommodated high amounts of strain in the detwinned state early in the cycling process were more likely to accommodate high amounts of strain in subsequent cycles, and showed a faster accumulation of residual strain in subsequent cycles as well, indicating a link between sub-grain residual strain and strain at detwinned state that is established early and can negatively impact actuator performance. Additionally, correlation coefficients between individual data points tended to increase with thermo-mechanical cycling, indicating that there is a settling in process where the similarity induced by detwinning and plasticity becomes stronger as cycling progresses. In the coarse-grained specimens, neither grain diameter nor grain orientation affected the transformation characteristics of the grain, supporting the hypothesis that it is rather the interactions with the surrounding microstructure that determine transformation characteristics at a point. The standard deviation of the strain increased with the average grain diameter - this strain heterogeneity was inversely related to the ratio between the length scale of the microstructure and the field of view, but was not related to the actuation stroke.

Chapter 1. Introduction and Background

Section 1.1. A Brief History of Nickel-Titanium (NiTi)

Shape memory alloys (SMAs) are a class of metallic alloys with the ability to recover large mechanical deformations with little residual strain [1], and the ability to revert to a previously defined shape or size when deformed and then heated past a set transformation temperature. The prior ability is termed *superelasticity (SE)* or *pseudoelasticity*, and the latter ability is termed the s*hape memory effect (SME)*. Ölander et al. discovered the first SMA, an Au-Cd alloy, in 1932 [2]. The mechanical response of this alloy was reportedly similar to rubber, leading to its description as superelastic. The *shape memory effect (SME)* of shape memory alloys was first comprehensively reported in the late 1940s by [3], [4]. SMAs gained in popularity after the discovery of nickel-titanium (NiTi) alloys. Buehler and Wang first observed SE in a nearly equal-atomic alloy of nickel and titanium in 1962 [5]. The discovery was made in the Naval Ordnance Laboratory, and therefore these NiTi alloys were named Nitinol (Nickel Titanium-Naval Ordnance Laboratory). Buehler et al. discovered the SMA properties of NiTi while working on completing the phase diagram of NiTi binary alloy [5], [9]. The phase diagram of Nitinol was modified through the 1970s, with an update occurring in 1979 that removed the eutectoid decomposition line at 630°C and added an order-disorder transition from B2 to BCC at 1090°C [8]. The discovery of a number of other SMAs followed between 1970 and 2000; a timeline of SMA discovery is shown in Figure 1.1 [6], [7].

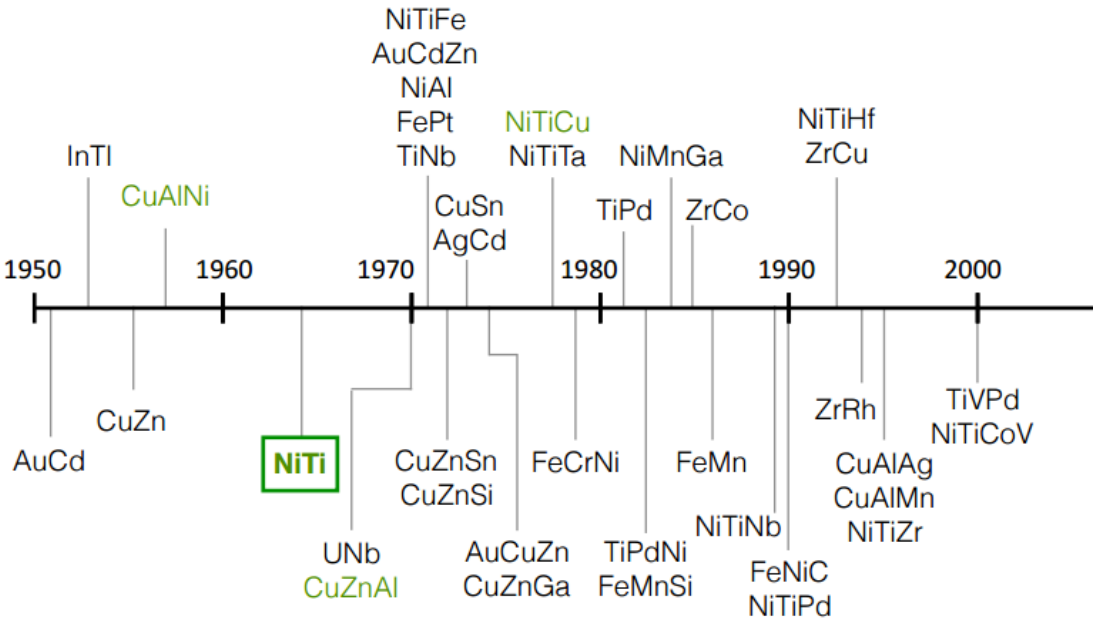

Figure 1.1. A brief summary of the timeline of shape memory alloy discoveries. Those highlighted in green are commercially available. NiTi, the subject of this work, is highlighted in green and boxed. [6], [87]

Schematics of the unit cells associated with the three phases of Nitinol– austenite, martensite, and the R-phase are shown in Figure 1.2 [8]–[10]. In Nitinol, the austenite (A) phase is a B2 cubic crystal. It is highly symmetric, possesses the highest internal energy, and is stable at the highest temperature [11]. The martensite (M) phase is monoclinic, has a lattice that is less symmetric than that of the austenite, and possesses the least internal energy. There are multiple configurations of the martensite lattice, which are called martensite *variants*. For example, a cubic to a tetragonal transformation results in three symmetry-related martensitic variants, whereas the cubic to monoclinic transformation of Nitinol results in twelve martensitic variants. Martensite is stable at the lowest temperature among the three phases [12]–[14]. Although twinned martensite and detwinned martensite have the same lattice parameters, the

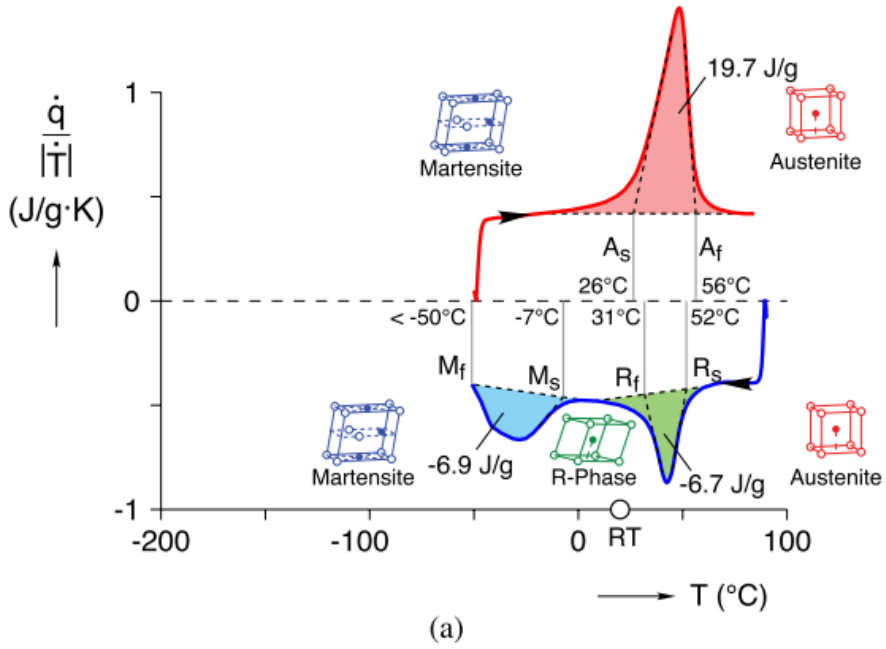

(a)

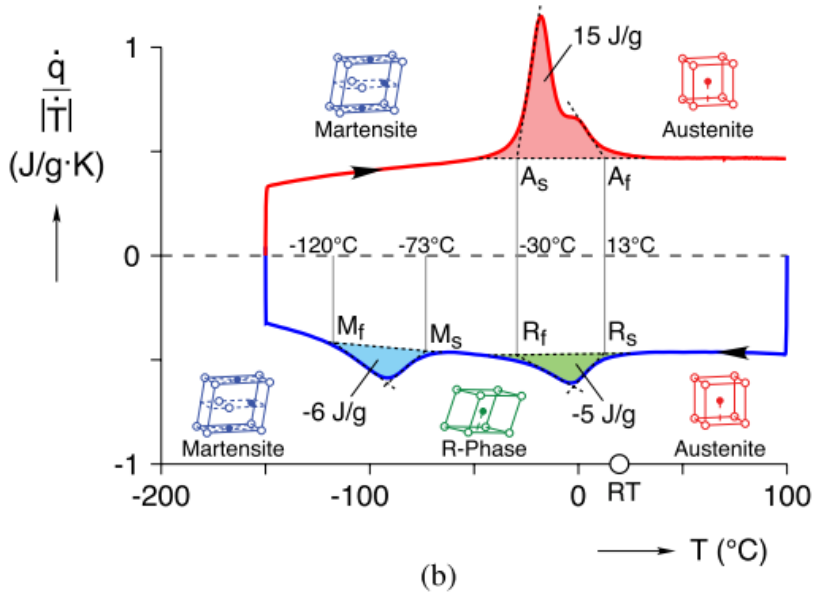

(b)

Figure 1.2. DSC data showing phase transformation in a Nitinol test specimen at a scanning rate of 5˚C/min, with schematics of the unit cells associated with the austenite, martensite, and rhombohedral phases of NiTi. Note that the rhombohedral, or R-phase, is not always present. [8]

lattice structures are arranged in different manners. The term twinned refers to the condition where two regions containing different variants of the martensitic lattice are related to each other by a simple shear and a rotation. The twinning equation that relates these martensite variants is described in Section 1.2. There is also sometimes present an intermediate phase of a rhombohedrally distorted martensite termed the R-phase [15]–[18]. The transformation strain of an austenite to R-phase transition is much smaller, on the order of 0.5%, in comparison to the ~6% transformation strain typically seen in superelastic Nitinol.

Section 1.2. Microstructure of Martensite

There are twelve possible symmetries of monoclinic martensite that can result from transformation of the NiTi B2 cubic austenite. These martensitic configurations, arising through point group symmetry, are called martensitic variants. The crystallographic deformation of the B2 austenite to one of its 12 variants is described using a transformation matrix U. The twelve transformation matrices for Nitinol are given below [19]:

$$U_1 = \begin{pmatrix} \gamma & \epsilon & \epsilon \\ \epsilon & \alpha & \delta \\ \epsilon & \delta & \alpha \end{pmatrix}, \qquad U_2 = \begin{pmatrix} \gamma & -\epsilon & -\epsilon \\ -\epsilon & \alpha & \delta \\ -\epsilon & \delta & \alpha \end{pmatrix},$$

$$U_3 = \begin{pmatrix} \gamma & -\epsilon & -\epsilon \\ -\epsilon & \alpha & -\delta \\ \epsilon & -\delta & \alpha \end{pmatrix}, U_4 = \begin{pmatrix} \gamma & \epsilon & -\epsilon \\ \epsilon & \alpha & -\delta \\ -\epsilon & -\delta & \alpha \end{pmatrix},$$

$$U_5 = \begin{pmatrix} \alpha & \epsilon & \delta \\ \epsilon & \gamma & \epsilon \\ \delta & \epsilon & \alpha \end{pmatrix}, \qquad U_6 = \begin{pmatrix} \alpha & -\epsilon & \delta \\ -\epsilon & \gamma & -\epsilon \\ \delta & -\epsilon & \alpha \end{pmatrix},$$

$$U_7 = \begin{pmatrix} \alpha & -\epsilon & -\delta \\ -\epsilon & \gamma & \epsilon \\ -\delta & \epsilon & \alpha \end{pmatrix}, U_8 = \begin{pmatrix} \alpha & \epsilon & -\delta \\ \epsilon & \gamma & -\epsilon \\ -\delta & -\epsilon & \alpha \end{pmatrix},$$

$$U_9 = \begin{pmatrix} \alpha & \delta & \epsilon \\ \delta & \alpha & \epsilon \\ \epsilon & \epsilon & \gamma \end{pmatrix}, \qquad U_{10} = \begin{pmatrix} \alpha & \delta & -\epsilon \\ \delta & \alpha & -\epsilon \\ -\epsilon & -\epsilon & \gamma \end{pmatrix},$$

$$U_{11} = \begin{pmatrix} \alpha & -\delta & \epsilon \\ -\delta & \alpha & -\epsilon \\ \epsilon & -\epsilon & \gamma \end{pmatrix}, U_{12} = \begin{pmatrix} \alpha & -\delta & -\epsilon \\ -\delta & \alpha & \epsilon \\ -\epsilon & \epsilon & \gamma \end{pmatrix}$$

Transformation matrices of the cubic to monoclinic I transformation in Nitinol, where

$$\alpha = 1.0243, \gamma = 0.9563, \delta = 0.058, \epsilon = -0.0427$$ [20], [21]

The ultra-fine microstructure of martensitic NiTi has been modeled through various means, for example using an energy density with two rotationally invariant energy wells [22]–[24]. Ball and James [22] first worked out this idea for internally twinned martensite (fine bands of martensite on one side of an interface, and a homogeneous austenite phase on the other side), and found that the minimizing sequences associated with this microstructure did deliver an austenite/martensite interface with an orientation and arrangement that agreed with experimental results. Unlike crystallographic theory, this minimum energy approach required no *a priori* geometric restrictions on phase domains and was able to predict microstructure resulting from general mixed boundary conditions. In 1992, Ball and James extended this work to additional

results that were amenable to quantitative experimental testing, by considering the two-well problem [23]; i.e. in determining possible microstructures that can arise from energy-minimizing sequences in the simplest case that leads to microstructure. This resulted in a limited fineness of the observed microstructures which was not predicted by the minimizing sequences; possible explanations included a small surface energy per unit area on twin boundaries that contributed significantly to the total energy of a fine microstructure, which has interesting implications in terms of ratios between twin boundary energy and bulk energy for various materials. An additional mechanism for limited fineness, as suggested by Ball et al. in 1991, is the inability of the chosen dynamic solution for interface refinement to reach an absolute minimizing sequence, rather getting 'stuck' at a relatively weak minimizer with finite interfaces [25]. They proposed experimental tests of their theoretical predictions by examining the mechanical response of properly oriented plates subject to simple shear.

The possible twinning modes in the martensite are determined as a consequence of the energy well structure. Result 1 describes the compatibility required for two martensite variants to form a twin, for the variant pair *I* and *J*. The variables are as follows: the twin rotation Q, the twin shear $\boldsymbol{a}$, and the vector normal to the plane ($\hat{\boldsymbol{n}}$) that constitutes the interface between the two regions. If the two martensite variants are compatible with each other, the magnitude and direction of $\boldsymbol{a}$ should be shared by both variants. There are at most two solutions for this equation. If the twinning plane is rational and the shearing direction has irrational indices, the twin is categorized as a type I twin. However, if the twinning plane is irrational and the shearing direction has rational indices, it is categorized as a type II twin. When the twinning plane and the shearing direction both have rational indices, it is referred to as a compound twin [19], [22], [26], [27].

Result 1. Given positive definite U_I and U_J, there exists a rotational matrix Q, $a \neq 0$ and $\hat{n}$ such that,

$$QU_I - U_J = a \otimes \hat{n}$$

The equation only has a solution if and only if the eigenvalues satisfy $\lambda_1 \leq 1$, $\lambda_2 = 1$, $\lambda_3 \geq 1$.[21]

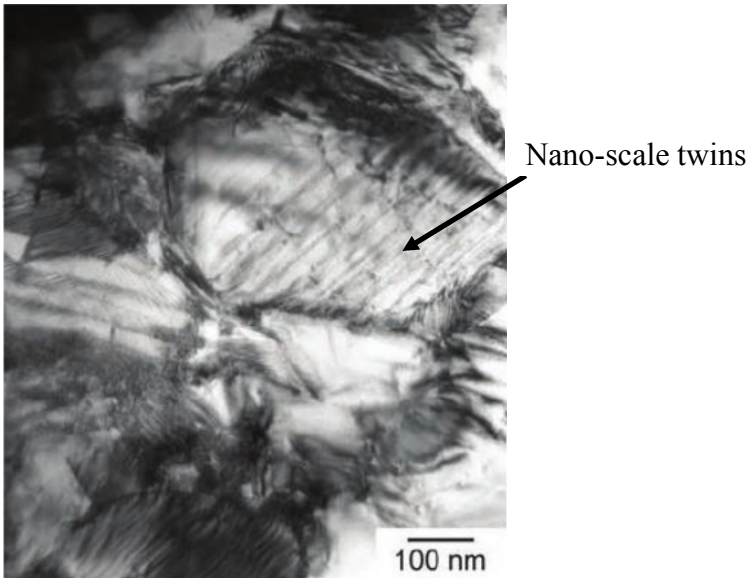

Figure 1.3: TEM micrograph of nano-scale twins in a heat treated shape memory NiTi wire. [88]

Twinned martensite coexists with the austenite phase in a structure wherein a homogeneous region of austenite is separated from a region of twinned martensite variants by a transition layer. In addition to compatibility between the individual martensitic variants, the variant combination needs to ensure minimum free energy at the load-free state below martensite finish temperature [28]. To explain how the austenite and twinned martensite co-exist, the concept of habit plane variants (HPVs) was introduced by Miyazaki et al. [26]–[28], where the

habit plane variant consists of twinned martensite lattice correspondence variants. There are theoretically 192 possible HPVs between the 12 symmetry-related martensite variants of Nitinol. Experimentally, however, Type II twins have been observed to dominate and are therefore used in modeling efforts [13], [27], [29]–[34]. Brinson et al. used interference filtered optical imaging to investigate the activation of martensite variants during superelastic cycles of NiTi. As shown in Figure 1.4, the same variants were observed to activate during 10 cycles [35].

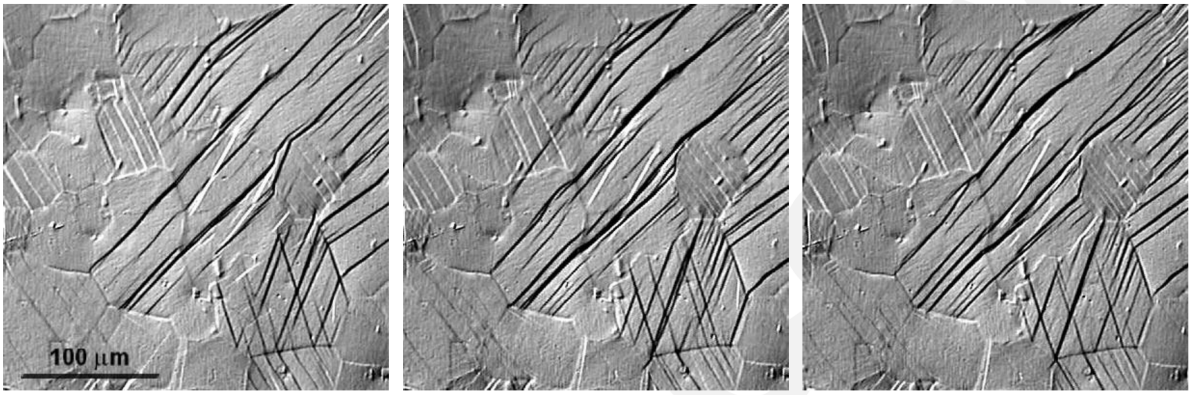

Figure 1.4: Micrographs of activated variants at 2% strain in one set of grains at different cycle numbers during superelastic cycling (cycle 1, 6 and 10 from left to right). Although the same habit plane variants are activated each loading cycle, the spatial position of the variants within the grains varies from cycle to cycle. [35]

Section 1.3. Stress-Strain-Temperature Response of NiTi

Superelasticity and the shape memory effect are facilitated by stress- and temperature-induced phase transformations, respectively. These effects involve solid-to-solid phase transformations with complex interactions between phases at the microstructural length scale. The microscale characteristics of the transformation path that underlies the shape memory effect will be explored in this dissertation work.

Section 1.3.1. Transformation Temperatures and Nomenclature

Transformation temperature refers to the temperature at which phase transformation takes place at macroscopically stress-free state. There are six transformation temperatures in NiTi. Figure 1.2 shows differential scanning calorimetry [8]–[10] data of NiTi showcasing all three phases during thermal cycling. The x-axis of the graph is the testing temperature. The y-axis shows the heat flux from the testing machine to the sample. Positive heat flow indicates heat absorption into the sample, and negative heat flow indicates heat release from the sample. Since phase transformation in Nitinol requires heat input/output, NiTi samples will absorb or release energy from the environment in the form of heat during transformation between phases. Using this characteristic, it is possible to observe phase transformation in the form of heat flow peaks and valleys.

On the heating path on the upper half of the curve, there is a single endothermic peak during the transformation from the martensite to austenite phase of NiTi. The sample absorbed heat in order to complete the phase transformation. On the cooling path, there are two exothermic peaks. The first peak corresponds to the transformation from the austenite phase to the R phase, and the second peak is from R phase to the martensite phase. These phase

transformations are proceeding from a higher energy phase to a lower energy phase; therefore the sample released heat to the environment.

There are no clearly defined points in the curves in Figure 1.2 to represent the exact transformation temperatures. This is due to the heterogeneous nature of transformation through the specimen. To pick out the transformation temperatures at which phase transformations take place, the intersection of the tangential lines is taken before, after the turn of heat flow rate are taken to represent the transformation temperatures. On the heating path, the sample begins to transform into the austenite phase at the austenite start temperature A_s. The transformation is considered complete at the austenite finish temperature A_f. On the cooling path, the sample first reaches the temperature R_s where austenite to R-phase transformation takes place. As cooling continues, the specimen reaches the R-phase finish temperature R_f, the martensite start temperature M_s, and finally the martensite finish temperature M_f. Note that R_s and R_f are not always present during cooling.

Section 1.3.2. Superelasticity (SE)

The superelastic effect is driven by a stress-induced, solid-to-solid, diffusionless phase transformation between austenite and martensite at temperatures above A_f (Figure1.5). Large strains on the order of 6% are possible, with minimal accumulation of residual strain.

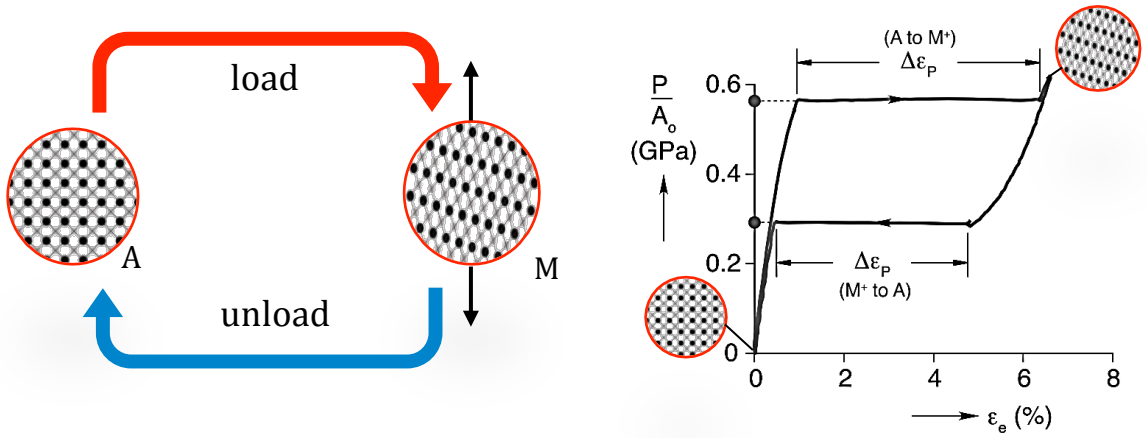

Figure 1.5: Stress-induced transformation between austenite and detwinned martensite that underlies the superelastic effect in Nitinol. (right: [8])

In Figure1.5, the initial state of the material at zero load and temperature > A_f is austenite.[1] Upon the application of load, the austenite elastically deforms up to a strain of roughly 1% (note this strain range is very temperature dependent). Although this deformation is macroscopically elastic, it has been shown that pockets of stress-induced martensite are present in a small amount, driven by crystal orientation and a heterogeneous strain distribution. With further loading, the applied stress reaches (or briefly exceeds) the stress needed to initiate the austenite to martensite phase transformation. During the stress plateau indicating macroscopic transformation from austenite to stress-induced martensite, localized bands of high strain, globally considered to be martensite, propagate through the specimen. During this plateau, the material transforms from the austenite phase to the detwinned martensite phase, in which

[1] Throughout this thesis, stages of transformation will be referred to by their main component; for example, austenite phase will be referred to as 'austenite'; but microscale transformation is significantly more complex and heterogeneous than this nomenclature would indicate, where the austenite includes pockets of transformed martensite, and vice versa.

[2] Note that this is different from the sigma value at a data point given by the Vic2D software, termed sigma[pixel], which provides feedback on the data quality as the 1-standard deviation confidence in the match at this point, in pixels [7]. For sigma[pixel], a value of zero indicates a perfect match, whereas higher numbers indicate noise

detwinned martensite appears in the form of Lüders-like bands that initiate and then propagate through the specimen.

In Figure 1.5, the reverse transformation from detwinned martensite to austenite takes place upon unloading. Elastic strain in the martensite is recovered, followed by a constant stress plateau (at a lower globally applied stress than the loading plateau), now indicating a reverse transformation from martensite to austenite. At the beginning of the reverse stress plateau, there is also a slight stress increase that represents austenitic nucleation, similar to the stress peak upon loading indicative of martensitic nucleation. When the reverse transformation from martensite to austenite is macroscopically complete, the stress will decrease following the austenitic elastic modulus. If, upon loading, the specimen is not unloaded after transformation but rather loaded significantly beyond the end of the stress plateau, the martensite will undergo significant plastic deformation proceeding to eventual fracture. The plastic strain resulting from slip and dislocation activity is not recovered upon unloading.

Experiments have shown that the stress-induced transformation between austenite and martensite in superelastic NiTi is not thoroughly completed. Although NiTi is referred to as austenite above A_f, retained martensite pockets still exist within the austenite [36]. These retained martensite pockets are impacted by intergranular constraints imparting heterogeneous stress fields in the microstructure during the globally applied uniaxial tension loading. Likewise, there can be retained austenite pockets in the martensite upon what is considered macroscopically complete reverse transformation. At the microscopic level, Kimiecik et al [37], [38] observed pockets of retained austenite throughout all loading stages, even when the material was globally considered fully martensite and was undergoing plastic deformation.

Figure 1.6: Examples of NiTi applications utilizing superelasticity: 1. endoscopy tools, 2. spinal implants, 3. vena cava filters, 4. NiTi clips, 5. glass frames, 6. arterial stents, 7. surgical files, 8. orthodontics arch wires. [39], [40], [89]

The superelastic property of NiTi offers significant opportunity, particularly in biomedical applications [39], [40]. The advent of NiTi devices, including septal defect occlusion devices and stents, has enabled the placement of medical devices into patients in a significantly less obtrusive manner than was previously possible. The superelastic property of NiTi allows, for example, a Nitinol septal defect occlusion device to be compacted onto a catheter, and directed up to the heart through an artery where it is in then installed before the catheter is then removed again through the artery. This route of medical device installation inside the body, enabled by the superelastic properties of the Nitinol alloy and thus its ability to reform inside the body after being compacted for insertion, has led to reduced hospital stays and better patient mortality outcomes. Additionally, the constant stress plateau that results from the austenite to martensite phase transformation also enables NiTi devices to traverse a large strain range while maintaining a constant stress output, which facilitates its use in devices ranging from stents to dental braces. Examples of biomedical applications of SE Nitinol are shown in Figure 1.6, including but not limited to orthodontic guide wires, endoscopic guide wires, cardiovascular stents, and

orthopedic support implants. The superelastic properties of NiTi have also been employed in other applications, including cell phone antennae and eyeglass frames.

Section 1.3.3. Shape Memory Effect

The shape memory effect (SME) in Nitinol is driven by a diffusionless, stress-induced phase transformation between the B2 cubic austenite and B19' monoclinic martensite phases. The steps are illustrated in Figure 1.7: Point 1 is at a temperature < M_f, at which the specimen is primarily comprised of twinned martensite. When deformation is then applied to the specimen, the martensite detwins, which manifests as a global stress plateau indicated by point 2. If the specimen is unloaded at point 3, the unloaded specimen (at point 4) will exhibit residual deformation that can consist of locked-in phase transformation and plastic deformation. Post-unload, if the material is heated beyond A_s, it will begin reverting to the austenite phase (denoted by point 5), and fully recover its undeformed shape in the ideal case. Subsequently, when the material is cooled below M_f, the austenite will self-accommodate to the twinned martensite (point 6).

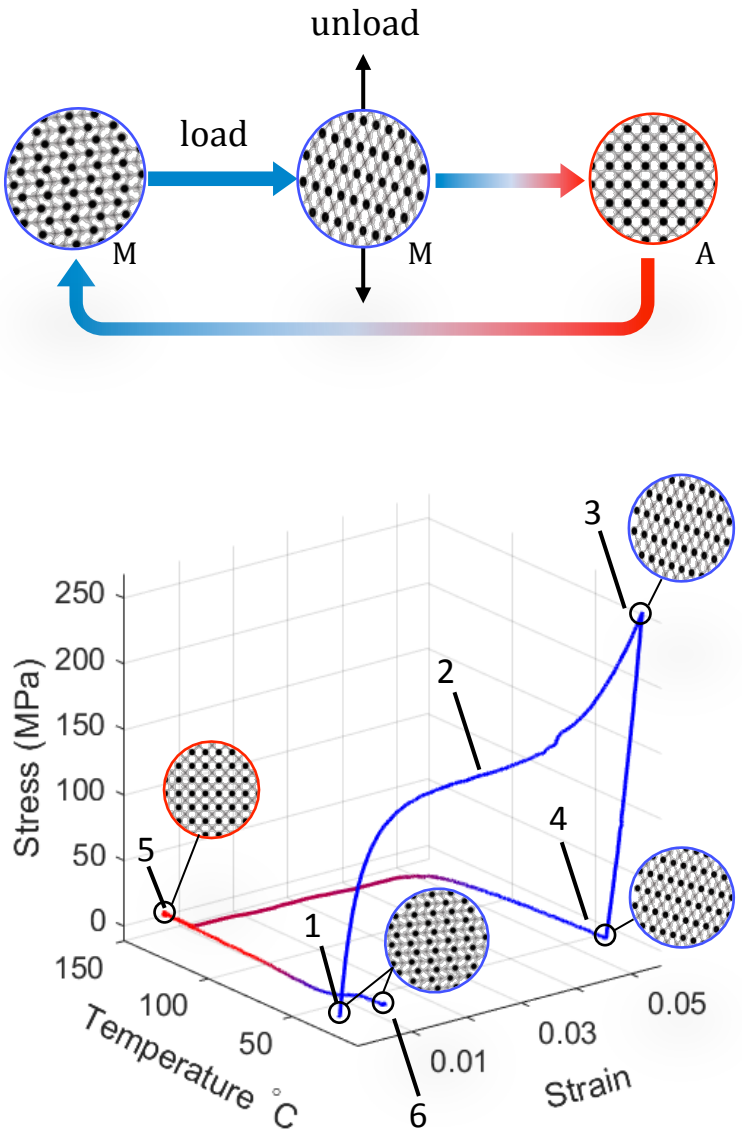

Figure 1.7: Transformation path underlying the shape memory effect in NiTi.

The residual strain that accumulates with shape memory actuation is a combination of plasticity and retained martensite. Theoretically, the strains at detwinned state can be fully recovered, if not loaded too far, through the temperature-induced phase transformation from detwinned martensite to the B2 cubic parent austenite. This austenite phase configuration will self-accommodate to twinned NiTi upon cooling with theoretically zero strain. However, there are factors that inhibit full deformation recovery. Residual strain can arise from unavoidable incompatibilities between phases at the microstructural length scale, which will be detailed in Section 1.3.3. The phase transformation between austenite and martensite has been found to be heterogeneous and incomplete in experimental studies on both superelastic and shape memory NiTi [41], where the residual deformations at temperatures $T>A_f$ during shape recovery and $T<M_f$ during cooling can include retained martensite and austenite, respectively, also leading to the accumulation of residual strain. Recently, a new ultralow-fatigue shape memory alloy film system based on TiNiCu has been reported that allows an unprecedented number of cycles (on the order of 10 million), through the use of Ti_2Cu precipitates that serve as 'sentinels' to guide complete and reproducible transformation in each actuation cycle [42]. In 2006, Cui et al. identified a new composition region for titanium-rich SMAs to improve the control of SMA properties, through manipulation of the second eigenvalue (λ_2) of the transformation stretch tensor [43]. A value of $\lambda_2=1$ indicates that the austenite is directly compatible with a single variant of martensite; in absence of this, a fine laminated mixture of variants that is approximately compatible with the austenite is formed, as described above, leading to both elastic and interfacial energy. If $\lambda_2=1$, there is no need for an elastic transition later or a fine structure of twinned martensite, leading to hysteresis reduction. Cui et al. validated their theoretical predictions of minimum hysteresis as λ_2 approaches 1, and checked the universality of

this criterion by synthesizing several alloys in the Ni-Ti-Pd system. In 2013, Song et al. demonstrated the first martensitic material ($Zn_{45}Cu_{30}Au_{25)}$ that closely satisfies recently proposed 'cofactor conditions' to form a laminated twinned microstructure that meets austenite at a low-elastic-energy transition layer, and therefore exhibited ultrahigh reversibility and an unusual microstructure. This alloy achieved a transformation temperature shift of <0.5˚C after 16,000 thermal cycles (versus a shift of nominally 20˚C in the first 20 cycles for NiTi), and to maintain a thermal hysteresis of approximately 2˚C during this cycling (compared with up to 70˚C in NiTi) [44]. Because the fabrication of this material depends only on lattice parameters which can be tuned by compositional changes, this result suggests a universal strategy for developing reliable martensitic materials. These shape memory alloys are particularly exciting, as they represent a breakthrough in the ongoing search to create more durable shape memory alloys.

Shape memory alloys can also exhibit a two-way shape memory effect after certain thermo-mechanical treatments, in which the material exhibits shape memory upon both heating and cooling; i.e., the shape of the martensitic phase can be remembered under certain conditions. This is in contrast to the one-way shape memory effect described above and examined in this thesis, in which the alloy is deformed at a state below A_s and holds the deformed shape until it is heated above its transition temperature, at which point it reverts back to the austenite phase and its original shape; when cooled to twinned martensite, it will then remain in this original (austenite) shape. The two-way shape memory effect is smaller in magnitude and its cyclic behavior is not as well understood, in part because the cyclic use of the one-way effect is considered more economic [45].

Shape memory actuation is advantageous under limited space and weight allowances, as are found in automotive, robotic, and aerospace applications. Shape memory actuation has

gained considerable attention in automotive applications, where, for example, once a NiTi wire actuated, a resettable spring lift can quickly respond to collisions between cars and pedestrians, providing a lifting/damping force to mitigate further injury of the affected pedestrian (Figure 1.8a). NiTi wires have also been used in damping control systems to provide actuation for the infotainment system in vehicles (Figure 1.8b). Additionally, through the use of webbed SMA structures, the door seal of a car can be controlled and actuated to improve the seal by providing a higher seal pressure, as well as providing flexibility for seal pressure adjustment (Figure 1.8c), which improves the user's experience in opening and closing vehicle doors. The shape memory effect is also utilized in aerospace applications, such as its use in altering the morphology of aircraft structures and chevrons. It is also of interest for its significant potential in small-scale applications like MEMs, where actuation can be performed at the microscale with minimal moving parts (Figure 1.9). The above applications require actuation to be reliable and fatigue resistant. To improve the capabilities of existing devices and expand the design space for future applications, particularly with respect to life and predictive modeling capabilities, there is a need to understand the microscale characteristics of actuation cycling.

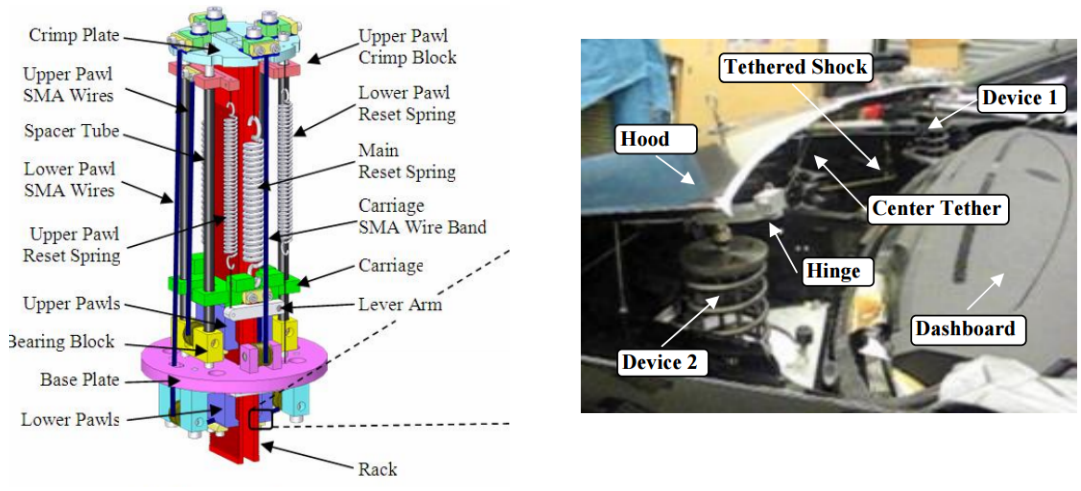

a)

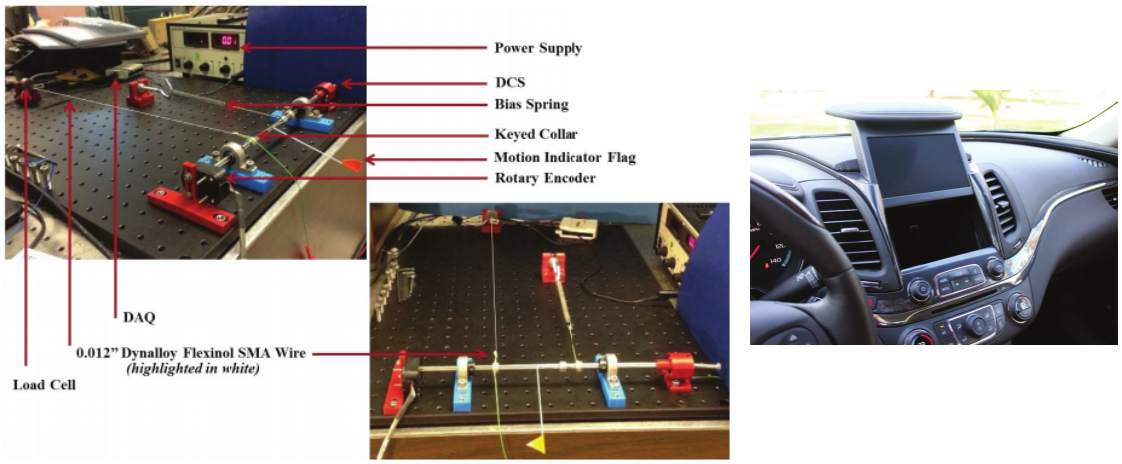

b)

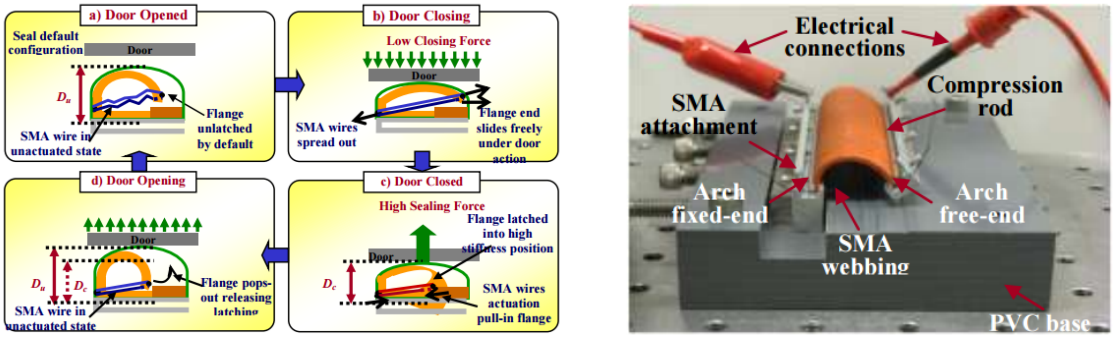

c)

Figure 1.8: Recent SME applications in auto industry. a) shape memory alloy resetable spring lift for pedestrian protection [90]; b) SMA wire providing smooth actuation for infotainment elements in cars [91]; c) a prototype of latched active arch seal for car doors [92].

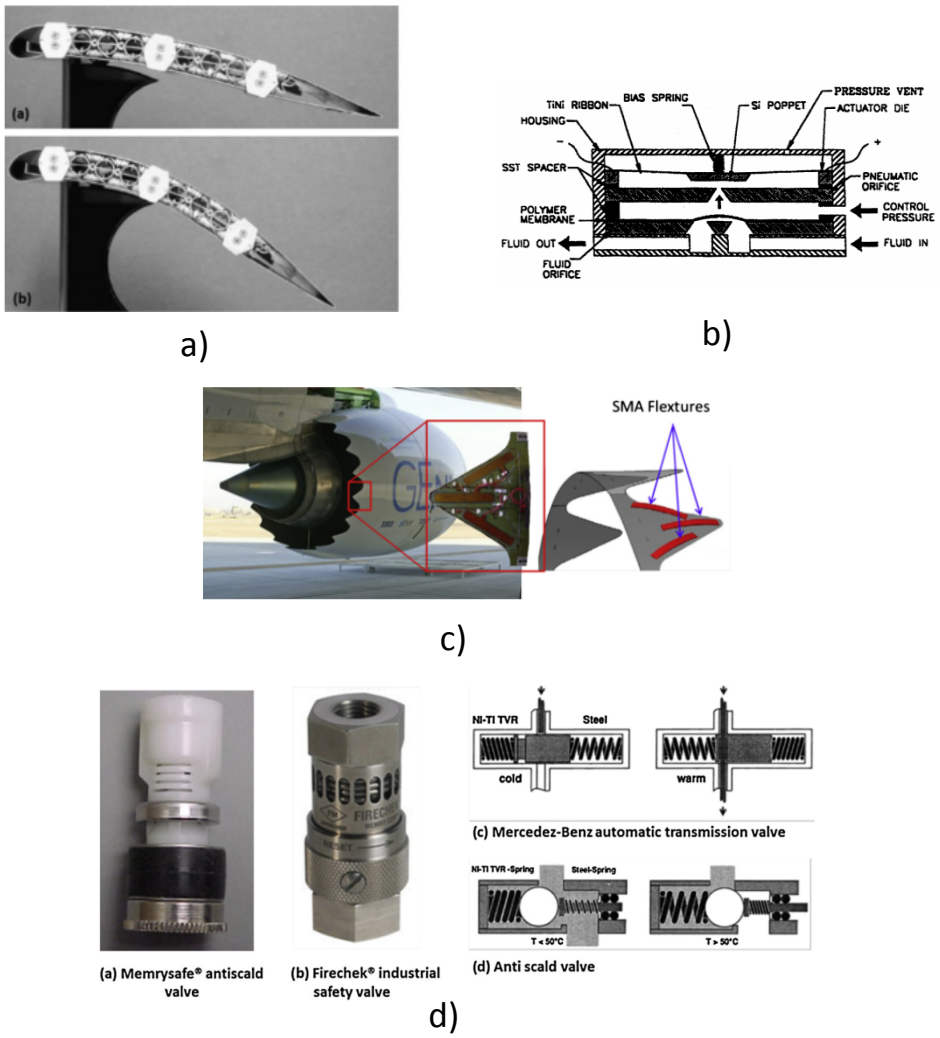

Figure 1.9: SME applications. Aviation and valve coupling. a) aircraft wings; b) MEMs fluid control; c) airplane engine chevrons; d) temperature sensing valves [40]

Although Nitinol is utilized in a variety of industrial actuation applications, there is still much that is unknown about the microscale characteristics of the transformation that underlies the shape memory effect, particularly during cyclic actuation. There are limited studies on phase transformation during the SME of Nitinol, and these have largely focused on either the macroscale or sub-micrometer length scales. However, there has been interesting and related research on the impact of mechanical cycling on superelastic (SE) NiTi. Several factors can influence the behavior of SE Nickel-Titanium under cyclic loading, including its Ni content, the heat treatment of the sample prior to testing, the temperature and strain rate at which the test is conducted, and the initial microstructure, amongst others. Several aspects of the superelastic response of NiTi under mechanical cycling can be related to the development of dislocations and/or retention of martensitic nuclei, and the interplay between plastic slip and the propensity to transform based on crystallographic texture.

Section 1.4. Cyclic Loading of Superelastic Nitinol

Although superelasticity is the not the focus of this work, prior research on SE under cyclic loading motivates research into the microscale transformation characteristics of the shape memory effect under cyclic actuation. There are numerous factors that can influence the transformation of Nitinol under cyclic loads, including Nickel content, material processing, ambient temperature, applied loading parameters, and initial microstructure, amongst others [46]. A primary factor in the performance metrics of transformation relate back to the interplay between phase transformation and slip processes; recent mesoscale modeling by Richards et al. determined that transformation and plasticity can in fact occur synergistically, where plasticity can provide a mechanism to bridge poorly-oriented, and thus non-transforming, grains [47]. Experimentally, Strnadel et al. determined that in SE Nitinol, a higher nickel content resulted in

an increased critical shear stress required for slip, and thus suppressed the development of residual deformation [48]. The characteristics and resulting global performance of NiTi under cyclic loads (such as the amount of hysteresis) can also be significantly affected by cycling, due to small-scale deformation processes including the development of dislocations and/or the retention of martensitic and austenitic nuclei.

Strain memory, indicative of a similarity in the transformation characteristics, has been observed at various length scales in SE Nitinol. A global memory has been observed in macroscopic tests on SE specimens, wherein if the specimen is unloaded partway through the stress plateau, and then reloaded, the resulting sub-loop rejoins the original (full) stress-strain curve at the same state from which it left. This *return point memory* is also occasionally referred to as 'wiping out', since in effect the memory of the presence of this sub-loop is erased as soon as the stress is raised above the original value. For a discussion of return point memory in the context of the dynamics of first-order phase transformations, please see [49]. The presence of a spatially distributed strain memory has also been shown at the mesoscale, in both the extent and distribution of phase transformation, in flat sheet specimens of a commercial superelastic NiTi alloy of 55 wt% Nickel and 45 wt% Titanium [46]. Three-dimensional digital image correlation and infrared imaging were used to examine stress-induced martensitic transformation in Nickel-Titanium during uniaxial, zero-to-tension cyclic loading. Although the stress-induced austenite to martensite transformation becomes more homogeneous with cycling, there was a strong strain pattern memory across the gage section from cycle to cycle, which was much stronger in the stress-induced martensite (inside the localized band) than in the austenite (outside the localized band). This indicates that the manner in which the martensite accommodated strain in the first cycle strongly dictates how the martensite will accommodate strain in future cycles for this alloy.

Further studies on this alloy demonstrated that texture played a large role in both the initial transformation and subsequent response under cyclic loading, wherein flat sheet specimens cut transverse to the rolling direction demonstrated a stronger cycle-to-cycle similarity in the strain accommodated within the deformation band, and the martensite phase consistently showed a stronger strain similarity over austenite regardless of specimen texture [50].

Section 1.5. Effect of Texture

Experimental and analytical studies have shown a strong crystallographic dependence of phase transformation, therefore changing the crystallographic texture of Nitinol can be an effective means of improving its cyclic properties (for example see [46], and the references therein). However, crystallographic effects have been largely ignored in commercial computational tools for both SE and SME, which as Mehta et al. demonstrated, can lead to large deviations between the predicted and actual responses of the material [51]. Part of this is due to a lack of experimental data at the microstructural length scale and limited, but improving, experimental and analytical capabilities to characterizing the complex interactions that occur between phase transformation at local, sub-grain points and their surrounding three-dimensional microstructure. This remains a challenge in the community. More work has been performed to characterize microstructural effects on superelastic Nitinol than on shape memory Nitinol, motivating the study on coarse-grained Nitinol detailed in Chapter 5 of this dissertation.

Practical applications of the shape memory effect require reliability and fatigue resistance during numerous actuation cycles. Therefore, it is crucial to understand the deformation mechanisms inherent in the phase transformations that underlie this actuation, which are strongly dependent on the material microstructure. Deformation and microstructural data has been widely used to examine the relationships between processing and performance, but many of these

studies related averaged metrics. Similar research on the shape memory effect has been scarce despite the interest in the use of SME Nitinol in small scale devices, as it is experimentally difficult to relate local microstructure and spatially resolved deformations.

Macroscopic studies have shown that the microstructures resulting from rolling, extrusion, and drawing significantly impact the transformation characteristics of superelastic NiTi [52]–[54]. It has been postulated that certain microstructures can result in larger recoverable strains due to an increased number of transforming martensite variants [55], in concurrence with experimental findings. In NiTi flat sheet, specimens oriented along the rolling direction exhibit relatively large superelastic transformation strains, whereas those cut perpendicular to the rolling direction (TD) exhibit smaller transformation strains and accumulate smaller residual strains. This is due to the interplay between the critical resolved stresses needed for slip and phase transformation. Mulder et al.[56] found that the angular dependence of the Schmid factor for slip in a TD specimen was close to zero for all four possible martensite textures corresponding with that same system in the austenite. Chang and Wu [57] similarly postulated that smaller residual strains in TD flat plate specimens were due to the small (on average) Schmid factors of the grains.

Recent studies [38], [58], [59] on superelastic NiTi have related the transformation of individual grains to microstructure using diffraction and scanning electron microscopy. It has been shown that the austenite to martensite phase transformation can exhibit substantial transformation memory with cycling, and that transformation depends on local microstructural characteristics rather than individual grain diameter or orientation [50], [59]–[61]. In a recent publication by Paranjape et al., superelastic polycrystalline Nitinol was examined using far-field high energy diffraction microscopy to examine grain-averaged statistics and create a synthetic

microstructure for finite element analysis [62]. The grain-averaged responses of individual austenite crystals were examined during stress-induced transformation, and it was found that grains in the test specimen interior carried more axial stress than the surface grains during specimen 'shake-down' under cyclic loading. The authors concluded that intra-granular heterogeneity is more strongly driven by the constraints of neighboring grains than by the initial stress state or individual grain orientation. In studies on the SME effect in heat-treated Nitinol microwires detailed in Chapter 5, individual grain orientation and size also appear to be minimally significant in driving the intra-granular heterogeneity in the strain accompanying detwinning upon mechanical loading from the originally twinned state.

While superelastic NiTi has been studied at various length scales, work that investigates the effect of microstructure on the shape memory effect in NiTi is scarce, due in part to difficulties in obtaining spatially-resolved microstructural data on martensite. The ultra-fine plates of the monoclinic martensite phase can be on the order of 10nm in width [41], [63], [64], which is smaller than the current resolution of EBSD [65]; as an additional difficulty for EBSD characterization, these martensite variants are symmetry related. As described in Chapter 5, to examine effects of microstructure on the shape memory effect, SME NiTi microwires were heat-treated through a two-step process to obtain an average grain diameter of about 10μm while maintaining shape memory. EBSD scans were then obtained in the austenite phase, while the wire samples were heated to above A_f; it was not possible to obtain EBSD maps in the martensite phase for the reasons stated above, and therefore detwinning activity was examined with respect to the original austenite state. Strain maps were collected for five actuation cycles and analyzed with respect to the microscale transformation characteristics of the as-received wires and the underlying microstructure as characterized in the austenite phase.

Section 1.6. Effects of Composition and Heat Treatment

The mechanical behavior of NiTi strongly depends on alloy composition, where the shape memory properties and transformation temperatures can change significantly with even a fraction of a percent difference in composition. As illustrated in Figure1.10 from [66], the martensitic start temperature, M_S, in NiTi is particularly sensitive to composition. Commercially available superelastic NiTi generally has a nickel content ranging from 50.2% at to 52% at, and shape memory NiTi generally has a nickel content from 49% at to 50.2% at [67].

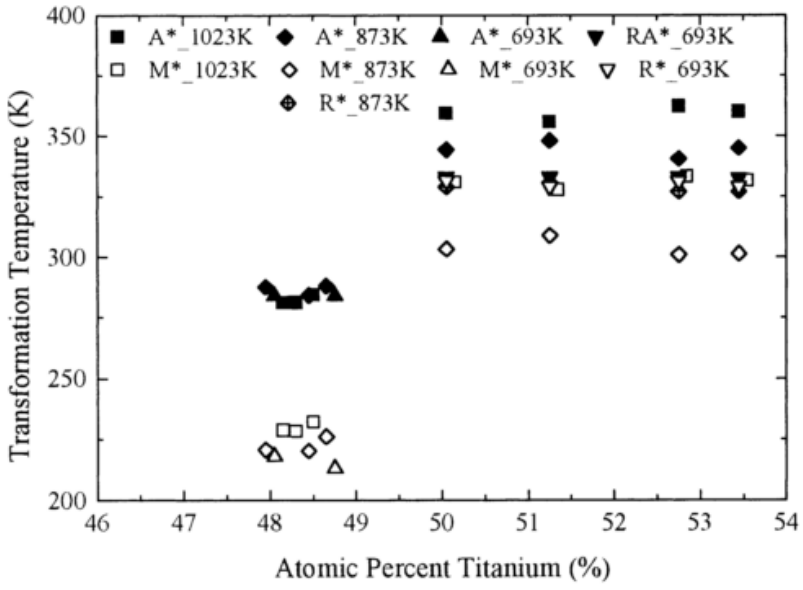

Figure 1.10: Variation of SMA transformation temperatures with composition (annealing at 693, 873 and 1023 K for 15 min) [66]. A_s is the austenite start temperature during heating, M_s and R_s are the martensite start temperature and R-phase start temperature respectively during cooling. (also shown in Figure 1.2.

Transformation temperatures can also be manipulated by aging, where the overall content of the alloy remains constant but local shifts of composition can affect the transformation temperatures. The heat treatment of NiTi can significantly change the composition, shape, size

and distribution of precipitates and therefore affect the transformation characteristics; for example, it was found that decreasing the annealing temperature of Ti-rich films resulted in a decrease of transformation temperature and transformation temperature hysteresis [66]. The heat treatment chosen for a Nitinol alloy will depend on its Nickel composition, as aging Ni-rich alloys will result in the precipitation of Ni-rich compounds [68]. Transformation temperatures will increase with the formation of Ni-rich precipitates (e.g. Ti_3Ni_4), which reduce the overall content of nickel in the matrix of the shape memory alloy. The common forms of NiTi precipitates include Ti_3Ni_4, Ti_2Ni, Ti_2Ni_3 and $TiNi_3$. Most of the precipitates in NiTi exhibit lenticular shapes; it has been shown that the Ni-rich precipitates are coherent or semi-coherent precipitates in B2 NiTi, and the Ti-rich precipitate Ti_2Ni is not [69].

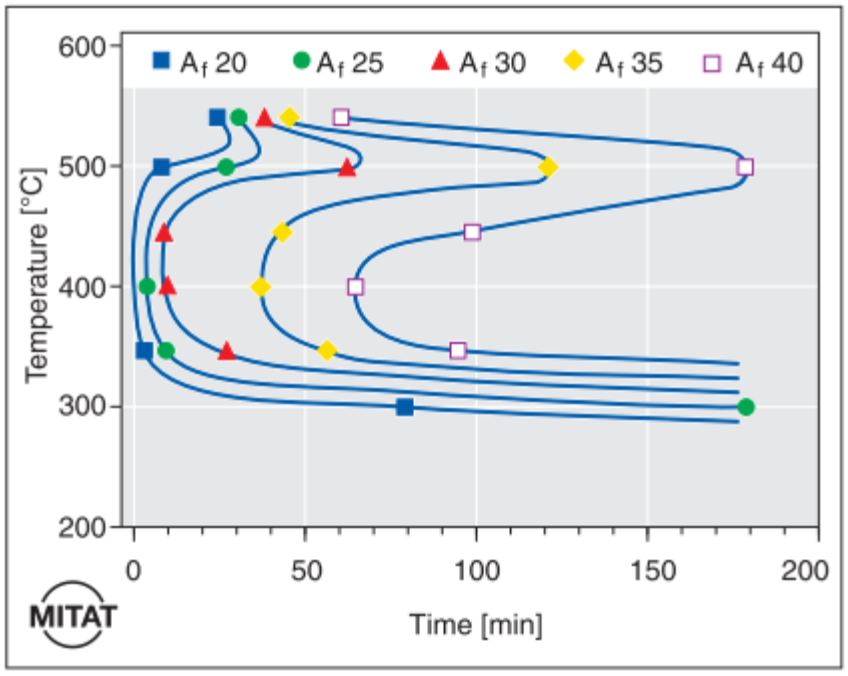

Figure 1.11: Effect of ageing temperature and time on the transformation temperature of Ti-50.8% at Nitinol wire with a starting A_f temperature of 11°C. [70]

In Figure1.11 [70], the effect of aging temperature and time on the transformation temperature of a 50.8% at nickel Nitinol shape memory alloy with A_f of 11°C is shown. There is a maximum precipitation activity at nominally 450°C, above or below which longer heat treatments are needed to increase the A_f. The existence of this optimal temperature is due to competing factors of mobility and driving force; at high temperatures, there is enough thermal energy to permit diffusion of the atoms through the matrix, but this higher atomic mobility also makes it more difficult to form a precipitate nucleus [70]. At lower temperatures, where the tradeoff between surface and volume energy is more favorable, it is easier to form precipitates; but the mobility of the atoms is inhibited. The change in the austenite finish temperature is due to the formation of these nickel-rich precipitates and the resultant leeching of nickel from the matrix of the shape memory alloy.

Section 1.7. Shape Memory Effect at Small Length Scales

At the macroscopic length scale, global measures like stress-strain relationships are used to characterize transformation capabilities. These studies provide valuable information, but are averaged measures that cannot capture the transformation heterogeneity inherent to these materials, nor the dependence of this heterogeneity on the underlying microstructure. As such, an opportunity to control material performance through targeted processing of the microstructure is lost.

At sub-micrometer length scales, studies have provided important information about lattice structure, precipitation, and dislocation activity, and have significantly improved our understanding of the underlying transformation mechanisms behind both the SME and SE effects. This length scale captures fundamental parameters of transformation, but the small field of view precludes the mesoscale analysis of the spatial evolution of transformation and its

relation to microstructure. SMA wire actuators are subjected to thermo-mechanical cycling during their working life, accumulating plastic deformation. This accumulation of plastic deformation with each cycle is attributed to changes in the microstructure of the wire, whereby lattice defects, dislocations, and precipitates are introduced into the matrix and cause significant changes in the capability of the actuator to recover deformation [71], [72]. It is macroscopically evident that residual strain accumulates through thermo-mechanical cycling in SME (for example see [8], [19], [73], [74] and the references contained therein), but the extent of detwinning and accumulation of residual strain at the microstructural length scale in polycrystalline SMAs remains largely uncharacterized.

The shape memory effect has been observed in a range of geometries including nanopillars, nanoscale imprints [75], thin films [76], [77], and microwires, with a varied recovery extent based on considerations including geometry and microstructure. For example, complete shape memory recovery has been observed in tests on micro/nano pillars of a Cu-Al-Ni shape memory alloy [78]. The previously reported problems were attributed to martensite nucleation at this scale to a lack in local crystallinity of the sample or, particularly in the case of NiTi, to local deviations in stoichiometry due to titanium depletion from oxidation, in agreement with recent TEM studies on NiTi thin films [79]. It has also been found, on a modeling study of NiFeGa micropillars, that the influence of micropillar aspect ratio and taper angle on the compression response was significantly smaller than the effect of the micropillar diameter. In a study on the shape memory actuation of Ni-Mn-Ga double beam nanostructures, the SME was observed down to a feature size of 100nm, behavior different from that observed in constrained geometries like films and nanocrystalline shape memory alloys [80]. Work on CuAlMnNi microwires of 45μm to 255μm diameter with a bamboo grain structure demonstrated enhanced thermal actuation of

lightly biased SMA wires in finer wires; this was attributed to both a decrease in the number of interacting martensite variants as well as to relaxation on the free surface [81].

There have been direct TEM observations of damage accumulation in NiTi under mechanical cycling. The density of dislocation increases significantly with thermal and thermal mechanical cycling, and they do not distribute homogeneously [82]. A number of studies indicate that the formation of a dislocation substructure in a SMA, whether through martensitic transformation or plastic deformation of the austenite phase, can act as an obstacle to martensite formation and thereby influence shape recovery [83], [84]. Martensite with an internal structure consisting of either twinning or stacking faults can allow shape recovery, whereas martensites that are truly slipped internally preclude SME [84]. Kajiwara [84] proposed that the shape strain of the nucleating martensite must be accommodated by plastic deformation in the austenite, and therefore any factors that impede this accommodation, including a lack of dislocations, work hardening, or grain refinement, will suppress transformation. Interestingly, it has also been proposed that dislocations can promote the nucleation, formation, and stabilization of martensite, acting as microstructural markers, which allow the material to remember its previous stress strain history. Simon et al. [85] comprehensively described the need to understand the role of dislocations and dislocation substructures in impeding martensitic transformation during thermal cycling, yet promoting the stress-induced formation of martensite during superelastic cycling, a distinction that is not yet understood. Whether dislocation substructures assist or impede phase transformation is under active debate in the SMA community, but it is clear that they play a important role in determining transformation properties and alloy performance.

There is a lack of experimental data that captures interactions between the microstructure of SMAs and the microscale phase transformation characteristics and residual strain

accumulation during shape memory actuation. Experimental data that correlates sub-grain martensitic transformation during the shape memory actuation of NiTi has been challenging to obtain due to the difficulty of capturing full-field microstructure and corresponding full-field microscale strains. As shown in previous work on SE Nitinol, the microscale strain fields are indicative of both transformation location and extent [86]. To investigate the SME response of Nitinol microwires, this doctoral research focused on capturing and analyzing the strain distributions at the microscale in NiTi under cyclic shape memory actuation.

References:

[1] K. Otsuka and C. M. Wayman, *Shape Memory Materials*. Cambridge University Press, 1999.

[2] A. Ölander, "An electrochemical investigatio of solid cadmium-gold alloys," *J. Am. Chem. Soc.*, vol. 54, no. 1906, pp. 3819–3833, 1932.

[3] G. V. Kurdyumov and L. G. Khandros, "On the 'Thermoelastic' Equilibrium on Martensitic Transformations," *Transl. Repr. from Dokl. Akad. Nauk SSSR*, vol. 66, no. 2, pp. 211–214, 1949.

[4] L. Chang and T. Read, "Plastic Deformation and Diffusionless Phase Changes in Metals - The Gold-Cadmium Beta-Phase," *J. Met.*, vol. 3, no. 1, pp. 47–52, 1950.

[5] F. E. Wang, W. J. Buehler, and S. J. Pickart, "Crystal Structure and a Unique "Martensitic'' Transition of TiNi," *J. Appl. Phys.*, vol. 36, no. 10, p. 3232, 1965.

[6] M. M. Schwartz, *Encyclopedia of Smart Materials*. Hoboken, NJ, USA: John Wiley & Sons, Inc., 2002.

[7] J. Ma, I. Karaman, and R. D. Noebe, "High temperature shape memory alloys."

[8] C. B. Churchill, "Experimental Techniques for Characterizing the Thermo-Electro-Mechanical Shakedown Response of SMA Wires and Tubes," *Disssetation - Available Univ. Michigan Libr.*, 2010.

[9] J. Shaw, "Thermomechanical aspects of NiTi," *J. Mech. Phys. Solids*, vol. 43, no. 8, pp. 1243–1281, Aug. 1995.

[10] B. C. Chang, J. A. Shaw, and M. A. Iadicola, "Thermodynamics of Shape Memory Alloy Wire: Modeling, Experiments, and Application," *Contin. Mech. Thermodyn.*, vol. 18, no. 1–2, pp. 83–118, May 2006.

[11] K. Otsuka and X. Ren, "Physical metallurgy of Ti–Ni-based shape memory alloys," *Prog. Mater. Sci.*, vol. 50, no. 5, pp. 511–678, Jul. 2005.

[12] K. Otsuka and X. Ren, "Martensitic transformations in nonferrous shape memory alloys," *Mater. Sci. Eng. A*, vol. 273–275, pp. 89–105, Dec. 1999.

[13] X. Zhang and H. Sehitoglu, "Crystallography of the B2 → R → B19 phase transformations in NiTi," *Mater. Sci. Eng. A*, vol. 374, pp. 292–302, 2004.

[14] J. M. Ball and R. D. James, "Fine phase mixtures as minimizers of energy," *Arch. Ration. Mech. Anal.*, vol. 100, no. 1, pp. 13–52, 1987.

[15] X. Zhang and H. Sehitoglu, "Crystallography of the B2 → R → B19′ phase transformations in NiTi," *Mater. Sci. Eng. A*, vol. 374, no. 1–2, pp. 292–302, Jun. 2004.

[16] P. Šittner, M. Landa, P. Lukáš, and V. Novák, "R-phase transformation phenomena in thermomechanically loaded NiTi polycrystals," *Mech. Mater.*, vol. 38, no. 5–6, pp. 475–492, May 2006.

[17] K. Otsuka and X. Ren, "Recent developments in the research of shape memory alloys," *Intermetallics*, vol. 7, no. 5, pp. 511–528, May 1999.

[18] S. Miyazaki and K. Otsuka, "Deformation and transition behavior associated with theR-phase in Ti-Ni alloys," *Metall. Trans. A*, vol. 17, no. 1, pp. 53–63, Jan. 1986.

[19] K. Bhattacharya, *Microstructure of Martensite: Why it Forms and how it Gives Rise to the Shape-memory Effect*, vol. 6. Oxford, 2003.

[20] K. F. Hane, "Bulk and thin film microstructures in untwinned martensites," *J. Mech. Phys. Solids*, vol. 47, no. 9, pp. 1917–1939, Sep. 1999.

[21] K. M. Knowles and D. A. Smith, "The crystallography of the martensitic transformation in

equiatomic nickel-titanium," *Acta Metall.*, vol. 29, no. 1, pp. 101–110, Jan. 1981.
[22] J. M. Ball and R. D. James, "Fine phase mixtures as minimizers of energy," *Arch. Ration. Mech. Anal.*, vol. 100, no. 1, pp. 13–52, 1987.
[23] J. M. Ball and R. D. James, "Proposed Experimental Tests of a Theory of Fine Microstructure and the Two-Well Problem," *Philos. Trans. R. Soc. A Math. Phys. Eng. Sci.*, vol. 338, no. 1650, pp. 389–450, Feb. 1992.
[24] R. V. Kohn, S. Müller, and S. Muller, "Branching of twins near an austenite—twinned-martensite interface Branching of twins near an aastenite-twinned-martensite interface," *Philos. Mag. A*, vol. 66, no. 5, pp. 697–71, 1992.
[25] J. M. Ball and R. D. James, "A Characterization of Plane Strain," *Proc. R. Soc. A Math. Phys. Eng. Sci.*, vol. 432, no. 1884, pp. 93–99, Jan. 1991.
[26] S. Miyazaki, K. Otsuka, and C. M. Wayman, "The shape memory mechanism associated with the martensitic transformation in Ti-Ni alloys—II. Variant coalescence and shape recovery," *Acta Metall.*, vol. 37, no. 7, pp. 1885–1890, Jul. 1989.
[27] T. Saburi and C. M. Wayman, "Crystallographic similarities in shape memory martensites," *Acta Metall.*, vol. 27, no. 6, pp. 979–995, Jun. 1979.
[28] S. Miyazaki, S. Kimura, F. Takei, T. Miura, K. Otsuka, and Y. Suzuki, "Shape Memory Effect and Pseudoelasticity in a Ti-Ni Single-Crystal," *Scr. Metall.*, vol. 17, no. 9, pp. 1057–1062, 1983.
[29] Y. Liu, J. Van Humbeeck, R. Stalmans, and L. Delaey, "Some aspects of the properties of NiTi shape memory alloy," *J. Alloys Compd.*, vol. 247, no. 1–2, pp. 115–121, Jan. 1997.
[30] M. Nishida, T. Nishiura, H. Kawano, and T. Inamura, "Self-accommodation of B19′ martensite in Ti–Ni shape memory alloys – Part I. Morphological and crystallographic studies of the variant selection rule," *Philos. Mag.*, vol. 92, no. 17, pp. 2215–2233, 2012.
[31] S. Miyazaki, K. Otsuka, and C. M. Wayman, "The shape memory mechanism associated with the martensitic transformation in Ti-Ni alloys—I. Self-accommodation," *Acta Metall.*, vol. 37, no. 7, pp. 1873–1884, Jul. 1989.
[32] O. Matsumoto, S. Miyazaki, K. Otsuka, and H. Tamura, "Crystallography of martensitic transformation in TiNi single crystals," *Acta Metall.*, vol. 35, no. 8, pp. 2137–2144, Aug. 1987.
[33] Y. Matsuzaki, H. Naito, T. Ikeda, and K. Funami, "Thermo-mechanical behavior associated with pseudoelastic transformation of shape memory alloys," *Smart Mater. Struct.*, vol. 10, no. 5, pp. 884–892, Oct. 2001.
[34] K. Gall, "The role of texture in tension–compression asymmetry in polycrystalline NiTi," *Int. J. Plast.*, vol. 15, no. 1, pp. 69–92, Mar. 1999.
[35] L. C. Brinson, I. Schmidt, and R. Lammering, "Stress-Induced Transformation Behavior of a Polycrystalline NiTi Shape Memory Alloy: Micro and Macromechanical Investigations via in situ Optical Microscopy," 2003.
[36] S. W. Robertson, a R. Pelton, and R. O. Ritchie, "Mechanical fatigue and fracture of Nitinol," *Int. Mater. Rev.*, vol. 57, no. 1, pp. 1–37, Jan. 2012.
[37] M. Kimiecik, J. W. Jones, and S. H. Daly, "Quantitative Analysis of Phase Transformation in Ni-Ti Shape Memory Alloys," *Adv. Mater. Process.*, vol. 171, no. 4, pp. 21–24, Apr. 2013.
[38] M. Kimiecik, J. W. Jones, and S. Daly, "Grain orientation dependence of phase transformation in the shape memory alloy Nickel–Titanium," *Acta Mater.*, vol. 94, pp. 214–223, Aug. 2015.

[39] T. W. Duerig, A. Pelton, and D. Stockel, "An overview of nitinol medical applications," *Materials Science and Engineering: A*, 1999.
[40] J. Mohd Jani, M. Leary, A. Subic, and M. A. Gibson, "A review of shape memory alloy research, applications and opportunities," *Mater. Des.*, vol. 56, pp. 1078–1113, Apr. 2014.
[41] T. Waitz, V. Kazykhanov, and H. P. Karnthaler, "Martensitic phase transformations in nanocrystalline NiTi studied by TEM," *Acta Mater.*, vol. 52, no. 1, pp. 137–147, 2004.
[42] C. Chluba, W. Ge, R. Lima de Miranda, J. Strobel, L. Kienle, E. Quandt, and M. Wuttig, "Ultralow-fatigue shape memory alloy films," *Science (80-.).*, vol. 348, no. 6238, pp. 1004–1007, May 2015.
[43] J. Cui, Y. S. Chu, O. O. Famodu, Y. Furuya, J. Hattrick-Simpers, R. D. James, A. Ludwig, S. Thienhaus, M. Wuttig, Z. Zhang, and I. Takeuchi, "Combinatorial search of thermoelastic shape-memory alloys with extremely small hysteresis width," *Nat. Mater.*, vol. 5, no. 4, pp. 286–290, Apr. 2006.
[44] Y. Song, X. Chen, V. Dabade, T. W. Shield, and R. D. James, "Enhanced reversibility and unusual microstructure of a phase-transforming material," *Nature*, vol. 502, no. 7469, pp. 85–88, Oct. 2013.
[45] D. Stoeckel, "The Shape Memory Effect – Phenomenon, Alloys and Applications," *Proceedings: Shape Memory Alloys for Power Systems EPRI* , vol. 683, no. pp.1-13, 1995.
[46] K. Kim and S. Daly, "Martensite Strain Memory in the Shape Memory Alloy Nickel-Titanium Under Mechanical Cycling," *Exp. Mech.*, vol. 51, no. 4, pp. 641–652, 2011.
[47] A. W. Richards, R. A. Lebensohn, and K. Bhattacharya, "Interplay of martensitic phase transformation and plastic slip in polycrystals," *Acta Mater.*, vol. 61, no. 12, pp. 4384–4397, Jul. 2013.
[48] K. Kim, K. A. Juggernauth, and S. H. Daly, "Stress-Induced Martensitic Phase Transformation in Nitinol Under Hard Cyclic Loading," in *ASME 2010 Conference on Smart Materials, Adaptive Structures and Intelligent Systems, Volume 1*, 2010.
[49] J. P. Sethna, K. Dahmen, S. Kartha, J. A. Krumhansl, B. W. Roberts, and J. D. Shore, "Hysteresis and hierarchies: Dynamics of disorder-driven first-order phase transformations," *Phys. Rev. Lett.*, vol. 70, no. 21, pp. 3347–3350, May 1993.
[50] K. Kim and S. Daly, "The effect of texture on stress-induced martensite formation in nickel–titanium," *Smart Mater. Struct.*, vol. 22, no. 7, p. 75012, 2013.
[51] S. W. Robertson, A. Mehta, A. R. Pelton, and R. O. Ritchie, "Evolution of crack-tip transformation zones in superelastic Nitinol subjected to in situ fatigue: A fracture mechanics and synchrotron X-ray microdiffraction analysis," *Acta Mater.*, vol. 55, no. 18, pp. 6198–6207, Oct. 2007.
[52] T. Inamura, Y. Fukui, H. Hosoda, K. Wakashima, and S. Miyazaki, "Relationship between Texture and Macroscopic Transformation Strain in Severely Cold-Rolled Ti-Nb-Al Superelastic Alloy," *Mater. Trans.*, vol. 45, no. 4, pp. 1083–1089, 2004.
[53] Y. Fukui, T. Inamura, H. Hosoda, K. Wakashima, and S. Miyazaki, "Mechanical Properties of a Ti-Nb-Al Shape Memory Alloy," *Mater. Trans.*, vol. 45, no. 4, pp. 1077–1082, 2004.
[54] H. Y. Kim, T. Sasaki, K. Okutsu, J. I. Kim, T. Inamura, H. Hosoda, and S. Miyazaki, "Texture and shape memory behavior of Ti–22Nb–6Ta alloy," *Acta Mater.*, vol. 54, no. 2, pp. 423–433, 2006.
[55] K. Bhattacharya and R. V. Kohn, "Symmetry, texture and the recoverable strain of shape-

memory polycrystals," *Acta Mater.*, vol. 44, no. 2, pp. 529–542, Feb. 1996.
[56] L. Zhao, P. F. Willemse, J. H. Mulder, J. Beyer, and W. Wei, "Texture development and transformation strain of a cold-rolled Ti50-Ni45-Cu5 alloy," *Scr. Mater.*, vol. 39, no. 9, pp. 1317–1323, 1998.
[57] S. H. Chang and S. K. Wu, "Textures in cold-rolled and annealed Ti50Ni50 shape memory alloy," *Scr. Mater.*, vol. 50, no. 7, pp. 937–941, 2004.
[58] L. Brinson, "Stress-induced transformation behavior of a polycrystalline NiTi shape memory alloy: micro and macromechanical investigations via in situ optical microscopy," *J. Mech. Phys. Solids*, vol. 52, no. 7, pp. 1549–1571, Jul. 2004.
[59] H. Paranjape and P. M. Anderson, "Texture and grain neighborhood effects on Ni–Ti shape memory alloy performance," *Model. Simul. Mater. Sci. Eng.*, vol. 22, no. 7, p. 75002, Oct. 2014.
[60] K. Gall, H. Sehitoglu, Y. I. Chumlyakov, I. V. Kireeva, and H. J. Maier, "The Influence of Aging on Critical Transformation Stress Levels and Martensite Start Temperatures in NiTi: Part I—Aged Microstructure and Micro-Mechanical Modeling," *J. Eng. Mater. Technol.*, vol. 121, no. 1, p. 19, Jan. 1999.
[61] A. Ahadi and Q. Sun, "Effects of grain size on the rate-dependent thermomechanical responses of nanostructured superelastic NiTi," *Acta Mater.*, vol. 76, pp. 186–197, Sep. 2014.
[62] H. M. Paranjape, P. P. Paul, H. Sharma, P. Kenesei, J.-S. Park, T. W. Duerig, L. Catherine Brinson, and A. P. Stebner, "Influences of Granular Constraints and Surface Effects on the Heterogeneity of Elastic, Superelastic, and Plastic Responses of Polycrystalline Shape Memory Alloys," *J. Mech. Phys. Solids*, Feb. 2017.
[63] Y. Liu, Z. L. Xie, J. Van Humbeeck, and L. Delaey, "Effect of texture orientation on the martensite deformation of NiTi shape memory alloy sheet," *Acta Mater.*, vol. 47, no. 2, pp. 645–660, Jan. 1999.
[64] R. Delville, B. Malard, J. Pilch, P. Sittner, and D. Schryvers, "Transmission electron microscopy investigation of dislocation slip during superelastic cycling of Ni–Ti wires," *Int. J. Plast.*, vol. 27, no. 2, pp. 282–297, 2011.
[65] D. R. Steinmetz and S. Zaefferer, "Towards ultrahigh resolution EBSD by low accelerating voltage," *Mater. Sci. Technol.*, vol. 26, no. 6, pp. 640–645, Jun. 2010.
[66] P. Surbled, C. Clerc, B. Le Pioufle, M. Ataka, and H. Fujita, "Effect of the composition and thermal annealing on the transformation temperatures of sputtered TiNi shape memory alloy thin films," *Thin Solid Films*, vol. 401, no. 1–2, pp. 52–59, Dec. 2001.
[67] S. Miyazaki and K. Otsuka, "Development of Shape Memory Alloys," *ISIJ Int.*, vol. 29, no. 5, pp. 353–377, 1989.
[68] M. Nishida, C. M. Wayman, and T. Honma, "Precipitation processes in near-equiatomic TiNi shape memory alloys," *Metall. Trans. A*, vol. 17, no. 9, pp. 1505–1515, Sep. 1986.
[69] J. Bhagyaraj, K. V. Ramaiah, C. N. Saikrishna, and S. K. Bhaumik, "Behavior and effect of Ti2Ni phase during processing of NiTi shape memory alloy wire from cast ingot," *J. Alloys Compd.*, vol. 581, pp. 344–351, Dec. 2013.
[70] A. R. Pelton, J. Dicello, and S. Miyazaki, "Optimisation of processing and properties of medical grade Nitinol wire," *Minim. Invasive Ther. Allied Technol.*, vol. 9, no. 2, pp. 107–118, Jan. 2000.
[71] M. F. X. Wagner, S. R. Dey, H. Gugel, J. Frenzel, C. Somsen, and G. Eggeler, "Effect of low-temperature precipitation on the transformation characteristics of Ni-rich NiTi shape

memory alloys during thermal cycling," *Intermetallics*, vol. 18, no. 6, pp. 1172–1179, Jun. 2010.
[72] A. Ibarra, J. San Juan, E. H. Bocanegra, and M. L. Nó, "Evolution of microstructure and thermomechanical properties during superelastic compression cycling in Cu–Al–Ni single crystals," *Acta Mater.*, vol. 55, no. 14, pp. 4789–4798, 2007.
[73] O. W. Bertacchini, D. C. Lagoudas, F. T. Calkins, and J. H. Mabe, "Thermomechanical cyclic loading and fatigue life characterization of nickel rich NiTi shape-memory alloy actuators," in *Proceedings of SPIE - Behavior and Mechanics of Multifunctional and Composite Materials*, p. 692916, 2008.
[74] D. A. Hebda and S. R. White, "Effect of training conditions and extended thermal cycling on nitinol two-way shape memory behavior," *Smart Mater. Struct.*, vol. 4, no. 4, pp. 298–304, Dec. 1995.
[75] C. P. Frick, T. W. Lang, K. Spark, and K. Gall, "Stress-induced martensitic transformations and shape memory at nanometer scales," *Acta Mater.*, vol. 54, no. 8, pp. 2223–2234, May 2006.
[76] J. D. Busch, A. D. Johnson, C. H. Lee, and D. A. Stevenson, "Shape-memory properties in Ni-Ti sputter-deposited film," *J. Appl. Phys. Appl. Phys. Lett. Phys. Lett. Appl. Phys. Lett. J. Appl. Phys*, vol. 68, no. 50, pp. 6224–173102, 1990.
[77] G. A. Shaw, D. S. Stone, A. D. Johnson, A. B. Ellis, W. C. Crone, "Shape memory effect in nanoindentation of nickel–titanium thin films," *Appl. Phys. Lett.*, vol. 83, no. 257, 2003.
[78] J. San Juan, M. L. Nó, and C. A. Schuh, "Superelasticity and Shape Memory in Micro- and Nanometer-scale Pillars," *Adv. Mater.*, vol. 20, no. 2, pp. 272–278, Jan. 2008.
[79] S. C. Mao, H. X. Li, Y. Liu, Q. S. Deng, L. H. Wang, Y. F. Zhang, Z. Zhang, and X. D. Han, "Stress-induced martensitic transformation in nanometric NiTi shape memory alloy strips: An in situ TEM study of the thickness/size effect," *J. Alloys Compd.*, vol. 579, pp. 100–111, Dec. 2013.
[80] E. A. P. Hernandez and D. C. Lagoudas, "Modeling size effects on the transformation behavior of shape memory alloy micropillars," *J. Micromechanics Microengineering*, vol. 25, no. 7, p. 75001, Jul. 2015.
[81] N. Tuncer, L. Qiao, R. Radovitzky, and C. A. Schuh, "Thermally induced martensitic transformations in Cu-based shape memory alloy microwires," *J. Mater. Sci.*, vol. 50, no. 22, pp. 7473–7487, Nov. 2015.
[82] A. R. Pelton, G. H. Huang, P. Moine, and R. Sinclair, "Effects of thermal cycling on microstructure and properties in Nitinol," *Mater. Sci. Eng. A*, vol. 532, pp. 130–138, Jan. 2012.
[83] J. Perkins, "Residual stresses and the origin of reversible (two-way) shape memory effects," *Scr. Metall.*, vol. 8, no. 12, pp. 1469–1476, Dec. 1974.
[84] S. Kajiwara, "Roles of dislocations and grain boundaries in martensite nucleation," *Metall. Mater. Trans. A*, vol. 17, no. 10, pp. 1693–1702, Oct. 1986.
[85] T. Simon, A. Kröger, C. Somsen, A. Dlouhy, and G. Eggeler, "On the multiplication of dislocations during martensitic transformations in NiTi shape memory alloys," *Acta Mater.*, vol. 58, no. 5, pp. 1850–1860, Mar. 2010.
[86] M. Kimiecik, J. W. Jones, and S. Daly, "The effect of microstructure on stress-induced martensitic transformation under cyclic loading in the SMA Nickel-Titanium," *J. Mech. Phys. Solids*, vol. 89, pp. 16–30, 2016.
[87] O. Benafan, A. Garg, R. D. Noebe, G. S. Bigelow, S. A. Padula, D. J. Gaydosh, N. Schell,

J. H. Mabe, and R. Vaidyanathan, “Mechanical and functional behavior of a Ni-rich Ni50.3Ti29.7Hf20 high temperature shape memory alloy,” *Intermetallics*, vol. 50, pp. 94–107, Jul. 2014.

[88] A. Coda, L. L. Toia, G. Ischia, and S. Gialanella, “Effect of Thermomechanical Treatments on the Microstructure of NiTi Wires: a TEM Study,” *SMST-2006 Proc. Int. Conf. Shape Mem. Superelastic Technol. (ASM Int.*, pp. 757–775, 2008.

[89] A. Pelton, “Nitinol for Medical Devices Workshop 4-5 June 2013,” no. June, 2013.

[90] B. M. Barnes, D. E. Brei, J. E. Luntz, K. Strom, A. L. Browne, and N. Johnson, “Shape memory alloy resetable spring lift for pedestrian protection,” in *Industrial and Commercial Applications of Smart Structures Technologies 2008 A4 - Davis, L. Porter A4 - Henderson, Benjamin K. A4 - McMickell, M. Brett*, vol. 6930, pp. 693005–693013, 2008.

[91] C. Aguayo, B. Utter, J. Luntz, R. Gonzalez, D. Brei, N. L. Johnson, and P. W. Alexander, “Damper-controlled switch for SMA motion smoothing,” p. 90590H, 2014.

[92] M. Toma, J. Luntz, D. Brei, P. W. Alexander, A. L. Browne, and N. L. Johnson, “Design and Proof-of-Concept Validation of a Latched Arch Active Seal,” in *ASME 2008 Conference on Smart Materials, Adaptive Structures and Intelligent Systems*, pp. 709–720, 2008.

Chapter 2. Materials and Methods

Section 2.1. SEM-DIC Sample Preparation and Testing

NiTi wires of 500μm diameter were thermo-mechanically loaded through shape memory actuation cycles using an *in-situ* SEM tensile stage. A custom experimental and analysis methodology was used to generate full-field Lagrangian strain maps at the microscale. The wires were 49.5 at% Ni (SM495, black oxide finish, straight wire) manufactured by Nitinol Devices and Components with a 500μm outer diameter and an austenite finish temperature of 84°C ± 5°C as determined by DSC (QA200, TA Instruments). The grain diameter was measured to be 20-40nm (assuming spherical morphology with crystallite shape factor K=0.9) using peak widening of the XRD spectrum, measured using a Rigaku Rotating Anode X-Ray Diffractometer. The diffraction spectrum was obtained at a stage temperature of 300°C; it was not possible to measure the specimen temperature, but 300°C was sufficiently above the temperature at which the numerous martensitic peaks turned to a single austenitic peak in the measured spectrum. The grain diameter was measured using the Scherrer equation (MDI JADE 2010). The wires were cut into sections of 5 ± 0.1 cm length with a low speed diamond saw (South Bay Technologies, Model #650).

Distortion-corrected Digital Image Correlation (DIC) combined with scanning electron microscopy (SEM), termed here as SEM-DIC, was used to quantify high-resolution, full-field strains in fields of view on the order of of tens of microns. DIC is a non-contact, full-field

surface displacement measurement technique, wherein a random pattern is applied to the specimen surface and tracked as the specimen is deformed. Deformations were calculated by minimizing correlation functions between subsets of the applied pattern, providing a high degree of spatial resolution in the resulting strain fields. As the method is length scale independent and solely depends on the tracking of the applied pattern, it can be applied to microscale fields of view with no theoretical loss in accuracy – however, in practice, the use of DIC with SEM introduces a number of distortion and noise error sources that require correction [1]–[3].

Two-dimensional DIC was used to analyze the SEM micrographs, and thus it was important to obtain flat surfaces on the sample to minimize the potential errors introduced by projection of a curved surface onto a two-dimensional image. The wires were first mounted onto an aluminum block, and then mechanically polished to produce one flat surface before being flipped over and polished to produce the second flat surface. The first flat surface helped to ensure that the wires rested stably, so that the resultant two flat surfaces were parallel to each other, in order to minimize tilt of the field of interest with respect to the observation plane in the SEM. After the initial removal of material, the second flat surface was further polished as follows: the samples were mechanically polished with a Buehler (EcoMet 250) mechanical polisher using grits of 600 (Buehler CarbiMet 2), 800 (Buehler MicroCut Discs), and 1200 (Buehler MicroCut Discs). Following the 1200 grit polish, the wires were then vibratory polished (Pace Technologies GIGA-0900) for twelve hours using a non-crystallizing colloidal silica solution (Buehler MasterMet 2, Non-Crystallizing Colloidal Silica Polishing Suspension, particle size <1μm). This polishing technique created flat surfaces along the longitudinal axis of the wires for later displacement mapping via nanoparticle tracking, as described in the next paragraph. To examine the microscale characteristics of transformation, the field of interest had

to be comparable to the length scale of material microstructure, yet large enough to provide a statistically relevant field of view. In the characterization of all test specimens analyzed herein – the fine-grained samples in Chapters 3 and 4 as well as the heat-treated, coarse-grained samples in Chapter 5 – the field of interest was 70um by 70um. To ensure that the same area was examined throughout the tests, platinum fiducial markers were deposited onto the flat surfaces to mark the areas of interest, using focused ion beam (FIB) deposition in an FEI Quanta 3D SEM.

For the microscale tracking in this work, gold nanoparticles (NPs) were self-assembled on a chemically functionalized surface following the procedure outlined in [4] for deformation tracking. The gold nanoparticles were fabricated following the Frens technique [5] at an optimal size dictated by the field of view, image resolution, and the roughly 3x3 rule of thumb for digital image correlation [6], which states that one should aim for roughly 3x3 'camera' pixels in a speckle, and roughly 3x3 speckles in a subset. The size of the gold nanoparticles could be manipulated down to 20 nm during fabrication through the addition of sodium citrate, as determined by Frens [5], whose data the authors plotted in Figure 2.1 to facilitate nanoparticle fabrication of the correct size. The sample surface was pretreated in 100°C air in a box furnace (Spiro-Therm HTE46, McEnglevan) in order to promote the growth of a layer of TiO_2 and subsequent hydroxide (-OH) group to serve as a substrate surface to which silane molecules could attach. The samples were then soaked in a methanol 4:1 APTMS to add a coat of silane molecules to the hydroxide groups, cleaned with methanol to remove excess silane molecules, and soaked in the suspension of gold nanoparticles to deposit the speckle pattern. The silane molecules served as an adhesive between the substrate surface and the gold nanoparticles, resulting in a random, isotropic pattern at a controlled density and size for high-resolution microscale deformation tracking. An example of a nanoparticle self-assembly on a NiTi wire

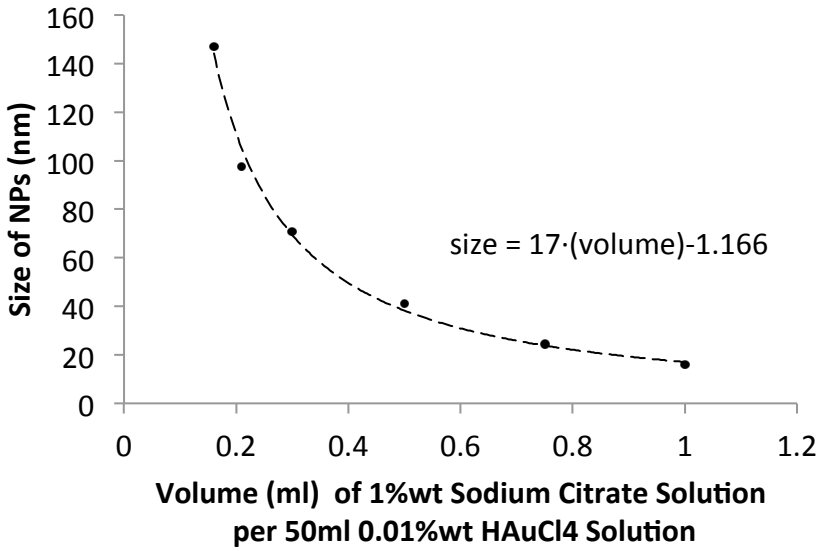

Figure 2.1: Nanoparticle size is controlled by the ratio of sodium citrate to $HAuCl_4$. Data points originally reported by Frens [5] are plotted and fit with an exponential relationship for ease of nanoparticle fabrication of the appropriate size.

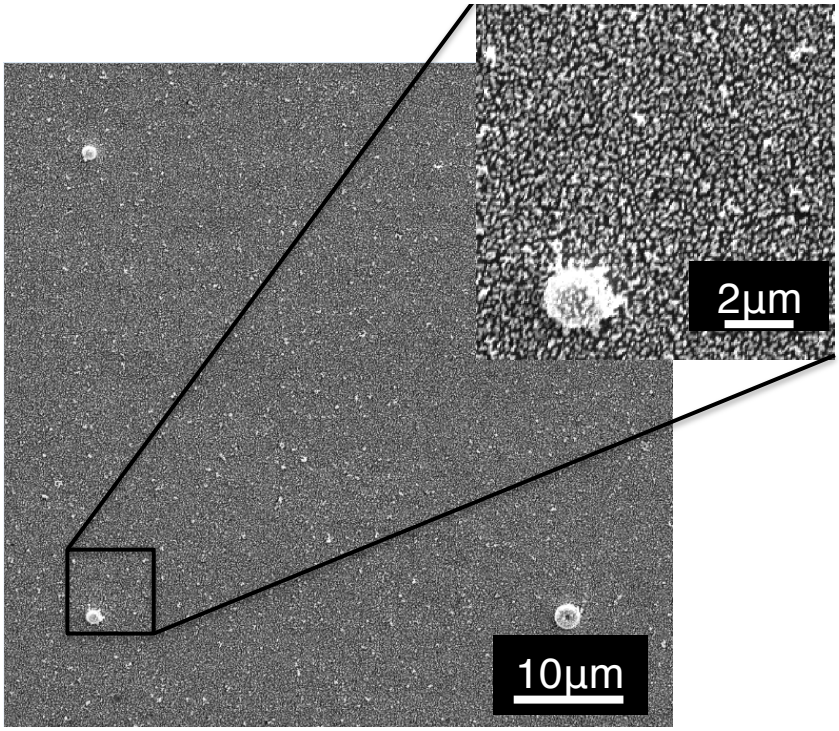

Figure 2.2: An example of a self-assembly of approximately 100nm diameter gold nanoparticles used for microscale deformation mapping via SEM-DIC. The larger white dots at the four corners of the field of view are platinum markers that were FIB-deposited to designate the field of view.

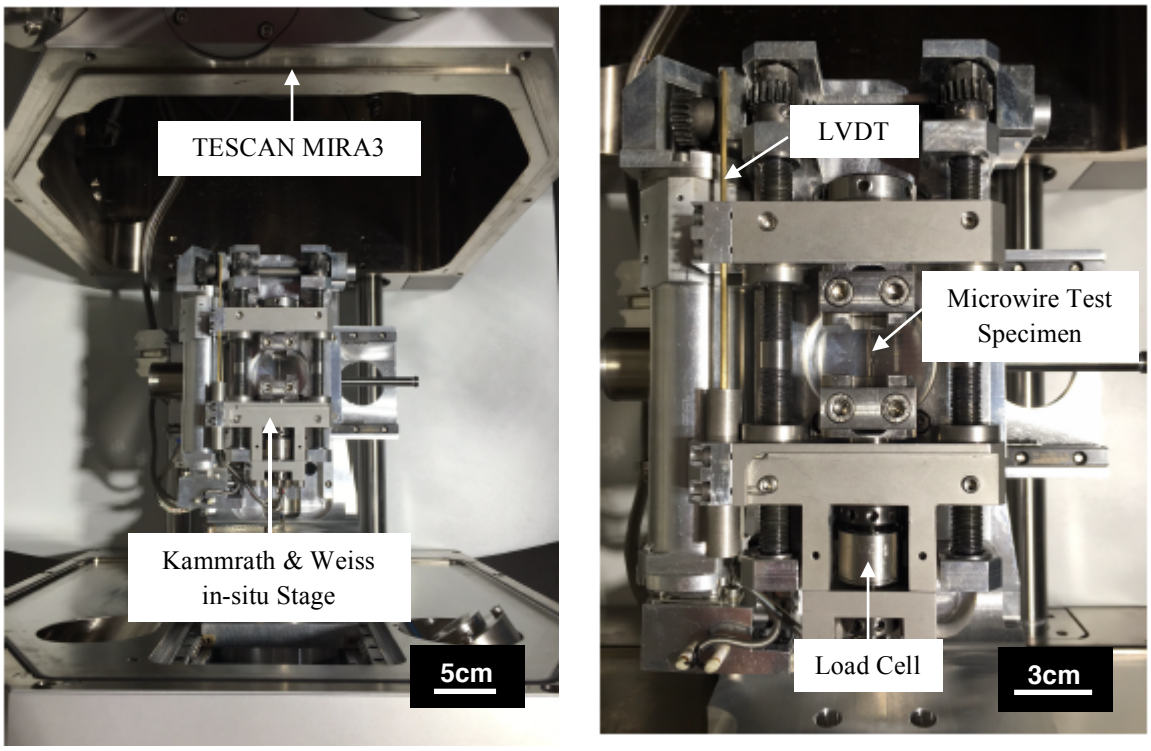

Figure 2.4: In-SEM testing was performed using a tensile stage (Kammrath and Weiss) with a tension-compression load cell (Honeywell model# 3108-10) in the scanning electron microscope (Tescan MIRA3) as shown above.

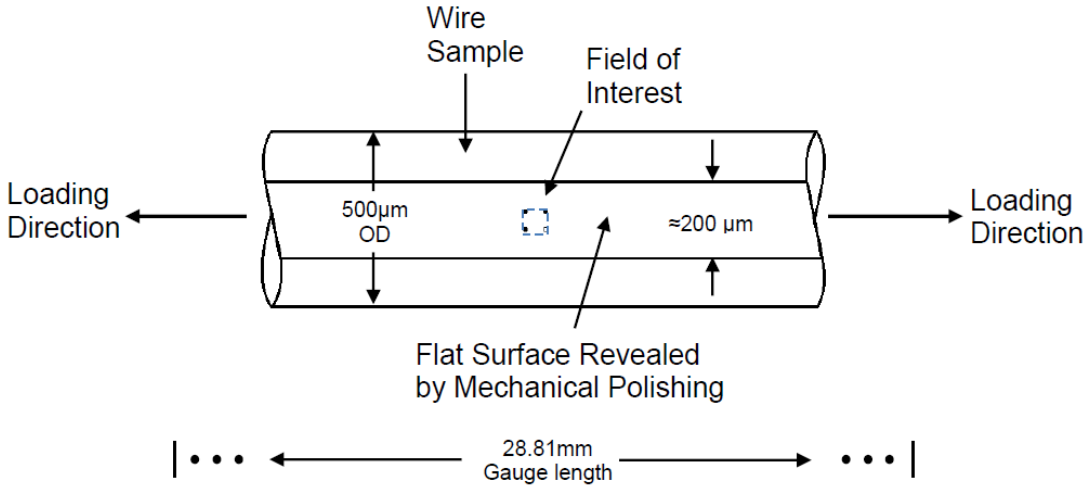

Figure 2.3: Schematic of the microwire specimen geometry, test field of view, and uniaxial loading condition. The 34µm by 34µm field of view was located on the flat surface as illustrated. Gage length represents the distance between the crossheads of the *in-situ* load frame, measured by caliper with a resolution 0.03mm.

specimen is shown in Figure 2.2. Note the larger light colored dots are the platinum fiducial markers.

To obtain microscopic strain data, the specimens were tested in the experimental setup shown in Figure 2.3, with the specimen geometry and test field of view shown schematically in Figure 2.4. The wires were loaded in-SEM to a globally applied axial strain of 0.06 using displacement control at a strain rate of 10^{-4} s^{-1}. After reaching a globally applied axial strain of 0.06, the sample was unloaded until the stage load cell read 0 N, then removed from the tensile tester and heated to 200±2.3˚C (measured using K-type thermocouple, Omega) to allow strain recovery. SEM images of the area of interest were acquired at steps of 100 μm during loading, and after strain recovery when the sample was heated above A_f. In order to acquire SEM images, the specimen was held at constant displacement for approximately ten minutes at each step to allow for relaxation and to prevent image shifting in the field of view. Microscale testing was performed in a Tescan MIRA3 GMH SEM, with a spot size of 7nm, an image size of 70μm x 70μm, pixel resolution of 2048 x 2048 pixels, scan speed of 4 (dwell time 3.2μsec), pixel size of 34.2 nm, beam current of 187μA, voltage of 10 keV, and a 2x frame integration. Images were collected at 70μm x 70μm to optimize nanoparticle size to pixel ratio, and later reduced to 34μm by 34μm for analysis on the region with the optimal nanoparticle pattern. The location of data collection on the specimen is shown schematically in Figure 2.4. The captured micrographs were first processed by commercial digital image correlation software (Vic-2D) [7], following which spatial and time-dependent distortions inherent to SEM imaging were corrected using in-lab codes. Validation of and procedures for distortion correction are detailed in [3] and are based on a framework originally developed by Sutton et al [1], [2]. The undeformed (twinned) martensite was taken as the reference configuration of zero strain. Lagrangian surface strains were

calculated using the corrected displacement information. The in-SEM stress-strain responses obtained using the load from the SEM stage load cell, and the global (LVDT measured grip displacements) and local (DIC-averaged in the FOV) strains, are shown in Figures 3.1 and 3.3 and discussed in Chapter 3. As expected, the global strains are larger, likely due to a small amount of grip slippage (on the order of 10 μm) of the microwires.

Section 2.2. SEM-DIC Error Analysis

The purpose of the work described in this section was to investigate the impact of error and noise on the experimental results, in order to characterize the degree of uncertainty associated with the experimental results in following chapters, and to aid in the choice of optimal imaging parameters in the future.

Despite challenges inherent in the emerging use of in-SEM digital image correlation to characterize microscale deformations, the power and potential of the methodology has spurred significant interest in addressing these challenges, including the errors in digital image correlation and how to minimize them. Currently, most of the effort has been spent on understanding error in macroscale digital image correlation. Digital image correlation can calculate surface displacements with sub-pixel accuracy. However, the algorithm relies on the grey scale values at each pixel to identify material points. Thus, it is important to ensure the correct representation of the behavior of a material point in a digitized SEM image. As previously mentioned, SEM images are generated by an electron beam scanning the area of interest, and this error is complicated and challenging to quantify due to the complexity of SEM imaging. There exist distortion errors that affect the accuracy of the spatial representation of

features on SEM images that lead to errors in the resulting analysis of these features. It is therefore necessary to investigate the characteristics of error in SEM imaging.

Due to the relative complexity of the scanning electron microscope, in addition to the complexity in determining error in the digital image correlation method itself, error analysis for deformation tracking using correlation of SEM images has been extremely challenging. An important first step is to characterize and optimize SEM parameters in order to minimize error in the image capture process. SEM images are generated by collecting secondary electrons (SE) emitted from the specimen surface that result from the incidence of a high-energy electron beam with a diameter on the order of nanometers. The electrons are produced at the top of the SEM column, and then accelerated and passed through a series of electromagnetic lenses and apertures, in order to produce the final incident beam, referred to as the electron probe. The objective lens and its inherent aberrations play a large role in determining the final diameter of the electron probe and thereby in the spatial resolution of the SEM, similar to the objective of a transmission electron microscope or an optical microscope. The scan coils of the SEM raster the beam across the surface of the sample, by creating a magnetic field using fluctuating voltage, in order to manipulate the electron beam and collect the image dot by dot, row by row.

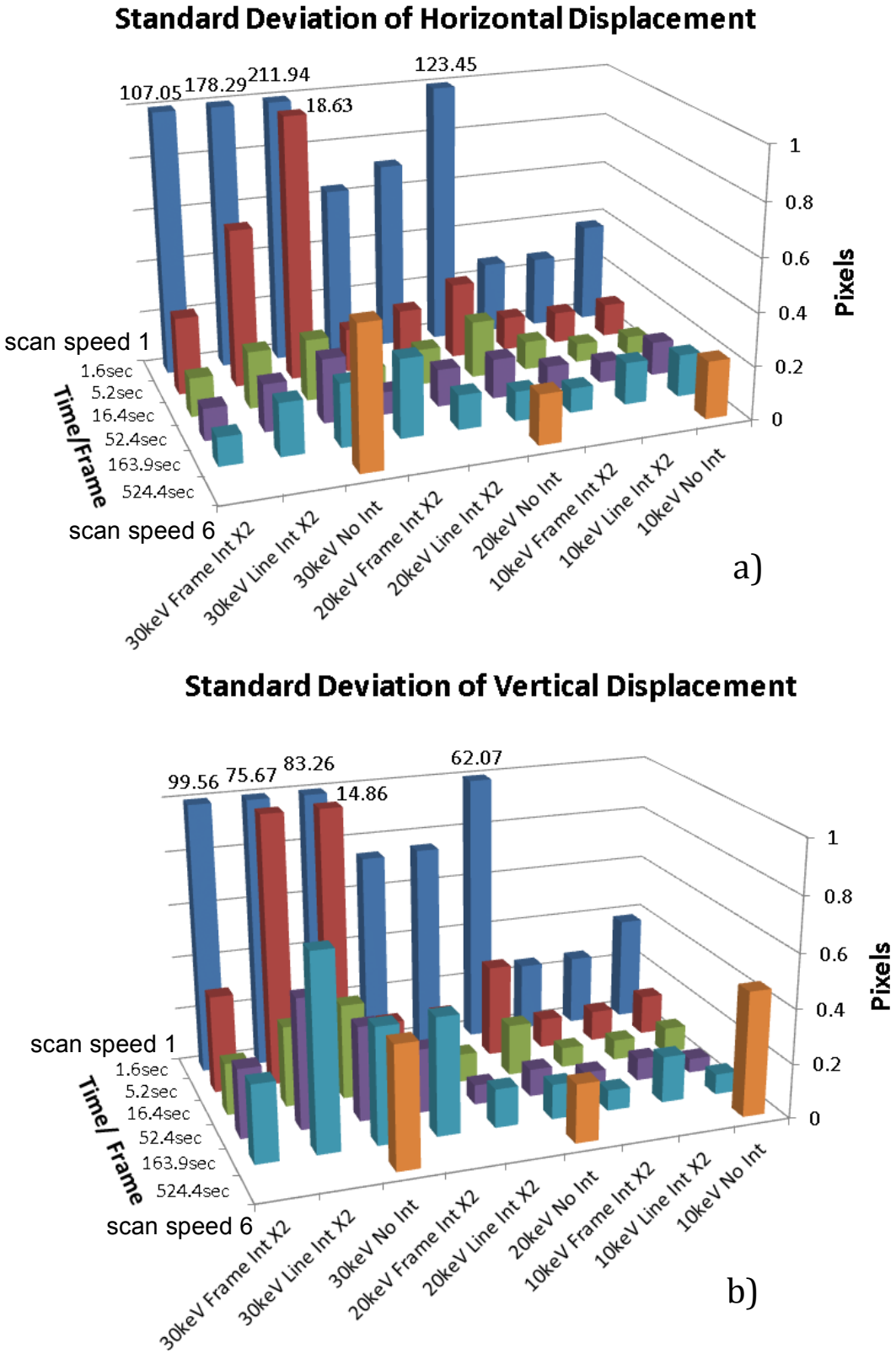

Figure 2.5: Standard deviations of the vertical and horizontal displacements that result from examination of an Inconel test specimen with no strain applied under varying the SEM (model Tescan Mira3D) imaging parameters.

Error in Scanning Electron Microscopy Digital Image Correlation (SEM-DIC) results is highly dependent on imaging parameters. Kammers et al. [3] discussed error analysis for SEM-DIC using micrographs obtained with a FEI Quanta3D SEM. It was shown that SEM image distortions, as discussed by [1], [2], can introduce significant error into SEM-DIC displacement fields. The impact of a range of SEM settings on image noise was quantified, and noise minimization schemes were discussed. The results show that noise in SEM imaging can be, in general, lowered by utilized a high beam current (large spot size), long dwell time, and image integration.

As errors vary based on the SEM in use, the purpose of this error analysis was to investigate the optimal settings for the SEM used in this work (Tescan model Mira3), in order to provide an evaluation of the degree of uncertainty for this microscope and to provide a pathway for future users to determine optimal imaging parameters. The parameters investigated were: beam voltage, scan speed (dwell time), frame integration, and line integration. These were chosen based on the accessibility of these parameters at the user interface while considering the parameters used by [3]. The parameters were varied in a range chosen such that the total time needed take one image would not exceed 25 minutes. Note that the magnitude of error varies with both the pixel number in an image and the physical sizes of the area of interest; here, these two parameters were determined by the requirement for DIC analysis for the NiTi experiments. It should also be noted that in the user interface of the Tescan Mira3, the beam current is not modified directly, but is rather determined by voltage and a parameter denoted ‘beam intensity.’ An electron beam with higher beam intensity generally deposited larger amounts of residual carbon on the substrate surface, and it is therefore not recommended to acquire images using high beam intensities. Additionally, the Mira3 SEM offers a function of averaging images

(image integration) along horizontal lines of pixels. Instead of averaging the images by frame, line integration averages at each scan line before moving on to the next line. This integration method is advantageous when the detected morphology of the area of interest changes during imaging, for example due to stress relaxation while the specimen is being held at a constant load. Using line integration, a clearer image can be captured versus using frame integration.

To obtain error in SEM-DIC displacement analysis under various imaging parameters, SEM images were taken of a gold nanoparticle pattern on a substrate surface of Inconel. The area of interest was 70μm×70μm (2048 pixels × 2048 pixels) and was coated with gold nanoparticles using the same technique for patterning NiTi samples. Three SEM images were taken of the same area of interest using the same imaging parameters. Imaging voltage was considered at 10kV, 20kV and 30kV. Scan speed was varied (decreasing) from "Scan Speed 1" to "Scan Speed 6", where the dwell time for these scan speeds are: 0.1μs, 0.32μs, 1μs, 3.2μs, 10μs, 32μs, respectively. The effect of integration was examined with "no integration", "2× line integration" and "2× frame integration". To limit imaging time to less than 25 minutes, images were not taken under "Scan Speed 6" with line or frame integration. It should be mentioned that although effort was made to keep the area of interest un-moved, images still had visible rigid body displacement. After image acquisition, the images were analyzed using digital image correlation. Under faster scan speeds, poor image quality contributed to difficulty in image correlation; a consistent subset size of 29 pixels and step size of 2 pixels was used across all images. Using the correlated data, the standard deviations of horizontal and vertical displacements were calculated; points where no correlation results could be generated were not counted for calculation. All results are tabulated in bar plots, as shown in Figure 2.5.

The standard deviation of the displacement values, denoted σ, in a full-field strain map was taken to represent the extent of the noise level in the analyzed image. The average and standard deviation of sigma were also calculated.[2]

In Figure 2.5, the x-axis indicates the voltage and frame or line integration used. The y-axis indicates the scan speed, i.e. the time taken in seconds to capture a frame. A frame is defined as data captured when the electron beam has scanned through the field of view once. An image is defined here as the final product that is captured when (and if) the frames are averaged. Therefore, the time/frame for SEM parameters with no integration is equal to the time taken to capture the final image, whereas the time/frame for SEM parameters with ×2 frame integration would be half that required for the final image. The standard deviation of the displacement is analyzed from the final images.

Lowering the imaging voltage, increasing the dwell time, and using more integration (both line and frame) was found to decrease the noise error for the SEM-DIC analysis presented here. However, line integration was found to be the better choice over frame integration; caution should be taken using frame integration when there is significant drift, surface charging or material relaxation, as images can be exceedingly blurry and the average of two images at different locations should be taken.

The standard deviation of the displacements mapping with the Tescan Mira3 SEM used in this work showed a minima when using scan speed three or four, and 10kV imaging voltage. In the scanning speed, the SEM-DIC results generated using the Mira3 SEM showed a minima in

[2] Note that this is different from the sigma value at a data point given by the Vic2D software, termed sigma[pixel], which provides feedback on the data quality as the 1-standard deviation confidence in the match at this point, in pixels [7]. For sigma[pixel], a value of zero indicates a perfect match, whereas higher numbers indicate noise, excessive gradients, or a potentially failed correlation.

the standard deviation of displacements at a scan speed of 3 for horizontal displacement, and a slightly slower scan speed of 4 for vertical displacement. As a possibly related error, there was also evident a clear crosshatch pattern in the calculated rigid body displacement fields (Figure 2.6 scan speed 5 and 6), as well as artificial displacement fields showing as horizontal lines, both of which were present when testing a range of metallic alloy specimens using this machine and a separate Tescan SEM Mira3D in another laboratory. These crosshatch patterns became more prominent as the dwell time was increased, and were at regular spacing that remained consistent. In this work, all SEM images were taken using 2× frame integration with a scan speed of 4 (52.4 seconds per frame), in order to minimize the noise represented by the first principal strain which manifests as a cross hatch pattern in the Tescan model microscope, as shown in Figure 2.6.

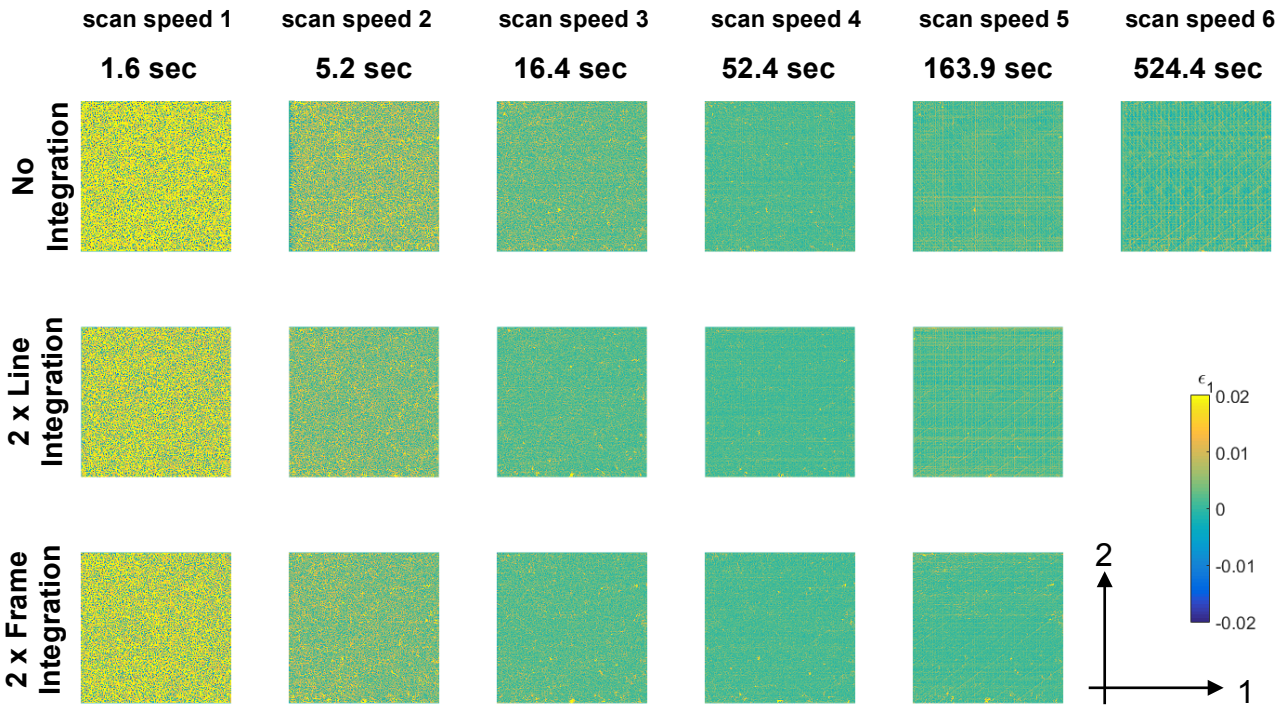

Figure 2.6: Noise introduced using various scan speed (column) and integration (row), demonstrated in the form of principal strain. The time data for each column represent the time used to collect a single frame without considering integration. Noise of more than 0.02 principal strain was introduced to the system with scan speed 1. Noise is minimized using scan speed 4. There are clear cross hatch patterns using scan speeds 5 and 6, hence demonstrating increased resultant noise in principal strain.

References:

[1] M. A. Sutton, N. Li, D. Garcia, N. Cornille, J. J. Orteu, S. R. McNeill, H. W. Schreier, X. Li, and A. P. Reynolds, "Scanning Electron Microscopy for Quantitative Small and Large Deformation Measurements Part II: Experimental Validation for Magnifications from 200 to 10,000," *Exp. Mech.*, vol. 47, no. 6, pp. 789–804, Mar. 2007.

[2] M. A. Sutton, N. Li, D. C. Joy, A. P. Reynolds, and X. Li, "Scanning Electron Microscopy for Quantitative Small and Large Deformation Measurements Part I: SEM Imaging at Magnifications from 200 to 10,000," *Exp. Mech.*, vol. 47, no. 6, pp. 775–787, Mar. 2007.

[3] A. D. Kammers and S. Daly, "Digital Image Correlation under Scanning Electron Microscopy: Methodology and Validation," *Exp. Mech.*, vol. 53, no. 9, pp. 1743–1761, Jul. 2013.

[4] A. D. Kammers and S. Daly, "Self-Assembled Nanoparticle Surface Patterning for Improved Digital Image Correlation in a Scanning Electron Microscope," *Exp. Mech.*, vol. 53, no. 8, pp. 1333–1341, 2013.

[5] G. Frens, "Controlled Nucleation for the Regulation of the Particle Size in Monodisperse Gold Suspensions," *Nature*, vol. 241, no. 105, pp. 20–22, Jan. 1973.

[6] H. Schreier, J.-J. Orteu, and M. A. Sutton, *Image Correlation for Shape, Motion and Deformation Measurements*. Boston, MA: Springer US, 2009.

[7] Vic-2D 2009., Correlated Solutions Inc., Columbia, South Carolina, USA

Chapter 3. Microscale Characteristics of the Shape Memory Effect in Fine-Grained NiTi Wires

An experimental investigation into the microscale transformation characteristics of polycrystalline fine-grained NiTi microwires of 500μm diameter during shape memory cycling is discussed, with emphasis on the characterization of a pronounced heterogeneity in the strain distribution evident during detwinning of the martensite phase upon application of load and its persistence throughout the actuation cycle. Using SEM-DIC (Scanning Electron Microscopy - Digital Image Correlation), full-field strain maps at the microscale were obtained during shape memory cycling. It was found that the strains induced by detwinning were quite heterogeneous at the microscale, and could display a large degree of similarity with thermo-mechanical cycling that tended to increase as cycling progressed. Residual strain concentrated at locations where strain accumulation from detwinning and plasticity were significant, indicating that martensitic detwinning and the associated plasticity that occurs with it is spatially correlated to the subsequent accumulation of residual strain at the microscale.

Section 3.1. Spatial Heterogeneity of Strain During 1st Actuation Cycle

There was a pronounced heterogeneity in the strain distribution evident at the microscale caused by detwinning of the martensite phase upon application of load. Detwinning is known to be directional with respect to texture, where it is enhanced for certain directions and reduced for others; this is the first direct observation, to the best of the authors' knowledge, of the extent of

that anisotropy at the microscopic length scale encompassing several grains. This heterogeneity is shown in Figure 3.1, where the principal Lagrangian (ε_1) strains incurred by martensite detwinning during a full actuation cycle (cycle 1) are shown for a 34μm × 34μm field of view. Points in the macroscopic loading curve correspond with the microscale strain maps labeled A-F. Point A, when the specimen is macroscopically considered twinned martensite, is taken as the reference (zero strain) map. All subsequent strain maps in this work also reference the unloaded, room temperature specimen of twinned martensite as the reference/zero strain. The field of view was captured in the approximate horizontal and vertical center of the wire specimen that had a gage length of 28.81 ± 0.03mm as shown in Figure 2.4, and contained 990,025 data points (995 × 995 pixels). Each data point was approximately 34 nm × 34 nm; therefore the magnitude of strain was taken to indicate the relative extent of deformation, including significant heterogeneity in the degree to which detwinning took place; there are nominally 5μm regions that showed little to no incurred strain (denoted in blue), whereas immediately adjacent regions showed strains on the order of 0.08 (denoted in yellow).

The heterogeneous distribution of strains resulting from detwinning remained consistent throughout the SME cycle, although the magnitudes changed. At point B, the specimen is nominally midway through the macroscopic deformation process, and the evolution of the heterogeneous strain field is apparent. At point C, further load has been globally applied, and the strain field now has the same distribution but a greater magnitude of heterogeneity, where local high strain regions from point B intensify. At point D, upon unloading, the strain magnitude lessens slightly, but its distribution remains consistent. The amount of strain each data point recovered upon unloading (Figure 3.1, from map C to D) showed no dependence on how much strain was initially present at that data point in map C; each data point reduced by nominally the

same amount. Even upon heating the specimen (point E), wherein there is a reversion back to the (primarily) austenite phase and subsequent recovery of the deformation, there remains a faint 'ghost' pattern of the induced strain. Note that maps E and F in Figure 3.1 are at a reduced strain scale of [-0.02, 0.02], versus maps A-D at a strain scale of [-0.05, 0.1].

At points E and F, the strain magnitude is greatly reduced, but the heterogeneity remains the same as in point C, when the specimen was primarily in the detwinned martensite phase at maximum load. When the specimen cools (point F) and macroscopically reverts back to twinned martensite, the ghost pattern seen at point E from the initial loading and subsequent detwinning remains, with a reduction in averaged strain from point E to point F (cooling and overall transformation from austenite to twinned martensite) of 0.55% to 0.39%. The strains at maximum load (map C) were largely recovered upon heating and subsequent cooling of the specimen and its reversion back to twinned martensite, with a small degree of residual strain from locked-in martensite and plasticity remaining, as evident in map F and in the macroscopic stress-strain-temperature curves at top of Figure 3.1.

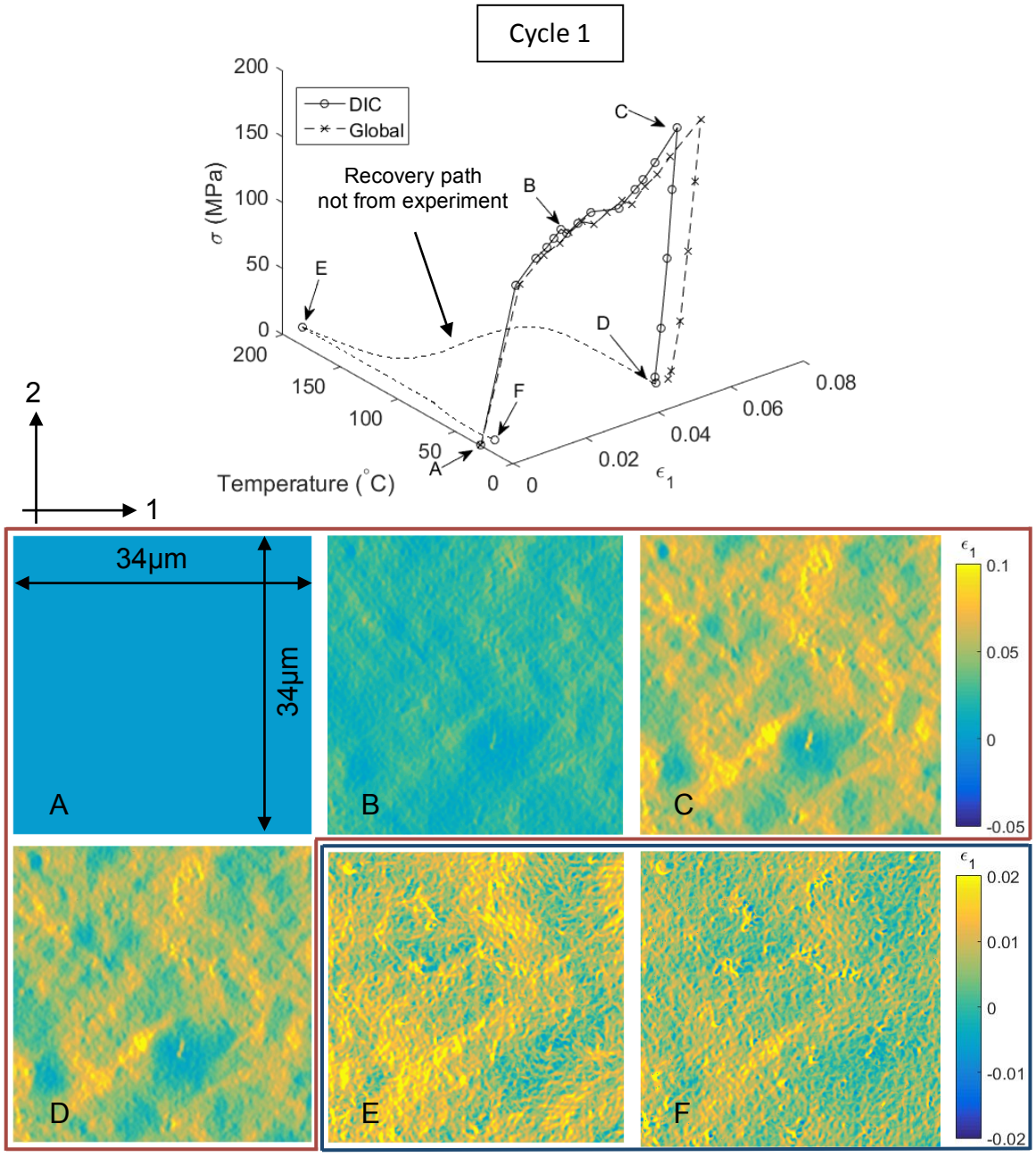

Figure 3.1: Microscale strain maps corresponding to the designated points in the stress–strain temperature curve. There was a pronounced heterogeneity in the strain distribution evident at the microscale, caused by detwinning of the martensite phase upon application of load. This heterogeneous strain distribution remained constant throughout the entire actuation cycle, although the strain magnitude changed. Residual strain concentrated at locations where strain accumulation from detwinning and plasticity were significant.

Residual strain concentrated at locations where strain accumulation from detwinning and plasticity were significant, as evident in a comparison between Figure 3.1 C (where significant stress-induced detwinning has taken place) and Figure 3.1 F (where the specimen has been heated and cooled, and has reverted back to primarily austenite with a corresponding recovery in shape). Note that Figures 3.1 C and Figure 3.1 F use different strain scale bars in order to highlight the similarity in the pattern of strain; however, the magnitudes of the residual strain in Figure 3.1 F are much reduced compared to Figure 3.1 C at maximum load. The persistence of the strain pattern indicates that the process of martensitic detwinning in a SME cycle, and the associated plasticity that occurs with it, is spatially correlated to the subsequent accumulation of residual strain at the microscale. As shown in Figure 3.2, the recovered strain (Figure 3.1, strain map F subtracted from strain map C) showed a linear dependence with the maximum strain (Figure 3.1, strain map C) at each individual data point. In Figure 3.2, each of the nearly one million data points in the map is individually plotted; recall that the reference (zero strain) image was taken as the initial twinned state before the start of cycle 1. The z-axis (normalized count calculated with respect to the total number of data points) indicates the proportion of data points that fall into each strain data bin of 0.0004 x 0.0004 in size. Therefore, the grid of recovered strain [-0.01, 0.11] and maximum strain [-0.01, 0.11] are sectioned into 300 x 300 bins. Significant strain recovery accompanied the stress-induced detwinning at nearly all points in the field of view, as indicated by the linearity of the heat map; for example, the largest number of data points on cycle 1 (constituting 4.3% of the total number of data points and labeled with the black arrow on Figure 3.3), had a maximum strain of 0.059 and a recovered strain of 0.053.

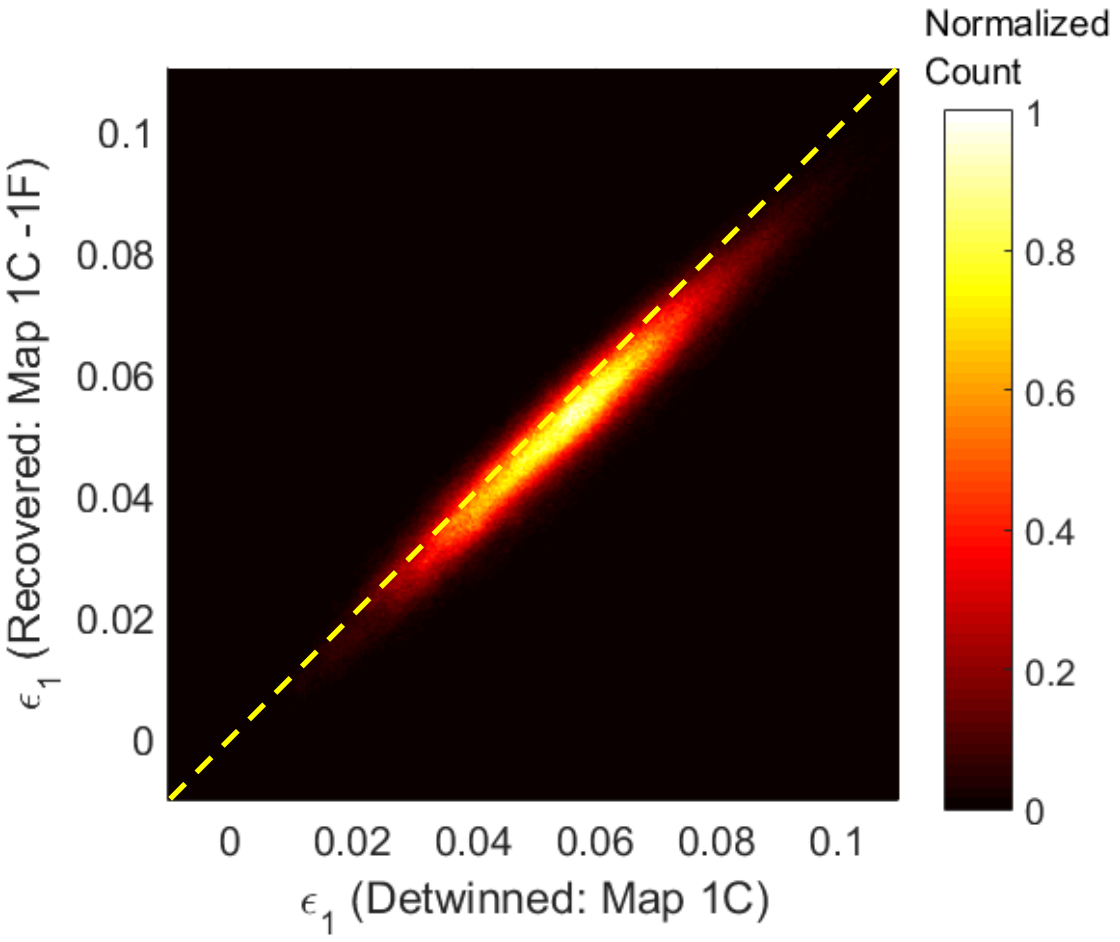

Figure 3.2: A heat map of the strain at each data point in cycle 1 is shown, where the color indicates the normalized count of the number of data points with those x- and y- values. The x-axis is the value of the point at strain map C (detwinned martensite at maximum load), and the y-axis is the value at that point of strain map of F subtracted from strain map C (where f is the twinned martensite after heating and subsequent cooling). Deformation was largely recovered after heating, and the recovered strain between maps C and F showed a strong linear dependence on the maximum strain of the detwinned martensite (map C).

Despite the local strain heterogeneity, the averaged DIC-calculated strains matched the globally acquired strains well, as shown in the macroscopic stress-strain curve for cycle 1 in Figure 3.1. The global strain was calculated from the displacement of the crossheads of the in-SEM testing stage as measured by LVDT. In both cases, the applied nominal stress was calculated from the applied load measured by the in-SEM stage load cell, divided by the initial cross sectional area of the wire. The DIC and global curves were in reasonable agreement, with discrepancy attributed to two factors; one, that the DIC-obtained strains were only captured and averaged in a 34 μm field of view, whereas the global strains were taken across the entire 28.81±0.03 mm gage section, in a process that is mesoscopically heterogeneous; and two, that due to the practical difficulty of gripping wires for testing, there was likely grip slippage, wherein only 10-20 μm of slippage would account for the differences in strain. As one would expect in this case, the global curve shows the larger strain values.

Section 3.2. Cycle-to-Cycle Similarity During Subsequent Actuation

Once established in the first actuation cycle, the same microscale pattern of strain reappeared in subsequent cycles, as shown in Figure 3.3. Here, the microscale strains of the (primarily) detwinned martensite at the maximum load (strain maps at point C) and of the (primarily) twinned martensite of the unloaded sample (strain maps at point F) are shown side by side during the first, second and fifth actuation cycles. Note that all maps are correlated with respect to the original reference image of the undeformed, twinned specimen as shown in Figure 3.1 A. Also, for ease of comparison, the strain maps in Figure 3.3 are shown with two different scale bars; the maximum strain at map C is shown with a relatively broad scale bar of ε_1 = [-0.05, 0.1] and the residual strain at map F is shown with a scale bar of ε_1 = [-0.02, 0.02]. The same microscale pattern of strain reappeared at both the maximum load and the recovered specimen, with an intensification of the residual strain in map F from cycle 1 to cycle 5. The averaged strain over the field of view for both maps increased from cycle 1 to cycle 5, from a strain of 0.0543 to 0.0561 (map C) and from 0.0039 to 0.0080 (map F), respectively.

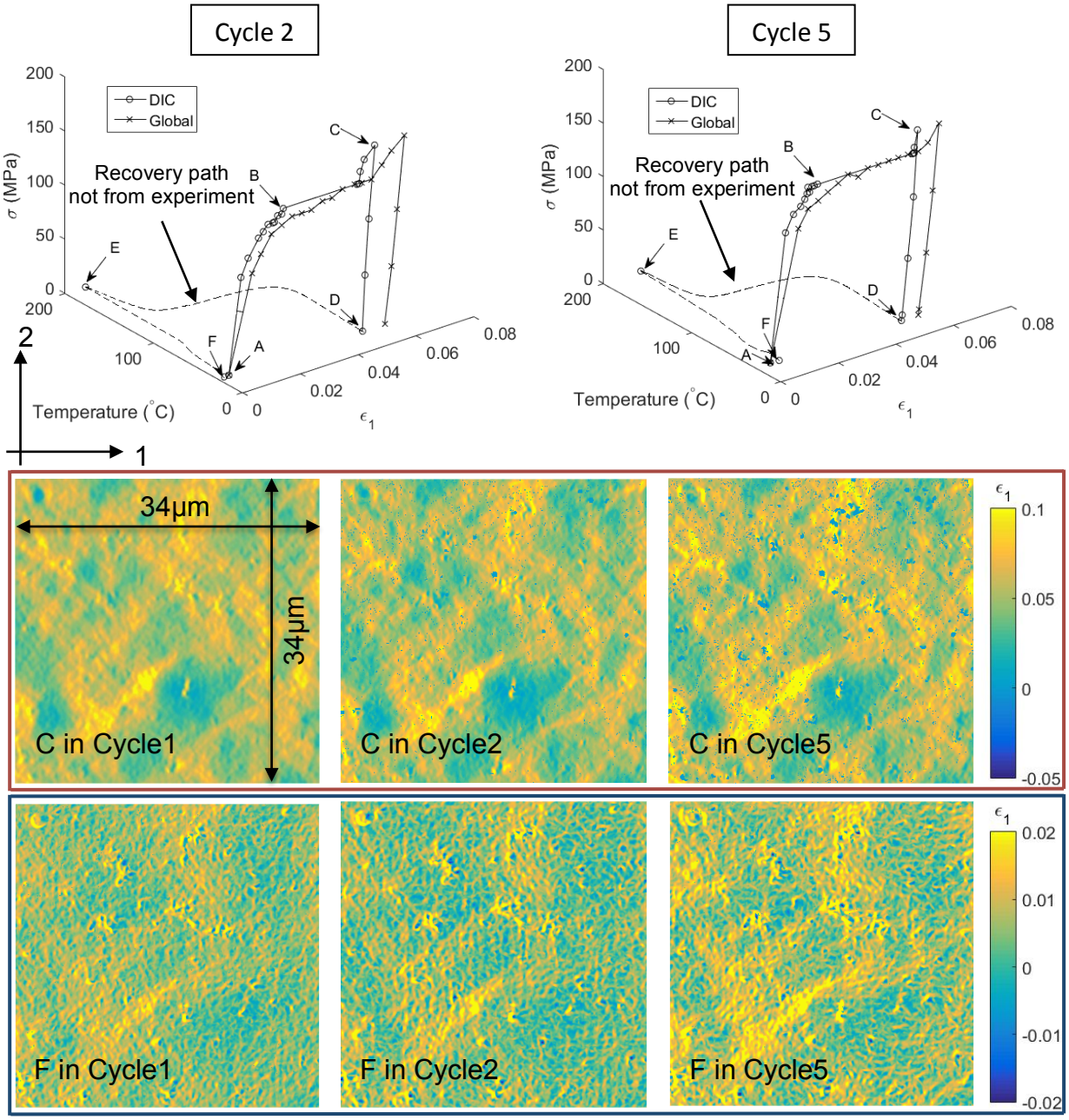

Figure 3.3: The strain maps acquired in the detwinned martensite at maximum applied load (map C) as well as in the twinned martensite after mechanical unloading, heating, and cooling (map F). The same microscale pattern of strain reappeared at both the maximum load and the unloaded specimen, with an intensification of the residual strain in map F from cycle 1 to cycle 5. The averaged strain over the field of view for both maps increased from cycle 1 to cycle 5, from a strain of 0.0543 to 0.0561 (map C) and from 0.0039 to 0.0080 (map F), respectively.

Correlation coefficients calculated point-by-point were used to quantify the persistence of microscale strain heterogeneity from cycle to cycle, as shown in Figure 3.4 for cycle 1 and cycle 2. Correlation coefficients were calculated when the specimen was at maximum load at a given cycle, i.e. between the strain maps at point C in Figures 3.1 and 3.3. The magnitude of the strain maps at point C varied depending on the cycle number, as expected given the small field of view, heterogeneity of transformation, and accumulation of residual strain; however, the strains averaged over the field of view were similar. The maps at point C in Figures 3.1 and 3.3 were taken at maximum load on the specimen, which was measured as DIC-averaged strain values over the field of view of 0.0543 (cycle 1), 0.545 (cycle 2), and 0.561 (cycle 5). The correlations calculated point-by-point between cycles 1 and 2 are shown in the form of a heat map in Figure 3.4. This map shows the number of data points (counts) on the z-axis that fall into a certain *x*-*y* bin, where *x* is the correlation coefficient between the cycles at their maximum load (e.g strain map C in Figure 3.1), and *y* is the maximum strain at that point in the first actuation cycle. Note that the correlation coefficient neglects the effect of strain magnitude, but instead reports the similarity between the trends of two data sets. The correlation coefficient at a data point *(x,y)* represents the linear dependence of the strain at that point at the two cycles under comparison, and ranges between -1 to +1. A correlation coefficient approaching +1 indicates that the strains are strongly positively correlated, and a correlation coefficient of 0 indicates that the strains have no correlation. The z-axis (normalized count) indicates how many data points fall into each data bin of 0.00125 (strain) by 0.01 (correlation coefficient) in size. Therefore, the grid of correlation coefficient [-1, 1] and strain [0, 0.15] are sectioned into 200 × 120 bins.

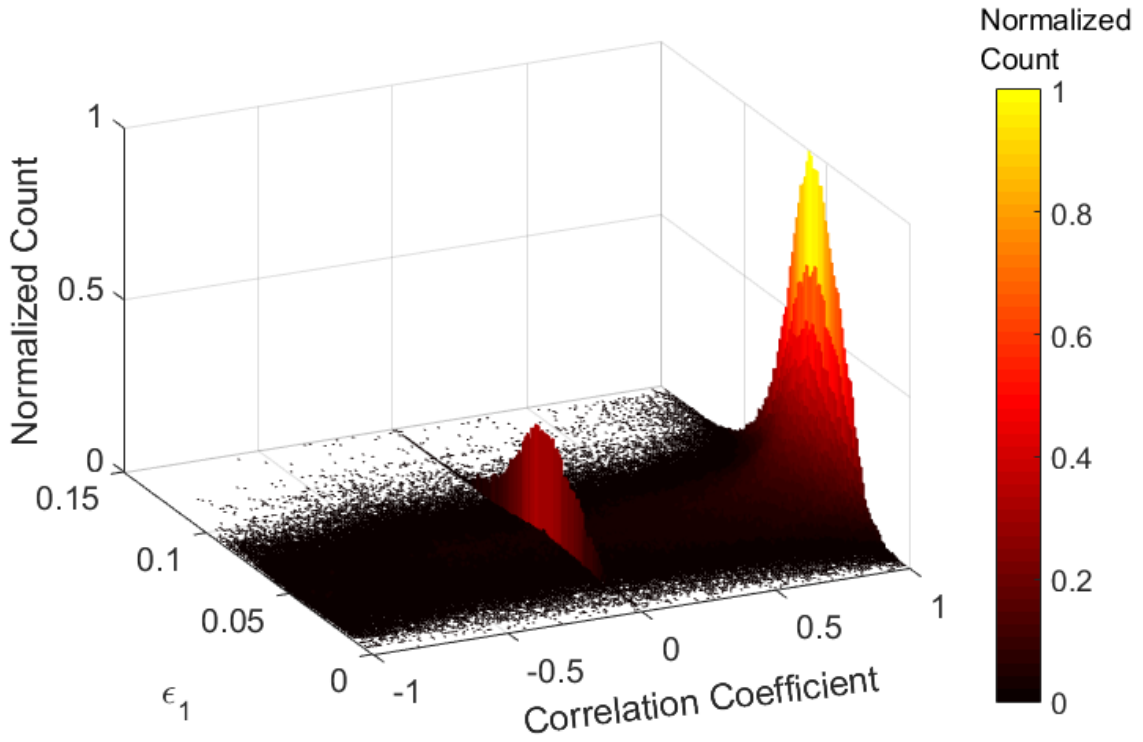

Figure 3.4: A heat map of the point-by-point correlation coefficients between microscale strain maps C for cycles 1 and 2 (in Figure 3.3). There is a strong point-to-point similarity between cycles 1 and 2, as observed in Figure 3.3 and tabulated here. The "Correlation Coefficient" axis refers to the correlation coefficient between the strains at each selected data point in cycles 1 and 2, and the "ε_1" axis refers to the strain at that same data point in cycle 1. The z-axis, "Normalized Count", tabulates the number of pixels that fall into each of these axes values. A small number of points that failed digital image correlation, or did not show a correlation to each other, constitute a short peak around a correlation coefficient of 0.

The two maximum strain maps (C) have strong point-to-point similarity between cycles 1 to 2, as observed in Figure 3.3 and graphically illustrated in Figure 3.4. Figure 3.4 shows a heat map of the point-by-point correlation coefficients between microscale strain maps C for cycles 1 and 2 (shown in Figure 3.3), which were taken at maximum DIC-averaged strains of 0.0543 (cycle 1) and 0.0545 (cycle 2). The "Correlation Coefficient" axis refers to the correlation coefficient between the strains at each selected data point in cycles 1 and 2, and the "ε_1" axis refers to the strain at that same data point in cycle 1. The z-axis, "Normalized Count", tabulates the number of pixels that fall into each of these axes values. The majority of the correlation coefficient values in the map belong to a large peak close to 1, indicating a very strong similarity of the maps for most data points. In this cluster of data points, 51.9% of the data points have a 'strong' correlation coefficient (greater than 0.8), 40.4% of the data points have a correlation coefficient greater than 0.9, and 29.4% have a correlation coefficient greater than 0.95. A small number of points (2.7% of the total number of points) that failed digital image correlation constitute a short peak around a correlation coefficient of 0. When the points that failed digital image correlation where excluded from this plot, the peak disappeared.

Correlation coefficients between each individual data point tended to increase with thermo-mechanical cycling. For example, in cycle 1 vs. cycle 2 as shown in Figure 3.4, 40.4% of data points had a correlation coefficient greater than 0.9, and 29.4% of data points had a correlation coefficient greater than 0.95. The percentage of data points with high correlation coefficients increased between cycles 4 and 5, where 44.2% of data points had a correlation coefficient greater than 0.9, and 32.5% of data points had a correlation coefficient greater than 0.95. This shift of distribution towards higher percentages of strong correlation coefficients indicates that there is a 'settling in' process, where the similarity of strain induced by detwinning

and plasticity becomes stronger as cycling progresses. This also indicates that, if strain accommodation can be controlled in the first actuation cycle by the appropriate microstructural design, then this control can carry through subsequent cycles for potentially the lifetime of the shape memory component. Future work is needed to investigate the relationship between detwinning and microstructural landscape, and the effect of microstructural and material characteristics on the persistence of accommodated strain with repeated shape memory actuation.

Section 3.3. Chapter Summary

The microscale transformation characteristics of Nitinol wires of 500μm diameter were examined during shape memory actuation cycles via a novel method combining scanning electron microscopy, distortion-corrected digital image correlation, and the self-assembly of nanoparticles on the specimen surface through chemical functionalization. These tests resulted in the following findings:

- The work provides, to the best of our knowledge, the first direct observation of full-field strain distribution at the microscale of SME NiTi during thermo-mechanical cycling.

- There was a pronounced heterogeneity in the strain distribution evident at the microscale caused by martensitic detwinning upon load application. At maximum load when there was a large amount of detwinning, there was significant heterogeneity in the strains, which are indicative of the degree to which detwinning took place; there were micron-sized regions (encompassing numerous grains with a grain diameter of 20-40 nm) that showed little to no incurred strain, whereas immediately adjacent regions showed strains on the order of 0.08.

- The heterogeneous distribution of strain (as referenced back to a zero strain configuration of the twinned martensitic sample at the beginning of cycle 1) remained consistent throughout the SME cycle, although the magnitudes of strain changed. The amount of strain each data point recovered upon unloading (Figure 3.1, from map C to D) showed no dependence on how much strain was initially present at that data point at maximum load in cycle 1 (map C); each data point reduced by nominally the same amount.

- Residual strain concentrated at locations where strain accumulation from detwinning and plasticity were significant. The persistence of the strain pattern indicates that the process of martensitic detwinning in a SME cycle, and the associated plasticity that occurs with it, is spatially correlated to the subsequent accumulation of residual strain at the microscale.

- In addition to persisting throughout a single cycle, the same microscale pattern of strain reappeared in subsequent actuation cycles as evident in Figure 3.3.

- Correlation coefficients between each individual data point tended to increase with thermo-mechanical cycling. For example, in cycle 1 vs. cycle 2 as shown in Figure 3.4, 40.4% of data points had a correlation coefficient greater than 0.9, and 29.4% of data points had a correlation coefficient greater than 0.95. The percentage of data points with high correlation coefficients increased between cycles 4 and 5, where 44.2% of data points had a correlation coefficient greater than 0.9, and 32.5% of data points had a correlation coefficient greater than 0.95. This shift of distribution towards higher percentages of strong correlation coefficients indicates that there is a ‘settling in’ process, where the similarity of strain induced by detwinning and plasticity becomes stronger as cycling progresses.

References

[1] L. Brinson, “Stress-induced transformation behavior of a polycrystalline NiTi shape memory alloy: micro and macromechanical investigations via in situ optical microscopy,” *J. Mech. Phys. Solids*, vol. 52, no. 7, pp. 1549–1571, Jul. 2004.

[2] M. . Kimiecik, J. W. . Jones, and S. . Daly, “Quantitative Analysis of Phase Transformation in Ni-Ti Shape Memory Alloys,” *Adv. Mater. Process.*, vol. 171, no. 4, pp. 21–24, Apr. 2013.

[3] M. Kimiecik, J. W. Jones, and S. Daly, “The effect of microstructure on stress-induced martensitic transformation under cyclic loading in the SMA Nickel-Titanium,” *J. Mech. Phys. Solids*, vol. 89, pp. 16–30, 2016.

[4] M. Kimiecik, J. Wayne Jones, and S. Daly, “Grain orientation dependence of phase transformation in the shape memory alloy Nickel–Titanium,” *Acta Mater.*, vol. 94, pp. 214–223, Aug. 2015.

Chapter 4. Microscale Repeatability in Fine-Grained Shape Memory NiTi

Section 4.1. Introduction and Background

This chapter focuses on the characteristics of the microscale transformation in the fine-grained NiTi microwires introduced in Chapter 3. The relationships between transformation, residual deformation, and cycling are investigated.

Section 4.2. Material and Experimental Procedure

The microwires were of the same batch as those examined in Chapter 3; in short, they were 500μm OD (outer diameter) straight wires with composition 49.5 at.%Ni and 50.5 at.%Ti (54.5 wt.%Ni, 45.5 wt.%Ti), as stated by the supplier. The grain diameter was approximately 20-40 nm, and the composition was determined to be 50.0 at.%Ni and 50.0 at.%Ti (55.1 wt.%Ni, 44.9 wt.%Ti). The austenite and martensite finish temperatures were 84°C ± 5°C and 35°C ± 5°C, respectively. The wires were tested in 5±0.1cm sections. A low-speed diamond saw at 150 rpm was used to section the test specimens. They were then mounted and polished as described in Chapter 2. Gold nanoparticles (NPs) of ~100nm diameter were chemically attached to the specimen surface in order to generate patterns at the appropriate length scale for displacement mapping via digital image correlation inside the scanning electron microscope, at a 70μm×70μm field of view using 2048×2048 pixels. The imaging parameters used in the tests were: dwell time 36μs, line integration 2 times, 10keV beam voltage, 2048 × 2048 pixel and 70μm × 70μm image size, pixel size 34.2nm, spot size 7 nm, and a beam intensity of 10 (beam current 187.6μA).

These parameters were selected by analyzing the magnitude of error using a matrix of combinations as described in Chapter 2.

In-SEM thermo-mechanical cycling tests were performed under displacement control at a strain rate of 10^{-4}/s. Mechanical loading of the wire was paused every 100μm displacement for nominally ten minutes to allow for material relaxation before a SEM image was taken. It took approximately 4.5 minutes to collect an image. The sample was loaded to a global strain of 0.06 before being mechanically unloaded to a global strain of 0. The sample was then taken out of the SEM and stage, and heated to a temperature of 200±2.3°C. SEM images were taken at both the heated (primarily austenite) and subsequently cooled (primarily twinned martensite) configurations. This process was repeated for five actuation cycles. All tests were performed using a Kammrath and Weiss micro tensile heating and straining stage in a SEM.

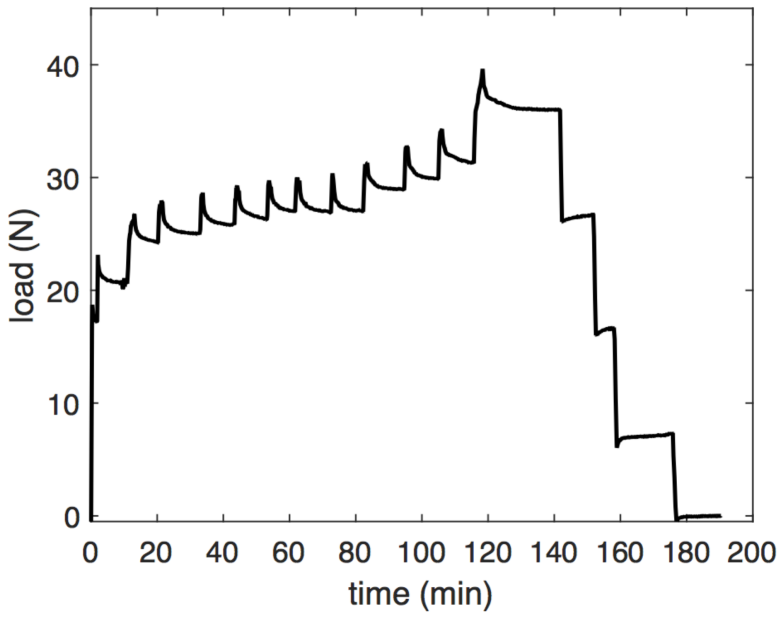

Figure 4.1: Mechanical loading of the wire was paused every 100μm displacement for nominally 10 minutes to allow for material relaxation before a SEM image was taken. This figure is mechanical loading/unloading path of the first cycle of the sample presented in this chapter under room temperature.

The resulting micrographs were first processed using commercial digital image correlation software (Vic 2D 2009, Correlated Solutions) to obtain preliminary full-field displacement maps. After a parametric study of our conclusions based on varied subset and step size, 15 and 2 were selected, respectively, as a balance between spatial fidelity and displacement value precision.

Section 4.3. Results and Discussion

Section 4.3.1. Linearity between Strains Accommodated by Detwinning with Cycling

It was shown in Chapter 3 that there was a pronounced heterogeneity in the strain distribution evident at the microscale caused by detwinning of the martensite phase upon the application of load. Additionally, this strain heterogeneity persisted throughout cycling with a large degree of similarity. This can be seen in Figure 4.2, which was performed on a different fine-grained test specimen than that in Chapter 3, but which was from the same batch of material (as were all tests in this thesis) and which are consistent with those earlier findings. Note that the reference (zero strain image) was taken as the twinned martensite before the start of cycle 1, and the map thereby shows the microscale strain accommodated by the detwinned martensite upon the application of load. In the maps in Figure 4.2, the designation on the bottom right hand side of each map refers to the cycle and point in the map, shown in the global stress-strain-temperature curve at top. For example, map 2D is the strain map of cycle 2, point D, which is the mechanically unloaded state after maximum load (primarily detwinned martensite). As evident in the top figures of Figure 4.2, point A is prior to mechanical loading (twinned martensite), point B is mid-way through the stress plateau caused by mechanical loading, point C is at maximum mechanical load

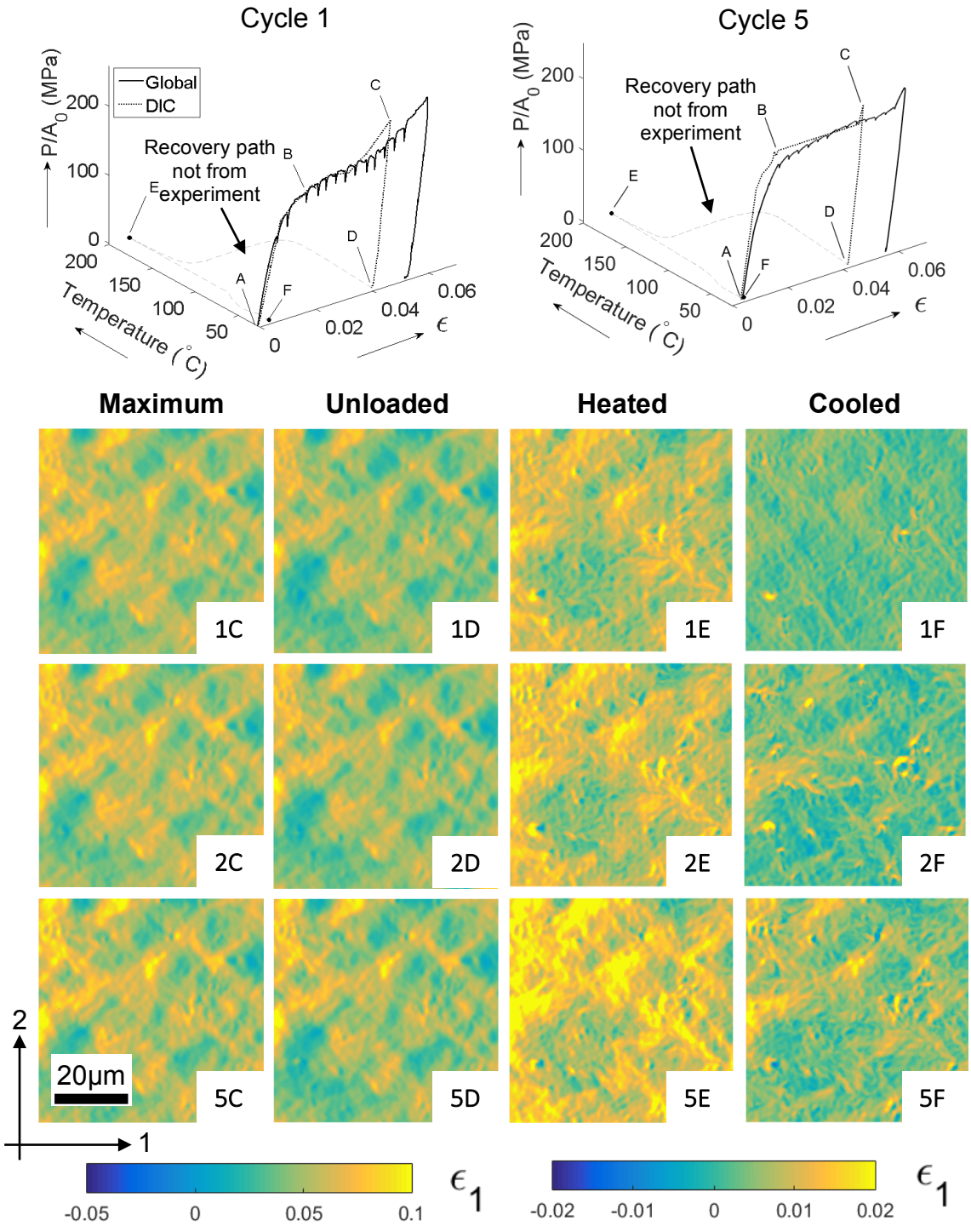

Figure 4.2: Stress-strain-temperature plots of cycles 1 and 5, as well as the full-field strain maps at designated stress-strain-temperature states.

(detwinned martensite/elastic/plastic), point D is the subsequently unloaded state (detwinned martensite/plastic), point E is subsequently heated to reversion back to the austenite state, and point F is the cooled austenite state that has reverted back to twinned martensite.

There is a linear relationship with cycling between the strains accommodated in the detwinned state. That is, there exists a strong linear correlation between the point-by-point strains at the detwinned, mechanically unloaded state (point D in Figure 4.2). Otherwise stated, there is a high probability that the strain demonstrated at a material point in the (overall) detwinned state will correspond strongly to the relative level of strain of that point at the same state in the subsequent cycles. This is shown in Figure 4.3, which shows two plots that are referred to as 'heat maps.' In heat map 4.3(a), the x- and y-axes indicate the principal strain value (ε_1) at a point acquired at two different cycles as designated in the axes labels. The color of the heat map at each point indicates the number of data points with those strain values, and is normalized by the maximum number of data points present at any single point in the strain map. This point-by-point linearity is strong between cycles 1 and 2 (Figure 4.3a) and becomes even stronger between cycles 4 and 5 (Figure 4.3b). The adjusted R^2 value between cycles 1 and 2 is 0.892, and that for cycles 4 and 5 is 0.927.

The adjusted R^2 value refers to the equation below, where *n* is the number of data points and *d* is the order of the fitted polynomial. In this case, *d*=1 as a linear polynomial was used. The variable $\hat{y}_i$ is the expected value of *y* from the model at data point *i,* and $\bar{y}$ is the overall mean of all data points.

$$R^2_{adjusted} = 1 - \frac{\sum_{i=1}^{n}(y_i - \hat{y}_i)^2}{\sum_{i=1}^{n}(y_i - \bar{y})^2} \cdot \frac{n-1}{n-d-1};$$

$$R^2 = 1 - \frac{\sum_{i=1}^{n}(y_i - \hat{y}_i)^2}{\sum_{i=1}^{n}(y_i - \bar{y})^2};$$

For comparison, the same analysis was conducted to compare the linear relationship between other states in the thermal mechanical cycles, as shown in Table 4.2. The analysis in Table 4.2 was also performed on two other SEM-DIC data sets collected on two other samples from the same material batch (as-received, fine grained). The linearity increase with cycling for map D is consistent throughout all tests. Map C data is shown to highlight that the trend did not remain consistent for the maximum loaded detwinned state (point C): for two specimens, the linearity decreased with cycling (data in Tables 4.1 and 4.2), while for one specimen, the linearity increased (Table 4.3). The decrease of linearity with cycling when cycle 1 is fixed (i.e., between cycle 1 and cycle 5), while maintaining high R^2 values, indicates that although the deformation accommodated by the detwinned martensite exhibits a high degree of similarity from cycle to cycle, there is evolution and deviation from the initial first cycle that is possible.

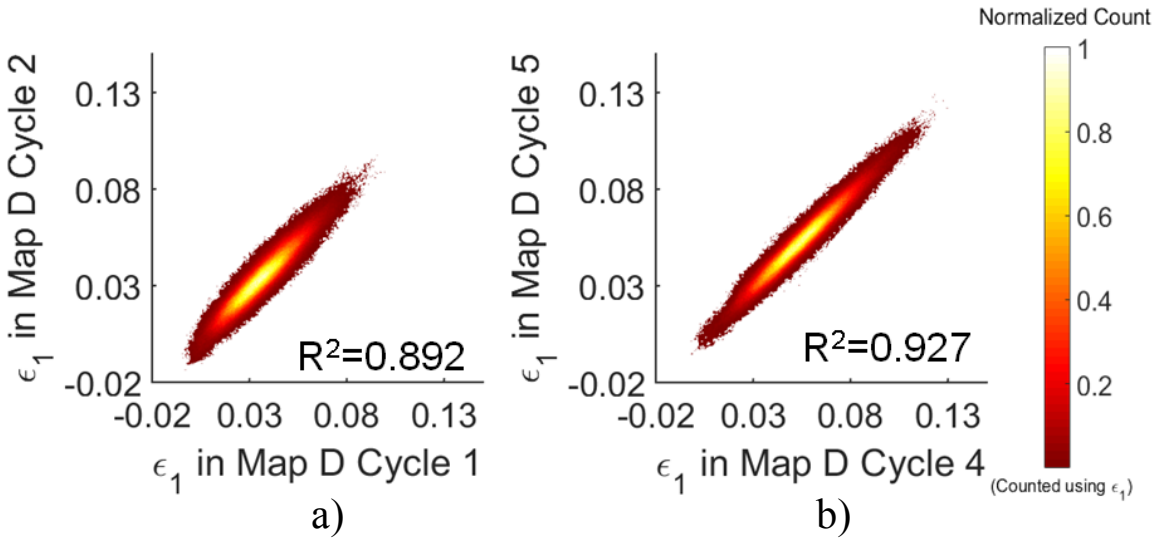

Figure 4.3: The linear relationship between the detwinned strain maps (map D) in adjacent cycles grow with cycling. Strain in map D (maximum detwinned, mechanically unloaded) in Table 4.2 during adjacent cycles are plotted on the x-axis against the strains at detwinned state in maps D indicated on the y-axis. The color scheme represents the normalized count of the numbers of strain data points that fall into one of the 200 by 200 data bins divided along x and y axes. The normalization was calculated using the maximum number of strain data points among all the bins in each subfigure.

Table 4.1 First Dataset (shown in Figure 4.2) Adjusted R^2 values

	cycle 1~2	cycle 1~5	cycle 4~5
Maps D	0.892	0.767	0.927
Maps C	0.956	0.872	0.953

Table 4.2 Second Dataset (shown in Figure 4.3) Adjusted R^2 values

	cycle 1~2	cycle 1~5	cycle 4~5
Maps D	0.975	0.918	0.981
Maps C	0.980	0.935	0.807

Table 4.3. Third Dataset Adjusted R^2 values

	cycle 1~2	cycle 1~5	cycle 4~5
Maps D	0.507	0.499	0.790
Maps C	0.887	0.806	0.931

Section 4.3.2. High Strain Regions in Detwinned State Associated with the Accumulation of Residual Strain

There was a weak correlation between locations of high strain in the detwinned martensite (which has also sustained plastic deformation) upon loading (map C) and locations of high residual strain in the twinned martensite (map F) upon subsequent unloading, heating and cooling of the specimen. Figure 4.4 plots the principal strain (ε_1) of the detwinned/plastically deformed martensite (map C) versus the residual strain (ε_1) of the self-accommodated twinned martensite (map F) for each of the nominally one million data points in the field of view. Recall that these strains are referenced to the as-received, uncycled twinned martensite (map A, 1st cycle).

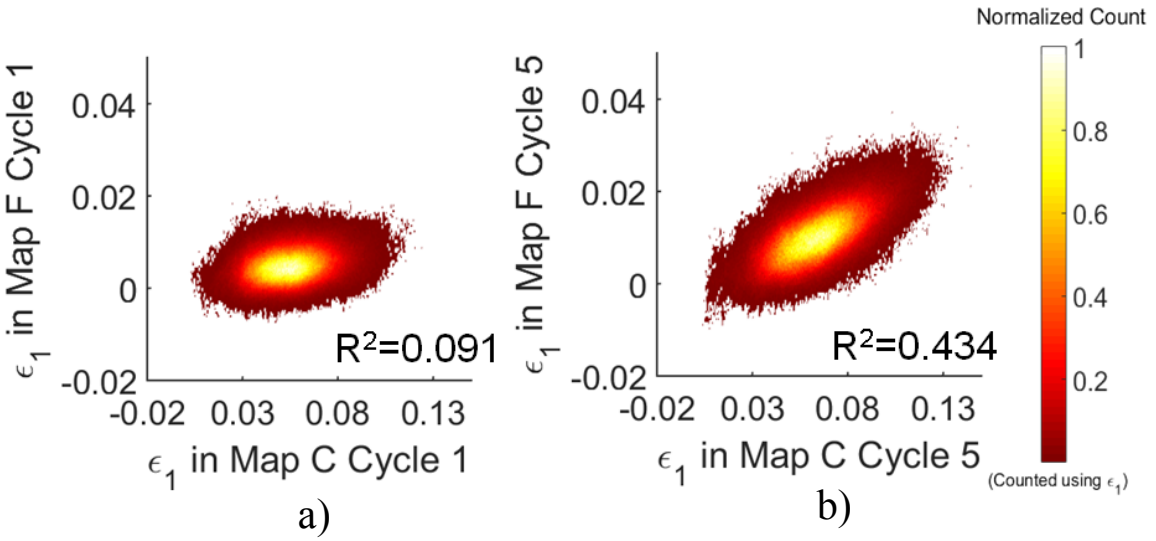

Figure 4.4: There is little linear relationship between the maximum detwinned (map D), maximum load strain map C with and the self-accommodated twinned martensite strain map F. The linear relationship however increased through cycling. Strain in map C (maximum detwinned, without unload) in Table 4.2 during cycles 1 and 5 are plotted on the x-axes against the strains at detwinned state in maps F in the same cycle respectively. The color scheme represents the normalized count of the numbers of strain data points that fall into one of the 200 by 200 data bins divided along x and y axes. The normalization was calculated using the maximum number of strain data points among all the bins in each subfigure.

During cycle 1 in Figure 4.4a, there was only a very slight linearity (R^2=0.091) in that the points that sustained a large degree of strain under mechanical loading (map C) tended to exhibit larger residual strains (map F). This trend became stronger from cycle 1 to cycle 5, going from a R^2 of 0.091 to 0.434. The strengthening of the pointwise linearity indicates that with cycling, a high strain at a point in the detwinned martensite more likely led to a high residual strain at that point in the cooled twinned martensite. The areas in the macroscopically detwinned martensite that exhibited a large degree of microscale strain – whether due to plasticity or high activity of detwinning – were less likely to regain this deformation. One cannot decouple from this data how much of this microscale strain is due to pockets of trapped detwinned martensite versus permanent plastic deformation. As seen in Figure 4.4a, there are data points (each data point encompassing a number of grains on the order of ~5-10) that exhibited large detwinning/plastic strains as much as 0.12, yet only sustained a residual strain in the cooled, twinned martensite of nominally 0.01. Meanwhile, there were a number of data points that sustained a detwinning/plastic strain on the order of 0.03, and subsequently showed minimal recovery leaving behind 0.02 residual strain. Residual strain increased overall with cycling. Higher detwinning/plastic strain at points correlated with larger residual strain increases at those points, as shown in Figure 4.4b during cycle 5. In future work on fine-grained specimens, exploring this discrepancy between the recovery behavior of clusters of grains as a function of their microstructural neighborhood and degree of sustained plastic deformation, potentially by the liftout and examination of TEM specimens at select locations, is of interest.

Section 4.3.3. Higher Strains in the Detwinned State Are Weakly Correlated with a Subsequent Faster Accumulation of Residual Strain

Regions that accommodated high amounts of strain in the detwinned state early in the cycling process were more likely to accommodate high amounts of strain in subsequent cycles, and slightly more likely to more rapidly accumulate residual strain in subsequent cycles as well. In the three-axis scatter plot in Figure 4.5a, for every pixel, the value of strain in cycle 1 map D (unloaded, detwinned martensite) is plotted on the x axis, versus the value of strain at that pixel of the difference between (cycle 2 map F) – (cycle 1 map F) on the z axis. The value for map D in cycle 2 is on the y-axis. Recall that map F is the strain map of the cooled specimen that has reverted back to twinned martensite; thus the figure represents the residual strain that was accumulated between cycle 1 and cycle 2. A similar plotting convention is used for the scatter plot in Figure 4.5b, this time examining the relationship between cycle 1 and cycle 5. In Figure 4.5a, there was not a strong correlation between higher values of strain in the mechanically unloaded, detwinned state of cycle 1 (x-axis) and a larger accumulation of residual strain at those points between cycles 1 and 2 (z-axis). However, this relationship is amplified when we look at x-z plot in Figure 4.5b, showing a slight increase in the linearity with a R^2 value of 0.145 between the value of strain at a point in map 1D and the subsequent residual strain accumulation at that point by cycle 5. The linearity also increased when considering the value of strain at a point in the subsequent map with the strain at that point in the detwinned state of the subsequent cycle, for example cycle 2 (vs. cycle 1) in Figure 4.4a with a R^2 value of 0.063. This indicated that the strain in the detwinned state increases as a predictor of residual strain as cycling progresses, and that the strain in the first cycle can, to an extent, predict the accumulation of residual strain after further (i.e. N=5) cycling.

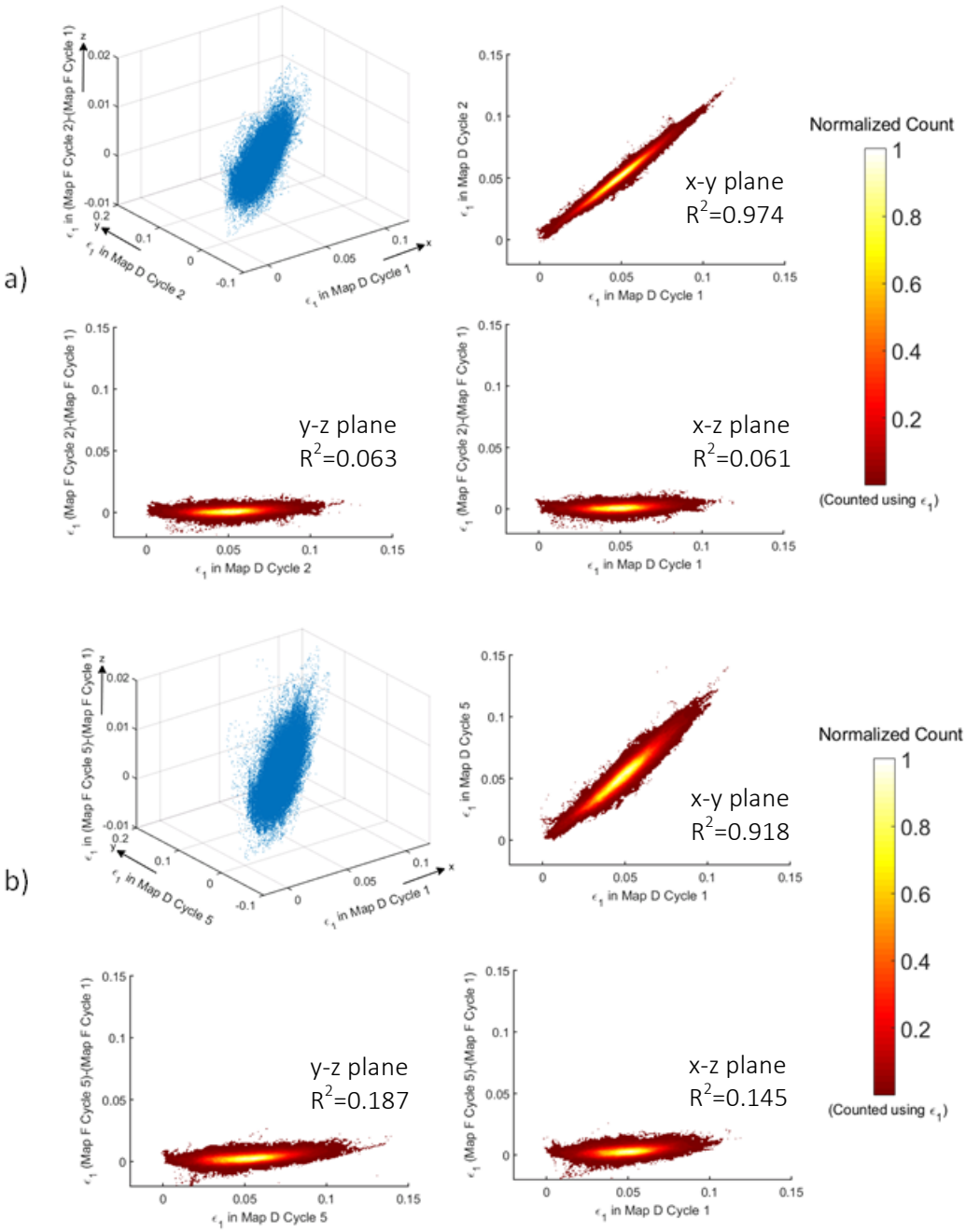

Figure 4.5: a) for every pixel, the value of strain in cycle 1 map D (unloaded, detwinned martensite) is plotted on the x axis, versus map D in cycle 2 on y-axis, and the value of strain at that pixel of the difference between cycle 2 map F – cycle 1 map F on the z axis. The heat maps are the cross-sections of the 3-D scattered plot following the same convention in Figure 4.3 and 4.4. b)) for every pixel, the value of strain in cycle 1 map D (unloaded, detwinned martensite) is plotted on the x axis, versus map D in cycle 5 on y-axis, and the value of strain at that pixel of the difference between cycle 5 map F – cycle 1 map F on the z axis.

As cycling progresses, the strain maps of the detwinned state (point C in Figure 4.2) converged to stronger (averaged) similarity. Figure 4.6 shows the summary of point-by-point correlations between strain maps at different cycles. The x-axis indicates the cycle numbers that were compared to generate the full-field correlation mapping. The y-axis is the correlation coefficient, where 1 represents a perfect correlation between the strain at those two data points, and 0 represents no correlation. The black box represents the 5 to 95 percentile of the all data points in a correlation coefficient map, and the red box represents the 25 to 75 percentile. The

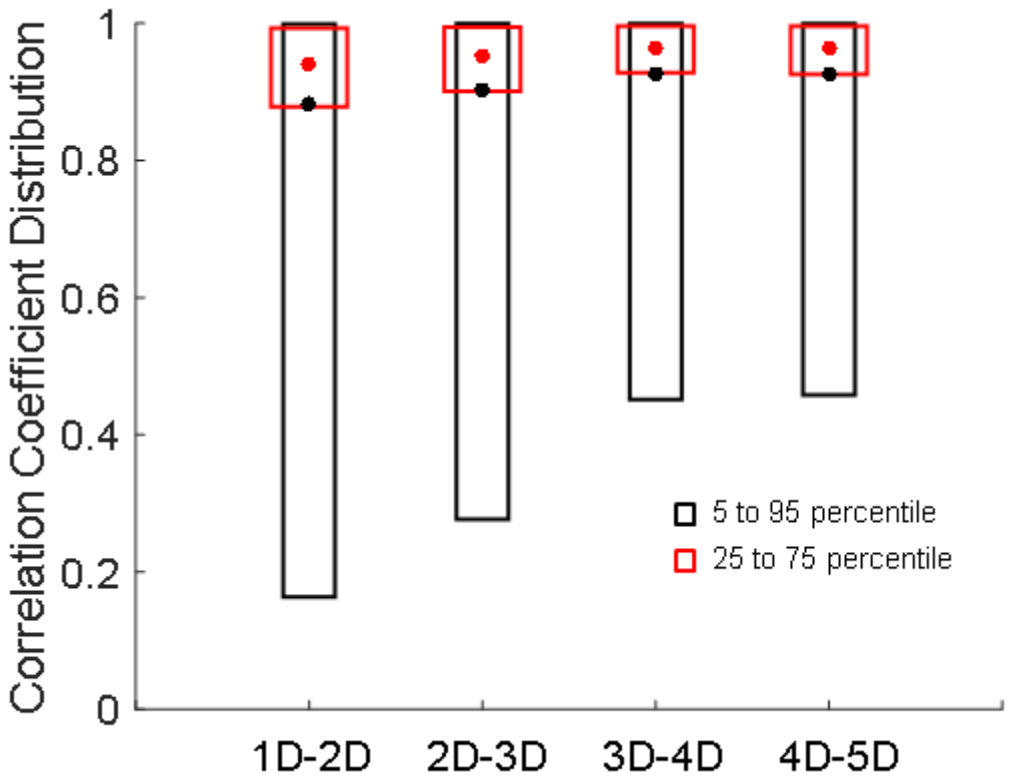

Figure 4.6: Point-by-point correlation between strain maps show that the point-by-point similarity grows with cycling. The red boxes represent the 25 to 75 percentile of the correlation coefficient distribution, whereas the black boxes represent the 5 to 95 percentile of the distribution. The lower bounds of the distribution to shift towards higher correlation values, indicating as cycling goes on, areas with poor correlation grows in transformation similarity.

red and black dots are the arithmetic mean of the data in the boxes of the dots' respective colors. Both the 5 and 25 percentile limits of the figure increased with cycling. The mean values in both percentile segments also increased with cycling, while the 75 and 95 percentile values stayed largely the same.

A point that accommodated a high level of strain in the detwinned state (point D in Figure 4.2) tended to have a stronger correlation between the strain at that point and at the same point in the subsequent cycle. This is shown in Figure 4.7, where the correlation coefficients for points accommodating various strain levels are tabulated between adjacent cycles. In Figure 4.7, each strain value in mechanically unloaded, detwinned martensite (map D in Figure 4.2) is plotted on the x-axis for map D_i, versus the correlation coefficients in the strain at that point between map D_i and D_{i+1} on the y-axis, where *i* indexes the cycle number. The x-axis is composed of 200 bins in the range x= [-0.02, 0.14], and approximately a million data points were

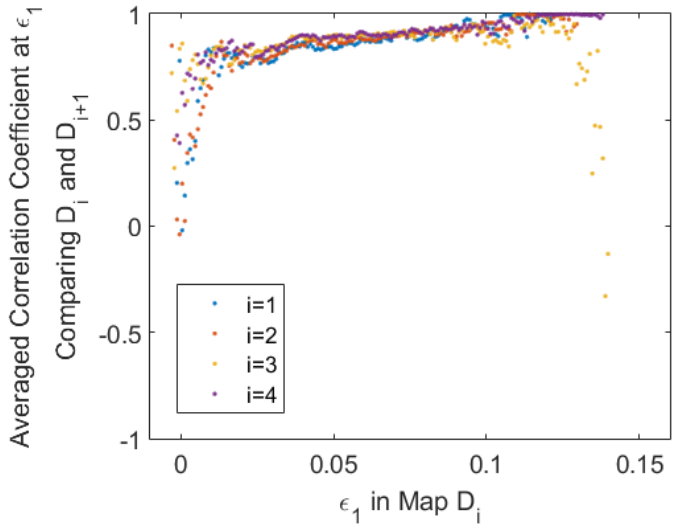

Figure 4.7: The point-by-point correlation coefficient calculated using maximum detwinned strain maps between adjacent cycles (y-axis) is plotted against the detwinned (but mechanically unloaded) strain map of the earlier cycle in the two cycles being compared. The curves roughly show positive slope indicating locations with larger deformation leads to more transformation similarity.

plotted, i.e. there were, on average, 5000 data points in each bin. In each bin, the correlation coefficient between D_i and D_{i+1} for data points with similar strain values in map D_1 were averaged for these points, and then plotted on the y-axis. In the intermediate strain range, where the majority of the data points resided (versus the extrema of the x-axis range), there is a linear trend upwards with high strains in map D_i for all cycles i=[1,5].

In the detwinned state, points with larger strains tended to exhibit a greater (averaged) strain similarity with itself in the next cycle. In Figure 4.7, points with a strain of ~0.05 at D_1 (i.e. map D, cycle 1) had an averaged correlation coefficient of approximately 0.83 with cycle 2, whereas points with a strain of ~0.08 at D_1 had a higher averaged correlation coefficient of approximately 0.89 with cycle 2. This indicates that more detwinning (and possible plasticity - note, however, there was not significant plasticity present in the unloading maps of these specimens) at a point positively influences the correlation coefficient of that point with the next cycle. In Figure 4.7, under $\varepsilon_1 < 0.1$, cycling does not affect this relationship between the averaged strain exhibited by a cluster of points and their averaged correlation with the next cycle. For example, points with strain of ~0.05 in D_1 will exhibit the same averaged correlation with D_2, as would points with strain of ~0.05 in D_4 exhibit with D_5. Fluctuations in the point-wise correlation coefficients appear at higher strains (~>0.10 in Figure 4.7) in the detwinned states, which are accruing significant amounts of plasticity.

The impact of residual strain is examined in Figure 4.8, which plots the residual strain in the recovered austenite versus the correlation between the two detwinned states straddling the austenite state. In contrast with Figure 4.7, in Figure 4.8 the correlation between E_i (austenite) and D_i and D_{i+1} does increase with cycling. For example, points that exhibit an (averaged) strain of 0.01 in the austenite state in cycle 1, show a weaker correlation between the detwinned martensite states of cycles 1 and 2 than the points exhibiting that same averaged strain of 0.01 in the austenite of the 4th cycle, which show a significantly stronger correlation between the detwinned martensite states of cycles 4 and 5. Otherwise stated, the impact of the residual strain (plasticity and retained transformation) on similarity with the next cycle between the detwinned martensite states will increase with cycling, whereas the points in the detwinned state will show a consistent correlation that is only dependent on the strain at those averaged points.

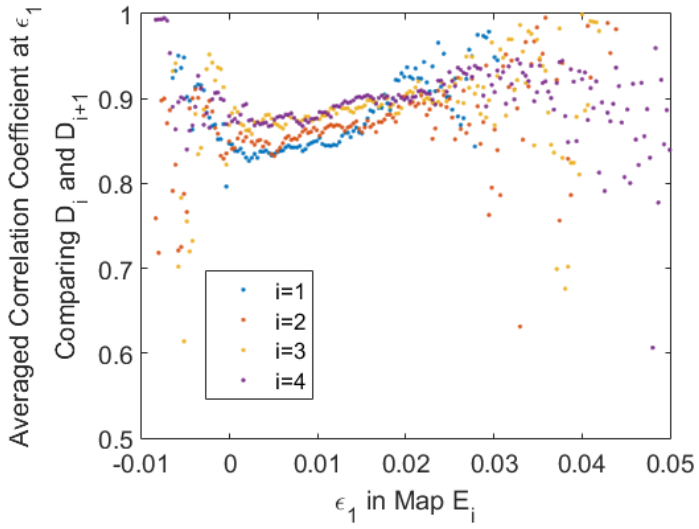

Figure 4.8: The point-by-point correlation coefficient calculated using maximum detwinned strain maps between adjacent cycles (y-axis) is plotted against the residual (heated austenite) strain map of the earlier cycle in the two cycles being compared. The data points roughly show positive slope indicating locations with larger deformation leads to more transformation similarity.

Section 4.4. Conclusions

- A pronounced heterogeneity in the strain distribution is evident at the microscale, caused by detwinning of the martensite phase upon the application of load, as shown in Chapter 3. In this chapter, it is shown that this strain heterogeneity persists throughout cycling with a large degree of similarity.

- There is a linear relationship with cycling between the strains accommodated in the detwinned state. That is, there exists a strong linear correlation between the point-by-point strains at the maximum detwinned (maps C for maximum load state and maps D for mechanically unloaded state) of actuation cycle 1 and subsequent cycles. Otherwise stated, there is a high probability that the strain demonstrated at a material point in the (overall) detwinned state will correspond strongly to the relative level of strain of the same point in the subsequent cycles.

- Regions that accommodated high amounts of strain in the detwinned state early in the cycling process were more likely to accommodate high amounts of strain in subsequent cycles, and slightly more likely to more rapidly accumulate residual strain at those points in subsequent cycles as well. This indicated that the strain in the detwinned state increased as a predictor of residual strain as cycling progressed, and that the strain in the first cycle can, to a small extent, predict the extent of residual strain accumulation after further cycling.

- As cycling progresses, the point-by-point strains accommodated by the detwinned state converged to stronger (averaged) similarity.

Chapter 5. Microscale Repeatability in Coarse-Grained Shape Memory NiTi

In order to characterize the effect of microstructure on the microscale transformation properties and the cyclic actuation behavior of polycrystalline NiTi microwires, test specimens were heat treated to an average grain diameter of 10 μm, in order to enable microstructural characterization by electron backscatter diffraction (EBSD) and analysis of the effects of grain diameter and orientation on transformation characteristics during cyclic actuation. Experimental data addressing the interactions between microstructure and phase transformation in shape memory alloys has been limited, largely due to the difficulty in obtaining the underlying microstructure and corresponding strain distributions at relevant length scales.

Section 5.1. Materials and Experimental Method

Samples were cut from spooled NiTi wire purchased from Nitinol Devices and Components (500μm OD, SM495, black oxide finish, straight). The A_f of the as-received, fine-grained material was 84 ± 5°C, as determined by differential scanning calorimetry shown in Figure 5.1. The samples were cut into 5 ± 0.1cm sections using a low-speed diamond saw (South Bay Technologies, Model #650). Using XRD (Rigaku Rotaflex), the grain diameter of the as-received material was determined by the Scherrer equation (MDI JADE 2010) to be approximately 20-40 nm, which was too small to resolve using electron backscatter diffraction [1]. The material was therefore heat treated as follows in order to grow the grains to an average grain diameter of 10 μm following a two-step heat treatment process. The wires were heated in a

box furnace (Spiro-Therm HTE46, McEnglevan). They were first heat treated at 650°C for 15 minutes to enlarge the grain diameter, following which they were heat treated at 475°C for 12 minutes to reduce the influence of precipitation. Both heating steps were followed by a water quench. The DSC data was collected again after the heat treatment. The A_f increased to 100 ± 5°C, the R-phase peak disappeared, and the M_f temperature was roughly 48 ± 5°C. The average grain diameter of the heat treated samples was approximately 10 μm as characterized by EBSD. The grain diameter distribution is shown in Figure 5.7a.

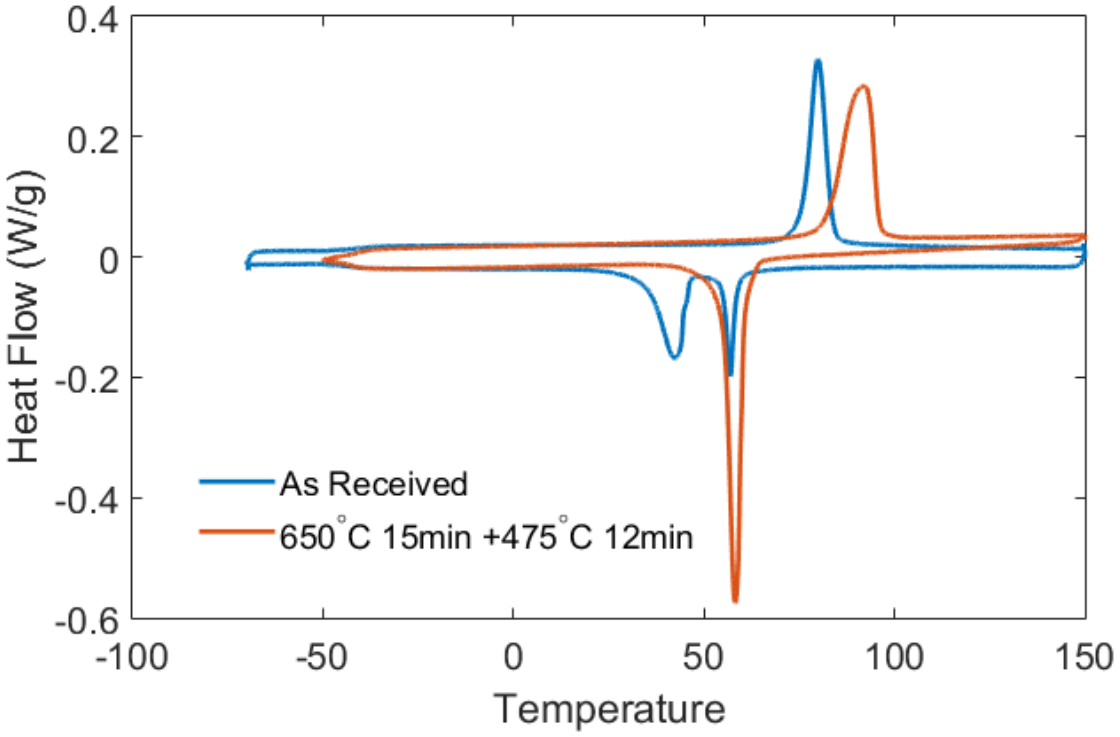

Figure 5.1: DSC graphs of the as-received microwires tested in this chapter before and after a two-step heat treatment. The A_f temperature increased from 84±5°C to 100±5°C. The R-phase peak vanished after heat treatment and M_f temperature increased to 48±5°C.

The test specimens were then mounted onto aluminum cylinders of 2.5 inches diameter and 1 inch thickness using Crystalbond (509-3 Ted Pella). Samples were gently pressed onto the aluminum block using a piece of flat glass, following which they were mechanically polished using 600 grit sand paper. The Crystalbond was then melted and the wires were turned over, such that the newly created flat surface was now in contact with the aluminum block. The wires were then mechanically polished using 1200 grit sand paper, and subsequently vibratory polished (Pace Technologies GIGA-0900) for 12 hours, skipping the diamond suspension steps described in Chapter 2.

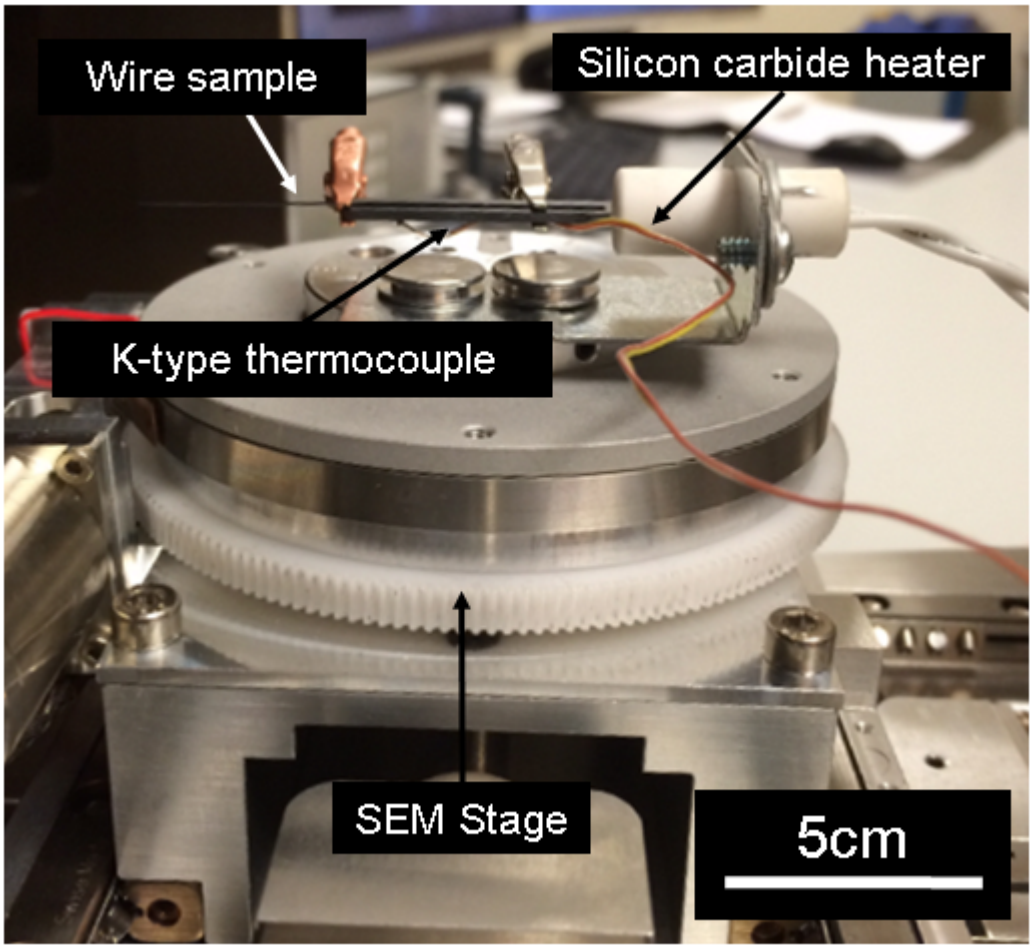

Figure 5.2: A custom SiC heater was used to heat the specimen past its A_f temperature. The heater was mounted to the SEM sample carrier stage. The heater was tilted with the SEM stage when EBSD data was collected on the sample while high temperature (150 ± 0.5°C) was applied.

EBSD maps were collected as the samples were heated in-SEM and held at a constant temperature of 150 ± 0.5°C. A custom SiC heater (designed and built by Mr. Chris Torbet, UCSB) was mounted on the carrier stage using the existing sample holder of the SEM along with two sample stubs, as shown in Figure 5.2. The wire sample was gently clamped on top of the SiC heating element. The middle section of the wire sample (the location of the field of view) was aligned with the tip of the SiC heating element. The thermocouple (K-Type, Omega) was positioned underneath the heating element, aligned to measure the temperature of the SiC strip at the location of the field of interest on the wire marked by Pt fiducial markers, i.e. measuring the temperature of the heater immediately underneath the middle point of the wire. EBSD characterization took on average 13 hours per 70 μm by 70 μm field of view. Although the PID controller for the SiC heater maintained the temperature at 150±0.5°C through time, the temperature fluctuations along with the electron beam drift still resulted in distortion in the resultant EBSD maps. To match the distorted EBSD maps to the strain maps, the EBSD maps were processed using EBSD codes such that the fiducial markers shown in the EBSD data sets matched with the strain maps spatially.

Specimens were patterned with nanoparticles following the methodology outlined in Chapter 2, then loaded at 10^{-4}/s displacement rate up to a globally applied strain of 0.06 using the in-SEM testing setup described in Chapter 2.

Section 5.2. Results and Discussion

Section 5.2.1. Strain Heterogeneity

There is strong strain heterogeneity with a persistent spatial distribution throughout all actuation cycles. Figure 5.3 shows the stress-strain-temperature relationship for cycle 1 and cycle 5. The solid lines in these plots indicate the strain values that were calculated from displacements taken from the LVDT that was built into the in-SEM stage. The dashed lines used strain values taken from averaging data points across the entire field of view in the strain maps (obtained using scanning electron microscopy and digital image correlation as detailed in Chapter 2). Both curves used loads obtained from the in-SEM testing stage to calculate the globally-applied engineering stress. At the same globally-applied load, the global (LVDT) strains are slightly larger than the DIC-obtained strains. This is reasonable, as there was likely some unavoidable grip slippage during testing of these small microwires; the magnitude of the difference correlates strain across the entire specimen, whereas the DIC-obtained strains are averaged over a localized field of view (70μm×70μm) of a heterogeneous deformation. The slip in the system corresponds to approximately 100μm displacement globally. Significant residual strain was accumulated with cycling in the coarse-grained material, and the constant stress plateau corresponding to martensite detwinning was much less evident than in the fine-grained material (Figure 3.3) during cycle 5.

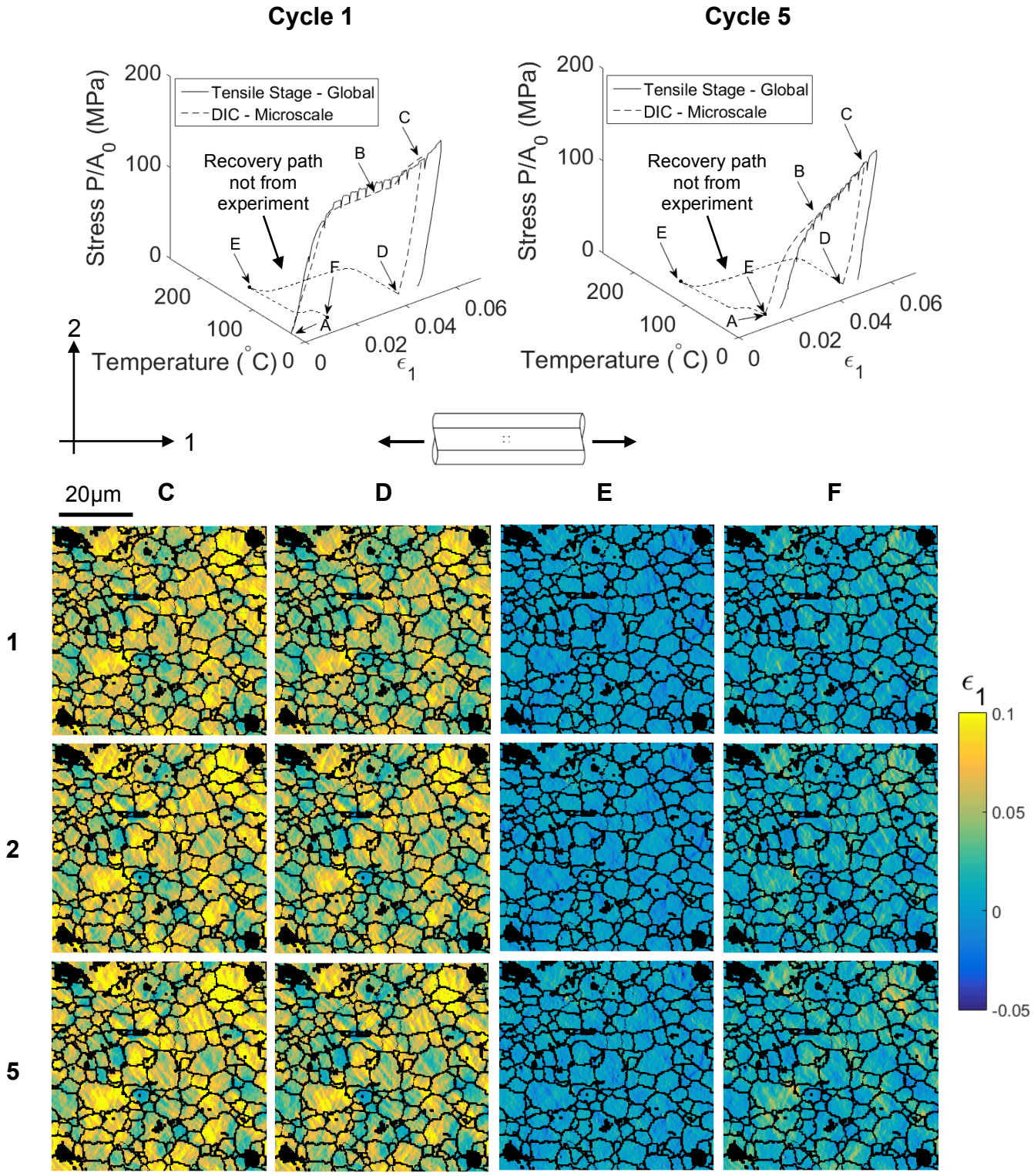

Figure 5.3: Stress-strain-temperature plots of cycles 1 and 5, as well as the full-field strain maps of at designated stress-strain-temperature states. The grain boundaries are overlaid on the strain maps. There is strong strain heterogeneity with a persistent spatial distribution throughout all actuation cycles. (Note: curve on heated strain recovery is not experimental data)

In Figure 5.3, full-field microscale strain maps are labeled A-F in order to designate the loading stages when the strain maps were captured. Note that only the strain maps for points C-F are shown in this figure, as these are the maps under discussion. Point A is before mechanical loading, when the specimen is considered fully twinned martensite; this state was also taken as the reference image prior to the start of testing (i.e., taken as the state of zero strain in the ensuing digital image correlation analysis). Point B is midway through mechanically-induced detwinning. Strain maps at point C were taken at the maximum globally applied load at room temperature ($27°C < M_f = 50 \pm 5°C$), and thus constitute largely the detwinned martensite phase. Maps D were taken when the mechanically applied load was released, therefore constituting largely detwinned martensite with recovered elastic deformation. Maps E were taken when samples were heated to above austenite finish temperature, constituting largely the recovered austenite phase. Finally, maps F were taken when sample was cooled and self-accommodated to twinned martensite. For brevity, the strain maps from cycles 1, 2 and 5 are shown in Figure 5.3. Each of the strain maps captures a 56μm×56μm area of interest, with each map containing 687,160 data points that are each 68nm×68nm in size. As evident in Figure 5.3, all of the microscale full-field strain maps at points C-F include pockets of widely varying strains, indicating different levels of transformation, throughout thermo-mechanical cycling. This is consistent with previous investigations using fine-grained samples [2].

Section 5.2.2. Effect of Grain Diameter on Strain Heterogeneity

As evident in a comparison between the as-received and heat treated specimens in Figure 5.4, the heterogeneity of the strain distribution was more significant in the heat-treated, coarse-grained samples (of average grain diameter 10μm) than in the as-received, fine-grained specimens (of average grain diameter 20-40nm, assuming shape factor of Scherrer equation K=0.9) that were observed in Chapters 3 and 4.

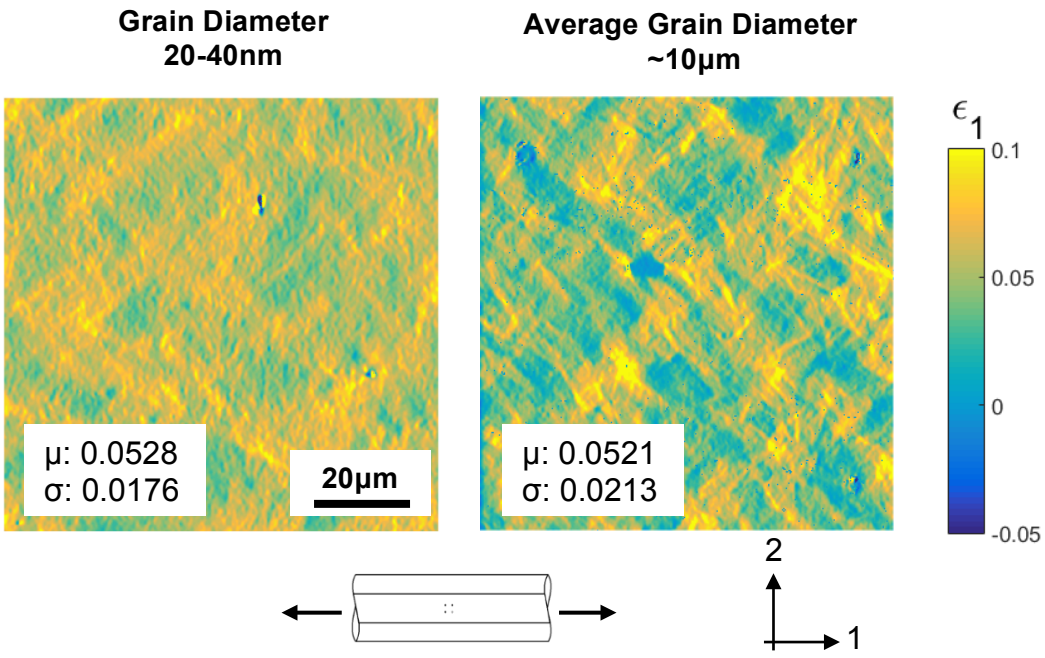

Figure 5.4: A comparison of heterogeneity in samples with different grain sizes, shown in a 70μm×70μm field of view. The mean and standard deviation of the strain distribution in the field of view are μ and σ respectively. Strain distribution in samples with larger grain sizes is more heterogeneous than the fine-grained samples.

In Figure 5.4, both fields of view are 70μm × 70μm in size, where each pixel is of 68.4nm×68.4nm in size. Parameter μ is the mean strain that is calculated from the approximately 1,000,000 data points encompassed in the field of view, and σ is the standard deviation of the data points. The mean axial strains, as determined by the average of 1,048,576 points across the 70μm×70μm fields of view, were chosen to be similar values of approximately 0.052 - 0.053 in

both fields of view in order to highlight the disparity in the degree of strain heterogeneity. Although the averaged strain across the field of view was nominally the same, the standard deviation of the strain (σ) increased by approximately 20% as the average grain diameter was increased from 40nm to 10μm. Note that the pixel size from which the heterogeneity was calculated encompassed a number of grains in the fine-grained case, whereas pixels in the coarse-grained case were sub-grain.

In the Figure 5.6, the two fields of view (fine-grained and coarse-grained) shown in Figure 5.4 were examined. Thirty square fields of view were taken at randomly distributed locations in each of the two strain maps, and their dimensions (as defined by the horizontal field width) were varied from 0.7μm (encompassing 100 data points of strain) to 47.88μm (encompassing 122,500 data points of strain) in 340 separate HFW steps. As the field of view was decreased in the fine-grained specimen, there was an apparent decrease in the standard deviation of the strain for all thirty fields of view, starting at nominally 20μm HFW. Even the smallest 0.7μm HFW FOV in the fine-grained material encompassed hundreds of grains. In the case of the coarse-grained material, however, there was not a uniform decrease in all thirty fields of view as the HFW decreased. Because a 20μm HFW encompassed only nominally four grains in the coarse-grained field of view (assuming a 10μm grain diameter), the small number of grains in the field of view coupled with the larger sub-grain strain heterogeneity overall, was likely the cause of substantial variation.

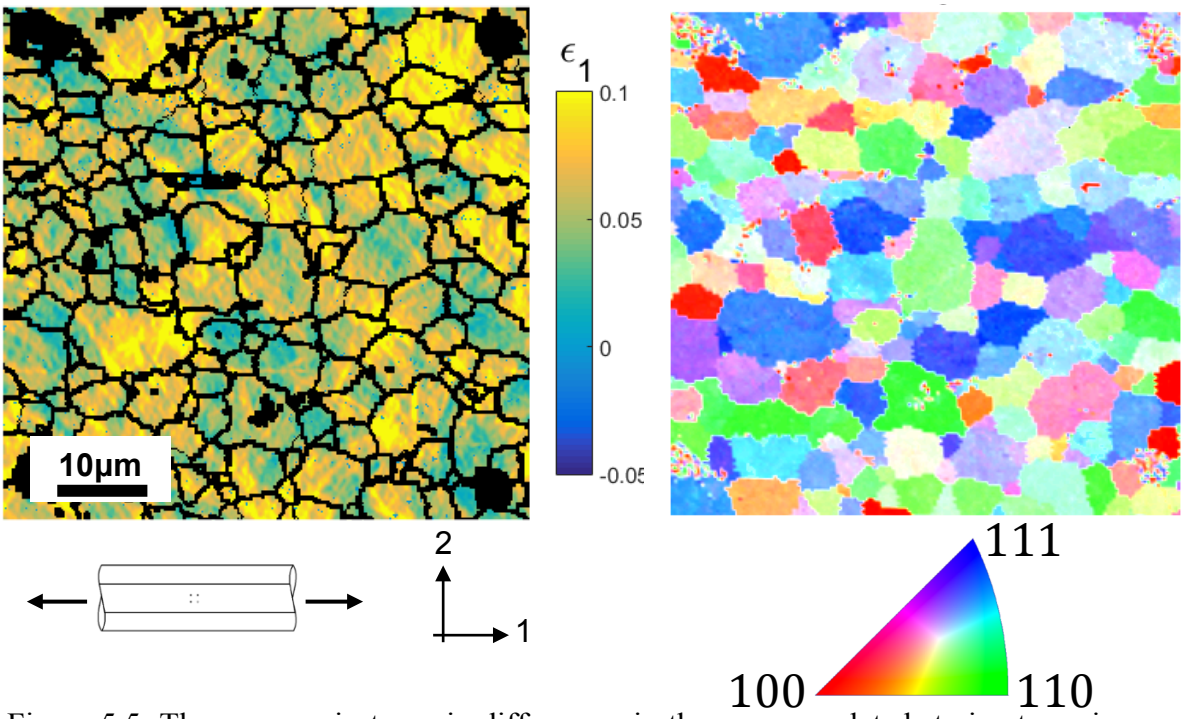

Figure 5.5: There are grain-to-grain differences in the accommodated strain at maximum deformation (detwinned martensite state). Grains were quite heterogeneous in their accommodation of strain, with some grains experiencing little detwinning while others accommodated strains >0.1. The underlying microstructure of the field of interest is shown on the right hand side.

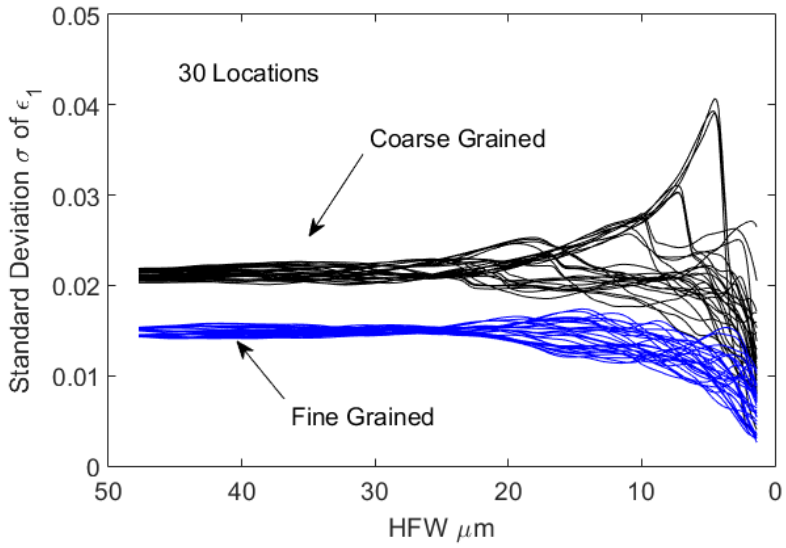

Figure 5.6: Effect of grain size and HFW on the strain heterogeneity of the as-received and heat-treated NiTi shown in Figure 5.4, where the strain heterogeneity decreases in the fine-grained material as the ratio between the length scale of the microstructure and field of view increases. Data from Figure 5.4 is illustrated here, but this trend holds across other tests. In each strain map, 30 locations are taken, and the standard deviation in 340 FOVS with different HFW ranging between 0.7 μm to 47.88 μm were calculated at each location.

Certain grains in the coarse-grained material showed a high degree of sub-grain strain heterogeneity, but there was no clear dependence of the degree of this heterogeneity with grain diameter. As evident in Figure 5.6, which shows the strain map of the largely detwinned state (under maximum mechanical load) with overlaid grain boundaries, there existed numerous grains where only a localized portion of these grains underwent significant deformation. Figure 5.7 plots the standard deviation of the strain inside a single grain on the y-axis, and the size of that grain in μm on the x-axis. Separate tests were conducted on three different specimens (tests denoted as red, blue, and green in Figure 5.7), and the finding of no dependence on grain diameter was consistent. One can argue that there may be a slight narrowing of the observed standard deviations of the strain inside of a grain as the grain increases in size, but more tests would be needed to determine this conclusively, particularly as the number of grains drops off significantly after a grain diameter of nominally 7μm, as shown in Figure 5.7 b. In Figure 5.7 a, the grain diameter distribution is shown in a stacked histogram, where color represents the data set shown in Figure 5.7 b c.

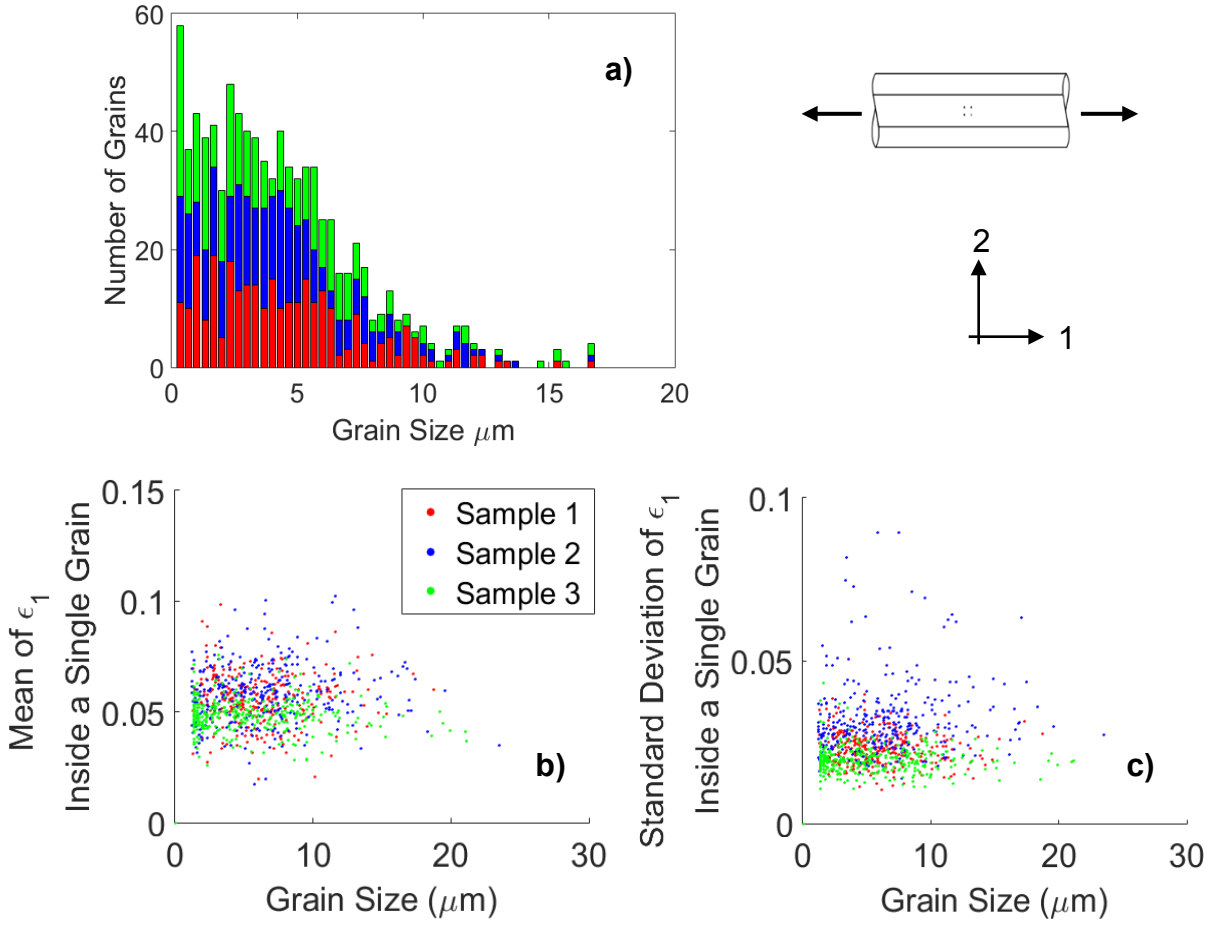

Figure 5.7: Size of the grains has little correlation with the extent of transformation or the spread of strain distribution within grains. a) Grain size distribution summarizing 3 tests; b) Mean strain inside individual grains vs. grain size; c) Standard deviation inside individual grains vs. grain size.

Section 5.2.3. Effect of Grain Orientation on Sub-Grain Strain Heterogeneity

The degree of sub-grain heterogeneity (in the macroscopically detwinned state, i.e. map C in Figure 5.3) did not depend on the grain orientation (characterized in the austenite phase). To examine sub-grain strain distributions in each grain, all strain values in an individual grain were extracted and ranked by percentile inside the grain. An average grain in this field of view of diameter 5 μm encompassed 5000 data points. The strain values at 5, 25, 75, and the 95 percentiles of strain in each grain are plotted in Figure 5.8. The wider section of a bar in the figure represent the 25 to 75 percentile bounds, and the thinner lines represent the 5 to 95 percentile of all strain values inside a grain. The bars are colored according to the color scheme of the stereographic projection triangle for a BCC cubic structure. The scatter plot inside the stereographic triangle represents the grain orientation distribution (crystallographic texture) of the field of view. There is no clear trend regarding the extent of transformation with respect to the grain orientation.

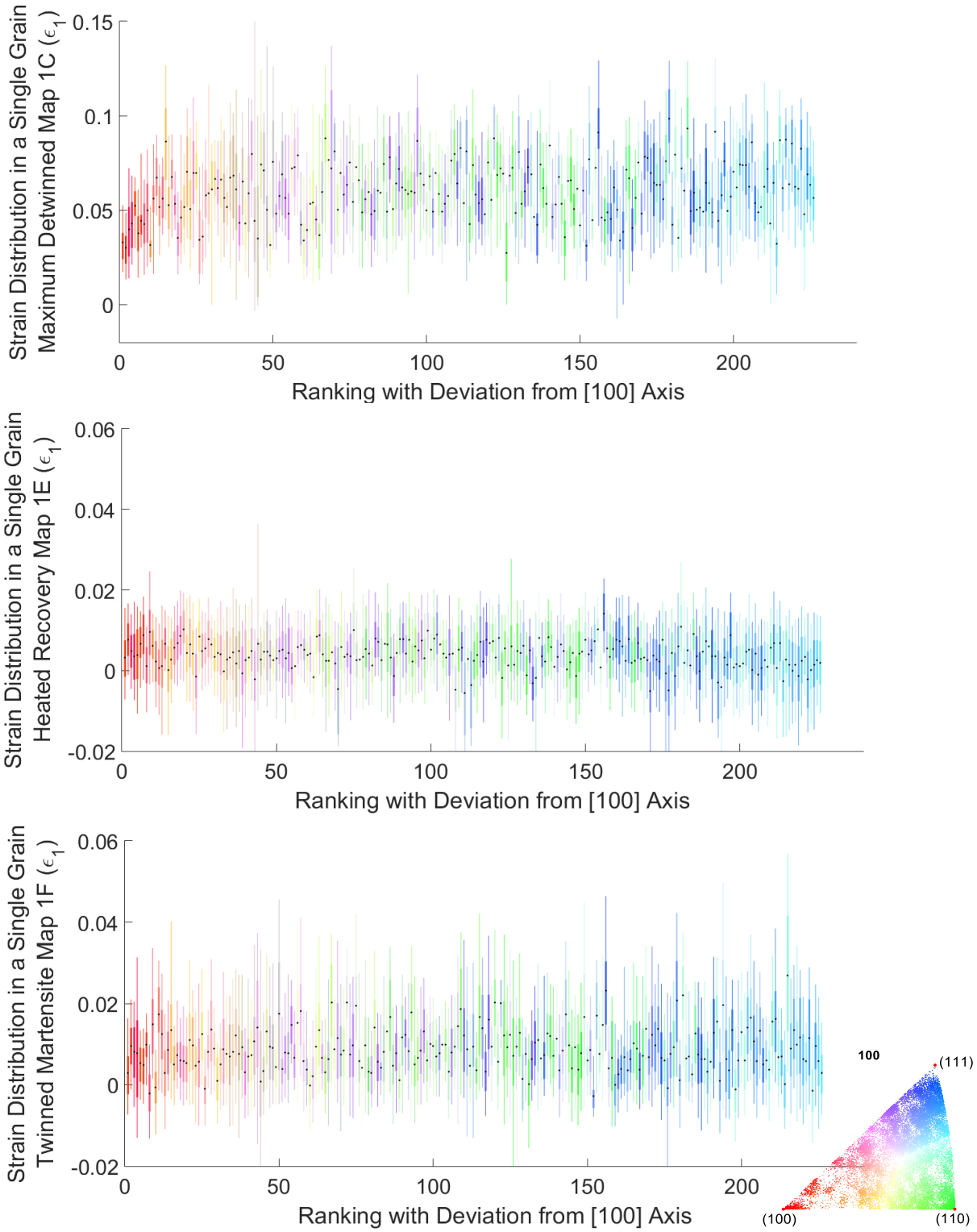

Figure 5.8: There is no significant correlation between the grain orientation and the strain distribution in individual grains during detwinning, recovery and self-accommodation. In these plots, the wide sections of these bars plots are 25 to 75 percentile range of all strain values in a grain. The thinner sections are the 5 to 95 percentile of the strain values. Black dots are mean values.

In general, grains encompassing high strains (indicating high detwinning activity) exhibited more residual strain in the twinned martensite. Similarly, the converse was true. To further investigate this, grains were sorted into two groups, which were labeled as 'high performing' grains (grains that encompassed large strains at detwinned states and also exhibited good recovery) and 'low performing' grains (grains that did not have significant strains upon detwinning, i.e. their grain-averaged strain was below the mean strain at maximum load (Map C), and that also exhibited residual strains that were above the mean residual strain). Here, large strains at detwinned states in a grain were taken to be those occurred when the grain-averaged strain was larger than the averaged strains at detwinned state in map C, and good recovery was taken to be when the grain-averaged residual strain was below the mean in the specimen heated >150°C, i.e. above A_f. As illustrated in Figure 5.9, the open circles mark the high performing grains, where both transformation and strain recovery was significant upon loading and heating. The triangles mark the low performing grains, with below average detwinning when loaded and above average retention of residual strain when heated. The distribution of strains in these grains are tabulated in Figure 5.10 a and b. The detwinned, austenite, and twinned plots are averages of all strain data points in Figure 5.3, maps C, E, and F respectively. By comparing Figures 5.10 a and b (note the difference in scale bars), the characteristic differences between the two groups can be summarized as follows: the strains at detwinned states of the low performing grains stayed nominally constant during mechanical deformation, whereas for the high performing grains, the strains in the detwinned state increased from 0.074 to 0.086 during the first five actuation cycles (note that this may likely include plastic deformation). Strains in the austenite phase for both groups remained largely the same and constant with cycling.

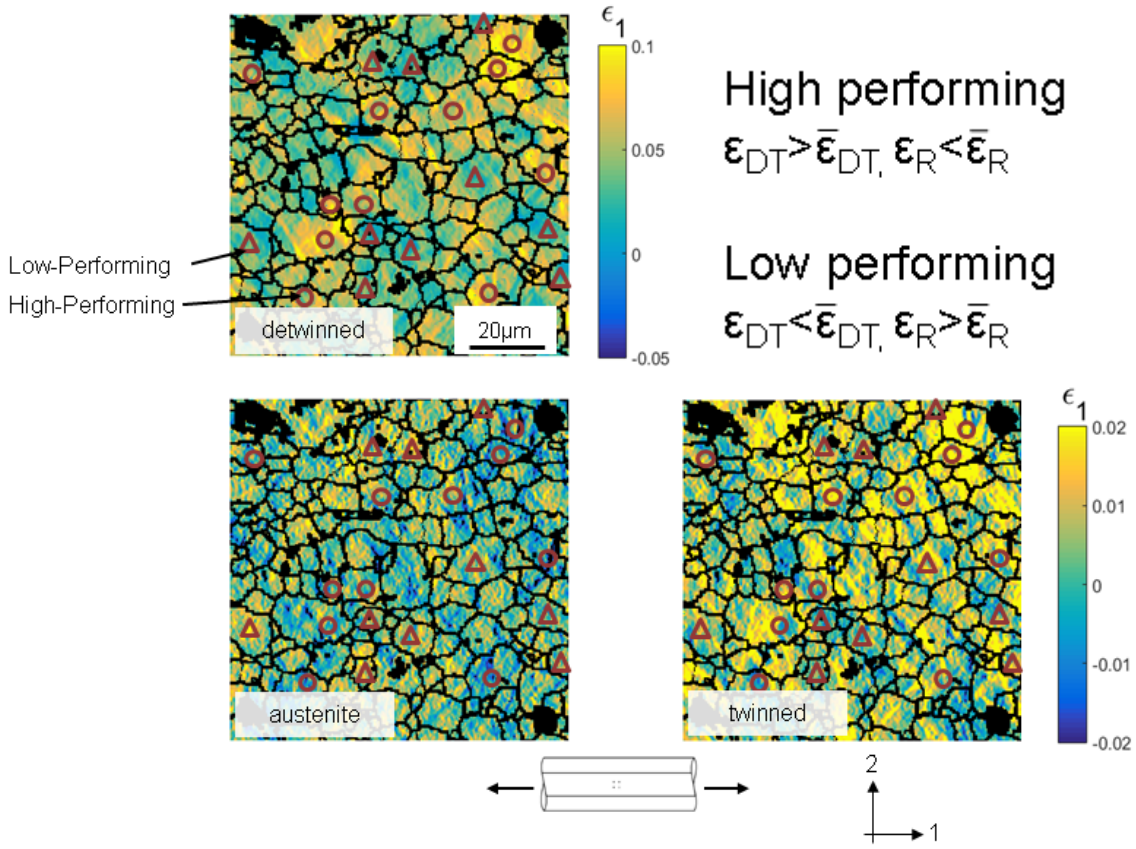

Figure 5.9: The pattern of strain heterogeneity changed within an actuation cycle in the coarse-grained material. For example, the grain in the upper right corner of the strains at the detwinned state map exhibits significant deformation. However, this grain did not retain significant residual strain upon reversion to the austenite phase. During cooling (self-accommodation through twinning), the grain experienced a greater strain increase than its neighbors. A grouping criterion is proposed: grains that experienced significant ($\varepsilon_{DT}>\bar{\varepsilon}_{DT}$) strains at detwinned states as well as less than average ($\varepsilon_R<\bar{\varepsilon}_R$) residual strains under the austenite state are called 'high performing grains', marked using open circles. Grains that exhibited less than $\bar{\varepsilon}_{DT}$ strains at detwinned state but exhibited larger than average ($\varepsilon_R>\bar{\varepsilon}_R$) residual strain are grouped as 'low performing grains'.

Although there is similarity in the microscale strain distribution between the detwinned martensite and the twinned martensite after heating and cooling (Figure 5.3, maps C and F, respectively), the intermediate stage of the austenite did not show the same degree of similarity. This is more evident in the strain maps using a reduced strain scale bar as shown in Figure 5.9.

For example, the grain in the uppermost top right of the field of view shows a large degree of activity in the detwinned state, then, in the austenite state appears to be significantly compressed, and then when subsequently cooled, shows a large degree of residual strain that mimics the original detwinning (recall that the reference image was taken at the twinned martensite state at room temperature). A vertical line was taken from the arrows shown at the bottom of the strain maps in Figure 5.9, where a pixel location of 0 corresponds to the bottom middle of the strain map, and a pixel location of 950 corresponds to the last pixel at the top of the strain map. These profiles are shown in Figure 5.11, where it is evident that both the magnitude and distribution of strains change at these states.

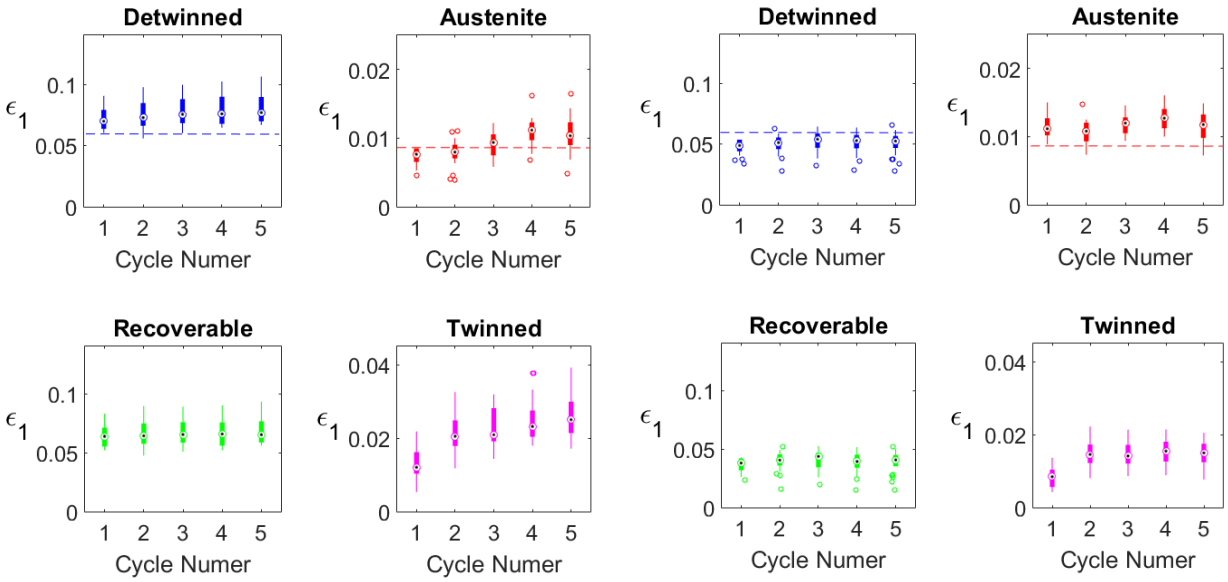

a) High performing grains b) Low performing grains

Figure 5.10: Strain progressions of 'high performing' and 'low performing' grains, as defined in the text, during cycling are shown as bar plots. The wider sections of the bars are the 25 to 75 percentile of strain values in the groups of grains. The thinner sections represent the 5 to 95 percentile of the strain distribution. Recoverable strain is calculated using the difference between the strain under detwinned and austenite state. The open circles are outliers. The data points marked in black are the mean values. Each group of grains ('high performing' and 'low performing' grains) roughly represents 160,000 data points. These bar plots showcase the difference in detwinning, recovery, and self-accommodation (twinning) activities. In the two groups, high performing grains provide more recoverable strain, without significant residual strain under austenite phase. However, the residual strain during self-accommodation is significant in the high performing grain group.

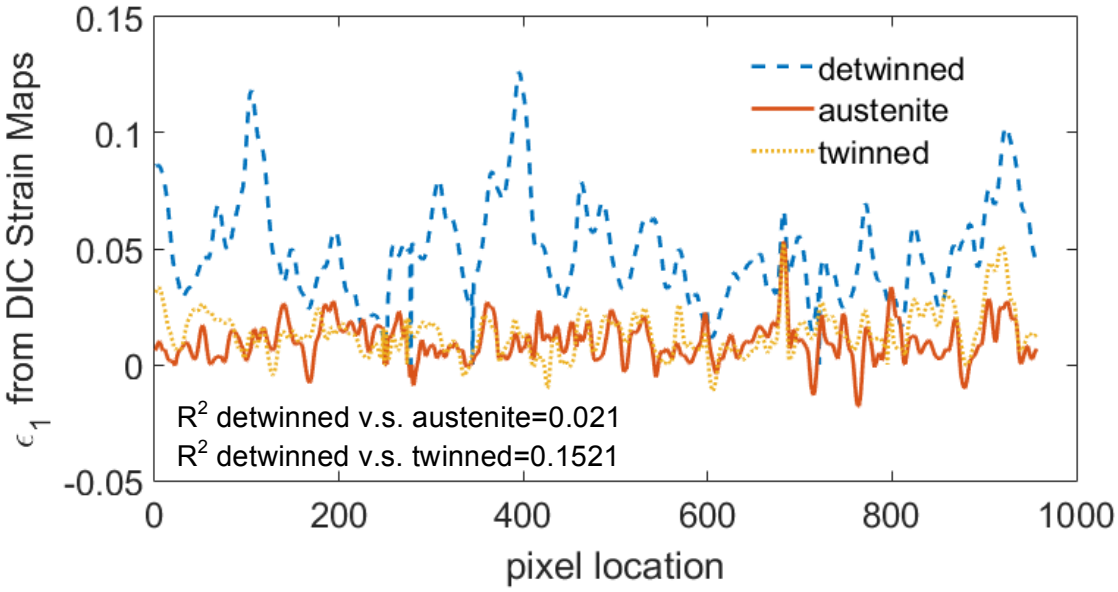

Figure 5.11: The pattern of strain distribution changes during heated strain recovery and self-accommodation. Lines in this figure demonstrate strain values along the line of pixels marked by the black arrow in Figure 5.10, under detwinned martensite, heated (austenite) and cooled (twinned martensite) states. The R^2 values between these lines show that strain pattern in detwinned martensite is much more similar to twinned martensite compared to austenite by a factor of 7. Note the R^2 values are evaluating the trend rather than the magnitude of the profile. Therefore, the pattern of strain distribution changed during heated strain recovery, and partially regained during self-accommodation.

Section 5.2.4. Transformation Similarity During Thermal-mechanical Cycles

There is linear relationship between the sub-grain strains accommodated by detwinning in the coarse-grained samples that grows with cycling, although the linearity is less significant than the fine grained samples. A comparison of the strains in the detwinned state (maps D, Figure 5.3) between adjacent cycles is tabulated in the form of heat map in Figure 5.12, where details of the heat map construction can be found in Chapter 4. The R^2 value between maps D in cycle 1 and cycle 2 is 0.655, which is significantly smaller than 0.927 in the fine-grained samples as shown in Figure 4.3.

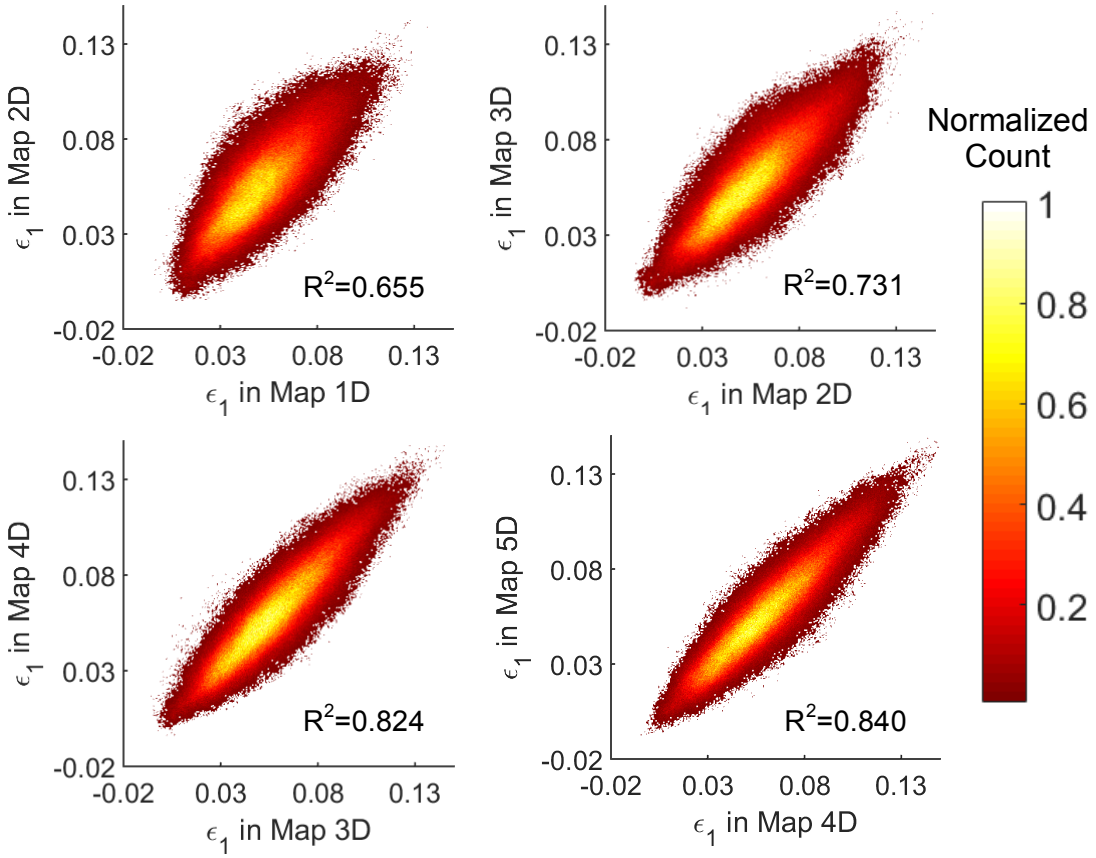

Figure 5.12: Strains at detwinned state in maps D (in Figure 5.3) are compared and tabulated in the form of heat maps following the same convention in Chapter 4. The correlation between the strains at detwinned state in coarse-grained sample is less than those in fine-grained samples. This correlation in strains at detwinned state grows with cycling, when comparing between adjacent cycles.

The correlations between strains in the globally detwinned state increase between adjacent cycles, as shown in Figure 5.12. The correlation increase is shown using the distribution of the point-by-point correlation coefficients in Figure 5.13. Each bar in the figure represents the distribution in point-by-point correlation coefficients between the strain maps indicated on the x-axis. For example, using strain maps D in cycle 1 and 2, the similarities between the strains are calculated at each pixel in the form of correlation coefficients. These point-by-point correlation coefficients were calculated using a 3 pixel×3 pixel area surrounding the pixel under consideration. The correlation coefficient values were then tabulated in the form of a bar plot. The wider sections of the bars represent the 25 to 75 percentile of the correlation coefficient

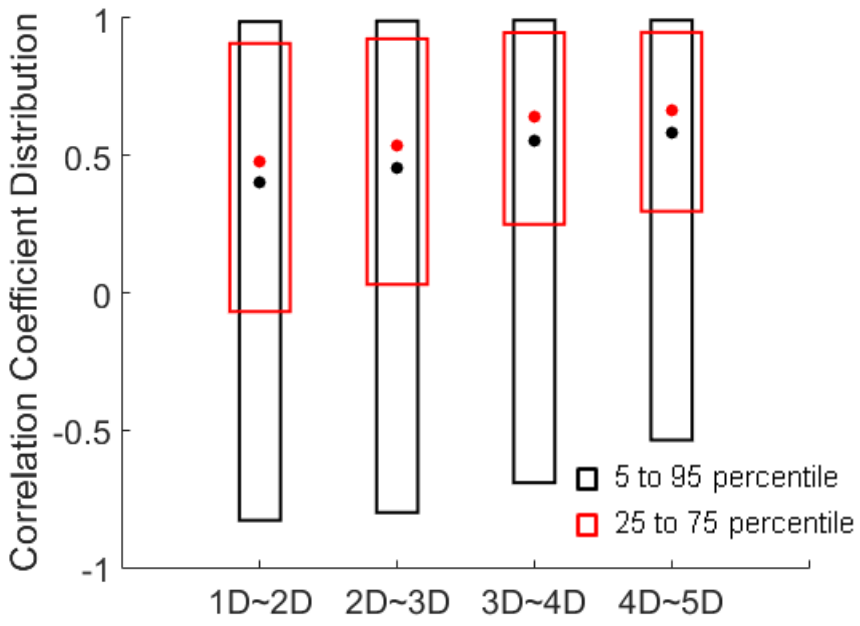

Figure 5.13: Point-by-point correlation between strain maps show that the point-by-point similarity grows with cycling. The wider sections of the bar plots represent the 25 to 75 percentile of the correlation coefficient distribution, whereas the thin lines represent the 5 to 95 percentile of the distribution. The lower bounds of the distribution to shift towards higher correlation values, indicating as cycling goes on, areas with poor correlation grow in transformation similarity.

distribution, the thinner sections represent the 5 to 95 percentile of the correlation coefficient distribution, and the black circles designate the mean of the distribution.

During strain recovery, the similarity between residual strain and the maximum globally applied strain grew with cycling in both the austenite phase and the twinned martensite phase. As shown in Figure 5.15, the R^2 value in the austenite grew from 0.090 to 0.202 from cycle 1 to 5. In the twinned martensite phase, the R^2 value grew from 0.306 to 0.591 from cycle 1 to 5.

There is little correlation between the local transformation or the residual strain and the point-by-point transformation similarity. A summary of this relationship plotted in Figure 5.16. The strain ranges on the x-axes of these both figures a and b are sectioned into 200 bins. For all the strain data points contained in each bin, the local point-by-point correlation coefficient at the same strain points are averaged at plotted against the y-axis. There is no significant relationship between the magnitudes of the strain on the x-axis with the transformation similarity on the y-axis. Instead, the data points stayed flat throughout the ranges of strain, except for larger and small strain values at the extremes.

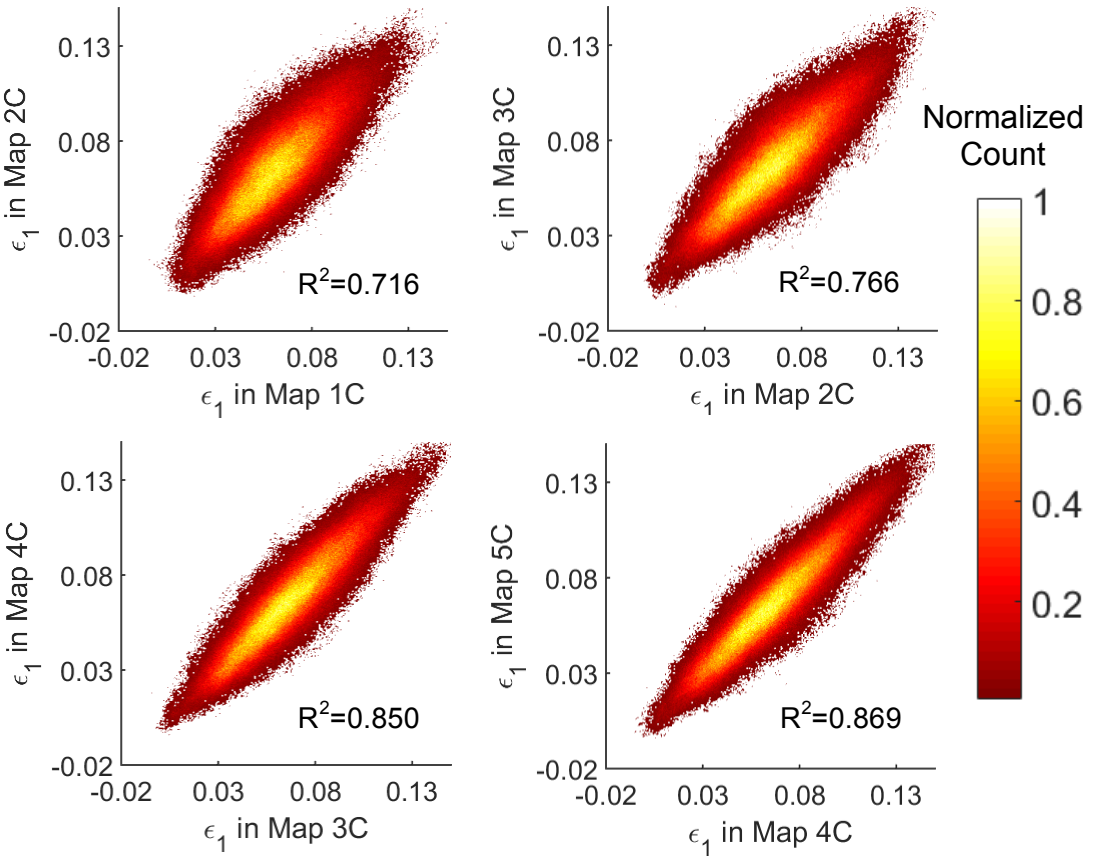

Figure 5.14: Strain maps C (in Figure 5.3, under maximum globally applied strain) are compared and tabulated in the form of heat maps following the same convention in Chapter 4. The correlation between maps C in adjacent cycles is slightly stronger than in maps D in Figure 5.12. For example, the overall correlation between maps C is 0.716 while for maps D the R^2 value is 0.655. These R^2 coefficient values are also less than the fine grained samples.

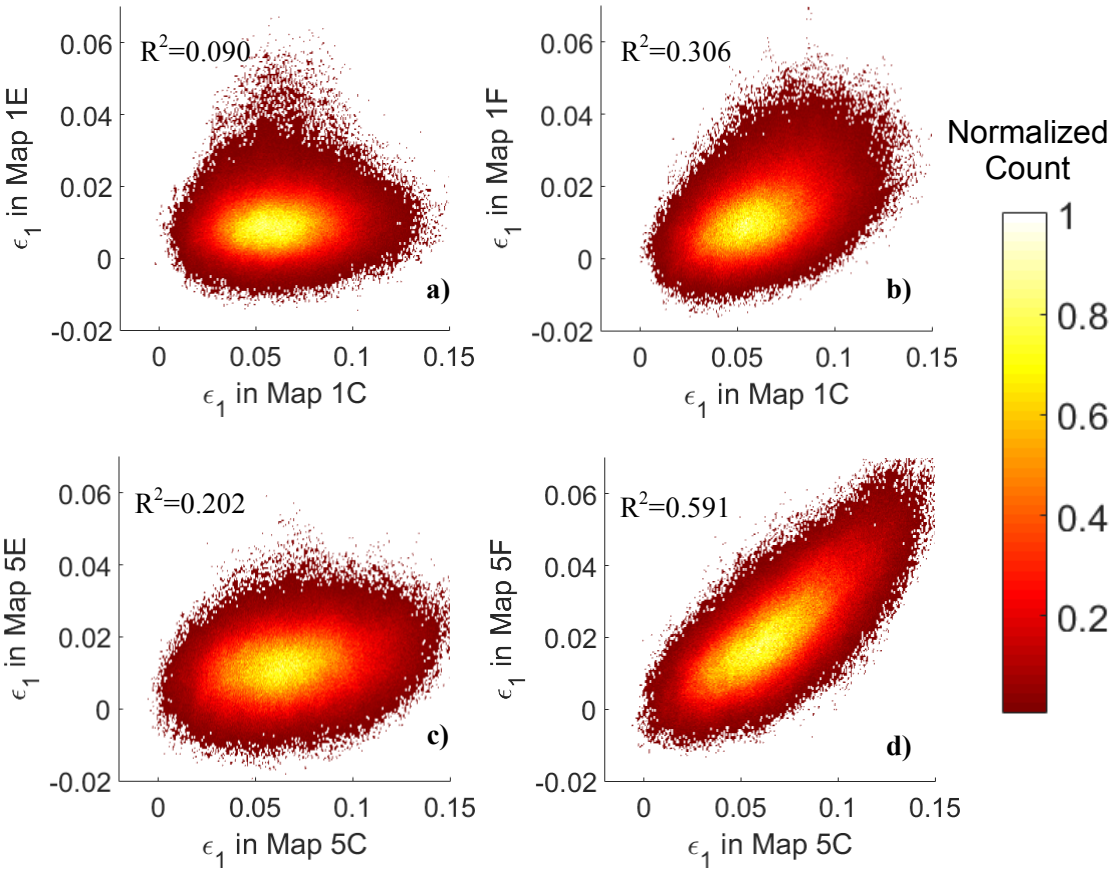

Figure 5.15: Strain distributions in the detwinned martensite (map C), austenite (map E), and subsequently cooled twinned martensite state (map 5) for cycles 1 and 5. The correlation between strains in the detwinned martensite and subsequent austenite upon heating became stronger with cycling, with a R^2 value that grew from 0.090 to 0.202 from cycle 1 to 5. The correlation between strains in the detwinned martensite and subsequently heated and cooled twinned martensite was substantially stronger, with a R^2 value that grew from 0.306 to 0.591 from cycle 1 to 5. The detwinned martensite phase was, on average, more strongly correlated with the subsequently heated and cooled twinned martensite than with the austenite.

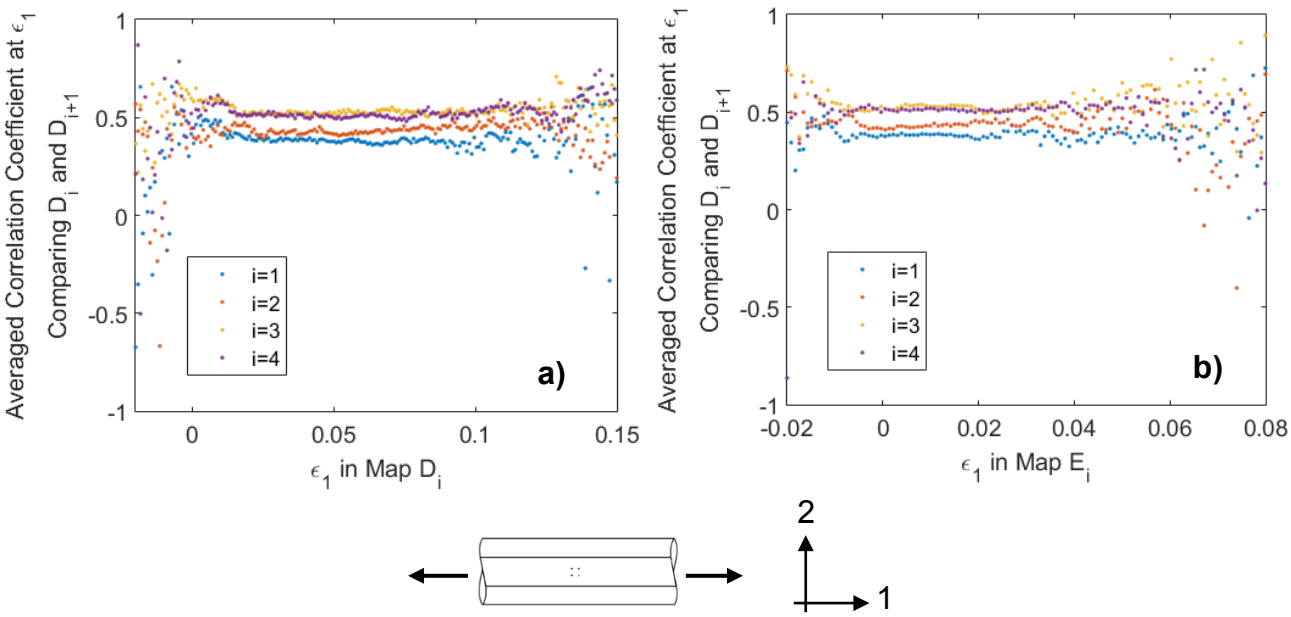

Figure 5.16: Relationships between the (a) detwinning and (b) residual strains at data points (x-axis), and the similarity between that cycle and the subsequent detwinning state (y-axis). The strain ranges on the x-axes of these both figures (a) and (b) are sectioned into 200 bins. The amount of detwinning sustained in cycle *i* at a point does not significantly increase the similarity with the detwinning activity in cycle *i+1*. This is also true for the residual strains; as shown in Figure 5.16b, the amount of residual strain at a set of (averaged) data points does not significantly increase the detwinning similarity between the two cycles at those points.

Section 5.3. Conclusions

Coarse-grained Nitinol microwire specimens were produced by heat treatment from the same as-received specimens described in Chapters 3 and 4, in order to examine the effect of the heat treatment and subsequent larger grain diameter on the cyclic actuation characteristics. It was found that:

- Similar to the as-received specimens, the sub-grain strains in the macroscopically detwinned state of the coarse-grained specimens exhibited a strong strain heterogeneity, with a persistent spatial distribution, throughout actuation cycling.
- For a loading state where the average strain across the field of view was nominally the same for the as-received and coarse-grained specimens, the standard deviation of the strain (σ) increased by approximately 20% as the average grain diameter was increased from 40nm to 10μm. Note that the pixel size from which the heterogeneity was calculated encompassed a number of grains in the fine-grained case, whereas pixels in the coarse-grained case were sub-grain.
- At larger fields of view with HFWs nominally >20 μm, the strain heterogeneity (as characterized by the standard deviation of the strain) of both the coarse-grained and fine-grained case was approximately constant with changing FOV (examined up to HFWs of nominally 50 μm). At smaller FOVs with HFW <20 μm, the standard deviation (i.e. heterogentity) of the strain decreased as the FOV decreased. This did not universally hold for the coarse-grained material, as smaller FOVs became sub-grain.
- Certain grains in the coarse-grained material showed a high degree of sub-grain strain heterogeneity, but there was no clear dependence of the degree of this heterogeneity with grain diameter or grain orientation (characterized in the austenite phase).

- In general, grains encompassing high strains (indicating high detwinning activity) exhibited more residual strain in the subsequent twinned martensite, than grains encompassing less strain in the macroscopically detwinned state.
- Although there was similarity in the microscale strain distribution between the detwinned martensite and the subsequent twinned martensite (after heating and cooling), the intermediate austenite did not show the same degree of similarity.
- There was a linear relationship between strains accommodated by detwinning in the coarse-grained samples, although the linearity was weaker than in the fine grained samples. The correlation between strains in the detwinned state increased when compared between adjacent cycles. During strain recovery, the similarity between residual strain and the maximum globally applied strain grew with cycling in both austenite phase and the twinned martensite phase.
- There was little correlation between the local transformation or the residual strain and the point-by-point transformation similarity.

References

[1] D. R. Steinmetz and S. Zaefferer, "Towards ultrahigh resolution EBSD by low accelerating voltage," *Mater. Sci. Technol.* , 2017.

[2] J. Y. Gong and S. H. Daly, "Microscale Repeatability of the Shape-Memory Effect in Fine NiTi Wires," *Shape Mem. Superelasticity*, vol. 2, no. 4, pp. 298–309, 2016.

Chapter 6. Summary and Comments on Future Work

Section 6.1. Summary

This thesis investigated the microscale transformation characteristics of NiTi shape memory alloy microwires for both fine-grained (~20-40nm grain diameter) and coarse-grained (~10μm grain diameter) samples. Using a custom experimental methodology combining digital image correlation and scanning electron microscopy, full-field maps of the strain accommodated during different stages of phase transformation were captured at the microstructural length scale. The work provides, to the best of our knowledge, the first direct observations of full-field strain distributions at the microscale of shape memory NiTi wires during thermo-mechanical cycling.

The full-field strain maps, which arose from martensitic detwinning, showed strong heterogeneity at the microscale throughout thermal-mechanical cycling for both the coarse-grained and fine-grained samples. This heterogeneous distribution of the strain in the detwinned state (with the cooled, twinned martensite state as the reference zero strain image) remained consistent throughout all actuation cycles, although the magnitudes of the strain changed. This similarity was measured by full-field correlation coefficient mapping, and was found between strain maps induced by detwinning and plasticity. Regions that accommodated high amounts of strain in the detwinned state early in the cycling process were more likely to accommodate high amounts of strain in subsequent cycles − this linear relationship between strains accommodated by detwinning from cycle to cycle was observed in both fine-grained and coarse-grained specimens, though it was weaker in the coarse-grained material. Additionally, there was an

accelerated accumulation of residual strain in subsequent cycles in the fine-grained material, indicating a link between residual strain and strains at detwinned state that is established early and can negatively impact actuator performance.

In both the fine-grained and coarse-grained samples, residual strain concentrated at locations where strain accumulation from detwinning and plasticity were significant. The persistence of the strain pattern upon unloading to the austenite state – which can be viewed as a 'ghost' pattern of the strain present in the detwinned state − indicates that the process of martensitic detwinning in a shape memory cycle, and the associated plasticity that occurs with it, is spatially correlated to the subsequent accumulation of residual strain at the microscale. Additionally, correlation coefficients between individual data points tended to increase with thermo-mechanical cycling, indicating that there is a settling in process where the similarity induced by detwinning and plasticity becomes stronger as cycling progresses. Locations with larger residual strain also transformed more similarly from cycle to cycle.

The heterogeneity of the strain distribution was stronger in the coarse-grained specimens, where for a loading state where the average strain across the field of view was nominally constant, the standard deviation of the strain (σ) increased by approximately 20% as the average grain diameter was increased from 40nm to 10μm. (Note that the pixel size from which the heterogeneity was calculated encompassing a number of grains in the fine-grained case, whereas the pixels in the coarse-grained case were sub-grain). At larger FOVs, the strain heterogeneity (as characterized by the standard deviation of the strain in the globally detwinned state) of both the coarse-grained and fine-grained specimens was approximately constant with changing FOV; however, as the FOV decreased to a HWF nominally <20 μm, the standard deviation (I.e. heterogeneity) of the strain decreased as the FOV decreased. This did not universally hold for the

coarse-grained material, as smaller FOVs became sub-grain with the larger 10 μm diameter grain size.

Certain grains in the coarse-grained material showed a high degree of sub-grain strain heterogeneity, but there was no clear dependence of the degree of this heterogeneity with grain diameter or grain orientation (characterized in the austenite phase). The observation that neither grain diameter nor grain orientation affected the transformation characteristics of the grain (at the surface) supports the hypothesis that it is rather complex interactions with the surrounding microstructure that determine local transformation characteristics.

Section 6.2. Future Work

Section 6.2.1. Statistical Analysis on Microstructural Dependency

In order to characterize the complex effects of surrounding microstructure on the transformation characteristics of grains, and thus actuation behavior, statistical analysis of the full-field strain maps correlated with the underlying microstructure are of interest to examine the dependencies of martensitic detwinning and residual strain accumulation on texture. As an example of future work, limited data is shown in Figure 6.1, plotted using thirty grains in each of the 'low performing' and 'high performing' grains groups based on the coarse-grained results of Chapter 5. To provide statistical significance to both grain-averaged and sub-grain measurements of transformation (both detwinning extent and recovery of residual strain), and its relation to the underlying microstructure, a much larger amount of data is needed and will necessitate methods for automation of image capture and stitching of the subsequently acquired images.

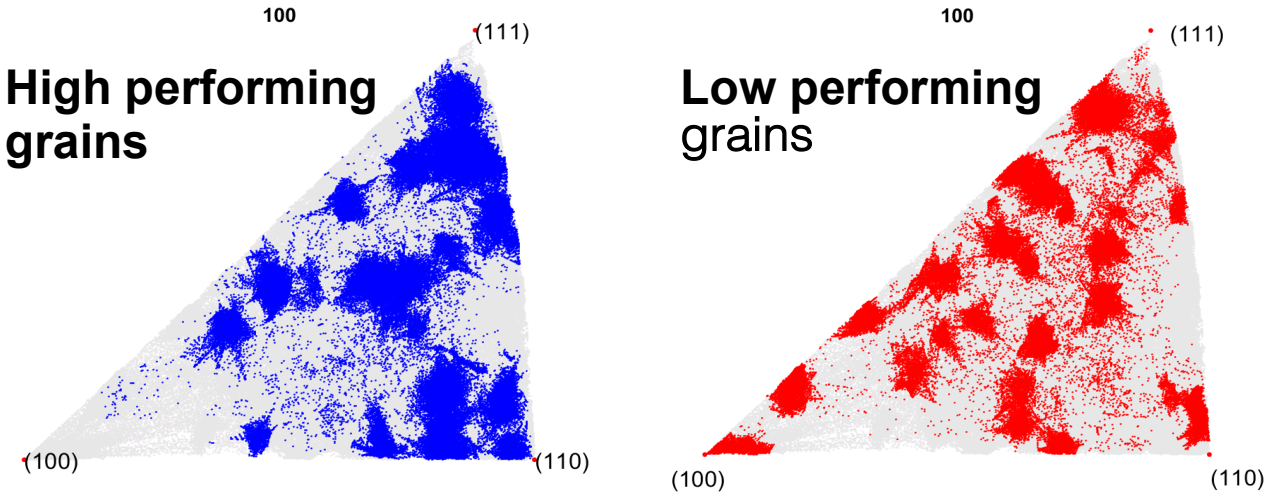

Figure 6.1: To investigate the texture dependency of the shape memory effect, large data statistical analysis and visualization methods are needed. The crystal orientations of 'high performing grains' (high detwinning, high recovery) and 'low performing grains' (low detwinning, low recovery) shown in Figure 5.10 are summarized above. These grain-averaged measures of transformation performance can be mined with regard to orientation and also with regard to the surrounding microstructure; similarly, the sub-grain transformation characteristics in these highly heterogeneous transforming grains can also be analyzed using large data statistics with regard to the surrounding microstructure. Data shown in this figure is the same set in Chapter 5.

Section 6.2.2. The Effect of Second Phase Precipitates

The effect of heat treatment on actuation capability is of interest, particularly with respect to the development of precipitates. A sharp gradient in the strain behavior of a second phase precipitate and the NiTi matrix is shown in Figure 6.2(c). An inclusion was examined using backscattered electrons to differentiate the boundaries and then EDS, where it was determined to be Ti_2Ni, as shown in Figure 6.2(a), (b). There is potential for the composition and spatial distribution of individual precipitates to be related to the microscale distribution of residual strain and strains at detwinned state during cyclic actuation, and to the larger macroscale actuation performance. This could lead to an improved understanding of the effects of heat treatment on precipitation and the resulting multi-scale phase transformation performance.

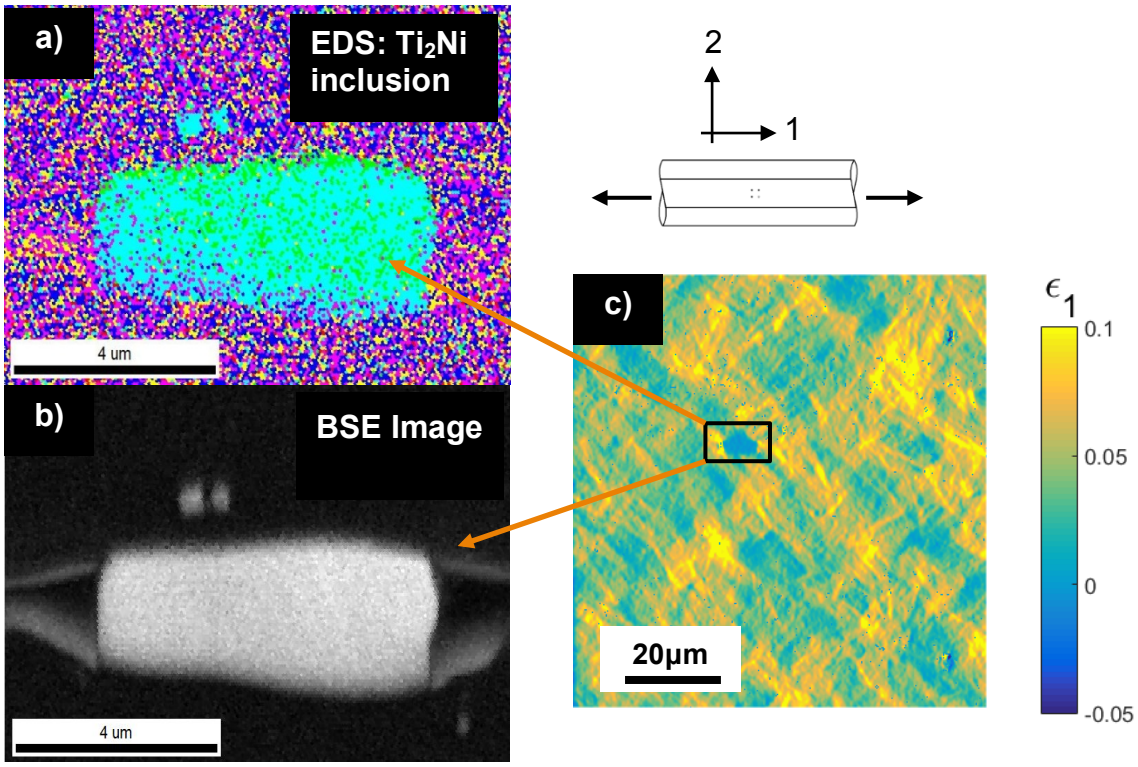

Figure 6.2: The strain behavior of an inclusion (Ti_2Ni) is drastically different from the matrix (NiTi). The inclusion area did not deform even though its matrix deformed to over 0.1 strain.

Section 6.2.3. Performance Prediction Using Magnitude of Detwinning Heterogeneity

There is potential to use metrics of the microscale strain distributions in the first few actuation cycles, particularly the rate of change of accumulation of residual strain, in order to rank lifetimes of microwires. Strain heterogeneity as an indicator of future device performance was investigated, as shown in Figure 6.3, where a larger actuation stroke size should correlate with shorter lifetimes. Specimens were tested up to five cycles, and the standard deviations of the microscale strain fields plotted versus the averaged strain over the field of view at that point. The results were inconclusive, and warrant further study. No statistically significant correlation was found between strain heterogeneity and stroke size with the limited number of test specimens examined. A comprehensive suite of testing is needed to examine this relationship, particularly at strains high enough to accumulate significant plastic deformation. There was, however, a clear correlation between grain size and strain heterogeneity, wherein the standard deviation of strain (indicative of detwinning) increased approximately 20% as the grain diameter was increased from 20-40nm to 10 micrometers. Future examination of the development of strain heterogeneity at larger grain sizes under increasing actuation strokes would be of interest. It would be interesting to examine the rate of change in detwinning across the first several actuation cycles as a function of stroke/lifetime – for example, does residual strain accumulate more rapidly in the first 50 cycles with a larger stroke? How does detwinning and the rate of residual strain accumulation depend on crystallographic texture? There are a number of possibilities to explore in this area that could lead to practical implementations for the predictive testing of actuator components.

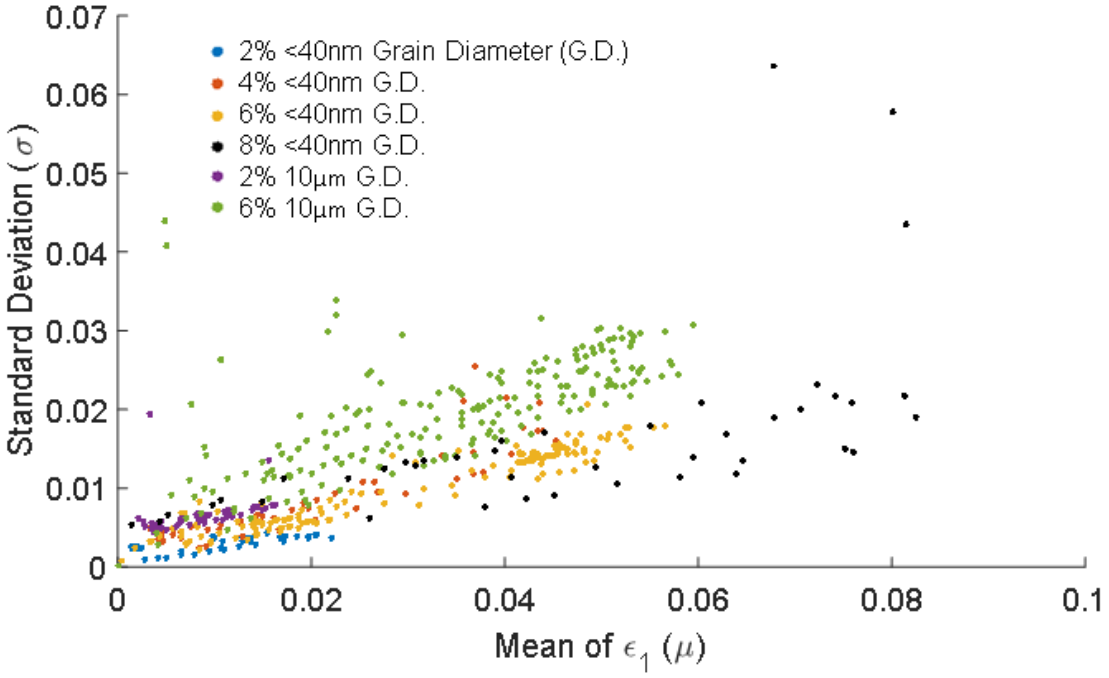

Figure 6.3: Preliminary testing on the effect of actuation stroke on the heterogeneity of the strain distribution. Each specimen was cycled for five cycles. The green (6%, 10 μm grain diameter) and yellow (6%, <40 nm grain diameter) data points represent three specimens tested. There was no clear correlation between strain heterogeneity during detwinning and actuation stroke, which may be due to the limited number of specimens tested especially under large strokes. There was a clear correlation between grain size and strain heterogeneity during detwinning.